

2020

High Spatial Resolution Silicon Detectors for Independent Quality Assurance in Motion Adaptive Radiotherapy and Charged Particle Radiotherapy Energy Verification

Matthew Keith Newall

Follow this and additional works at: <https://ro.uow.edu.au/theses1>

University of Wollongong

Copyright Warning

You may print or download ONE copy of this document for the purpose of your own research or study. The University does not authorise you to copy, communicate or otherwise make available electronically to any other person any copyright material contained on this site.

You are reminded of the following: This work is copyright. Apart from any use permitted under the Copyright Act 1968, no part of this work may be reproduced by any process, nor may any other exclusive right be exercised, without the permission of the author. Copyright owners are entitled to take legal action against persons who infringe their copyright. A reproduction of material that is protected by copyright may be a copyright infringement. A court may impose penalties and award damages in relation to offences and infringements relating to copyright material.

Higher penalties may apply, and higher damages may be awarded, for offences and infringements involving the conversion of material into digital or electronic form.

Unless otherwise indicated, the views expressed in this thesis are those of the author and do not necessarily represent the views of the University of Wollongong.

Recommended Citation

Newall, Matthew Keith, High Spatial Resolution Silicon Detectors for Independent Quality Assurance in Motion Adaptive Radiotherapy and Charged Particle Radiotherapy Energy Verification, Doctor of Philosophy thesis, School of Physics, University of Wollongong, 2020. <https://ro.uow.edu.au/theses1/1080>



UNIVERSITY
OF WOLLONGONG
AUSTRALIA

High Spatial Resolution Silicon Detectors for Independent Quality Assurance in Motion Adaptive Radiotherapy and Charged Particle Radiotherapy Energy Verification

Matthew Keith Newall

Supervisors:
Anatoly Rosenfeld
Marco Petasecca

This thesis is presented as part of the requirement for the conferral of the degree:

Doctor of Philosophy

This research has been conducted with the support of the Australian Government Research

Training Program Scholarship

University of Wollongong

School of Physics

August 2020

Abstract

Accurate empirical modelling of the treatment beam is necessary to ensure accurate delivery of dose to the intended target site. Dose calculations within the treatment planning system (TPS) for Stereotactic Radiosurgery (SRS) and Stereotactic Radiotherapy (SRT) treatment rely upon accurate beam data. Inaccuracies within the empirical measurements will propagate as errors throughout calculated patient dose distributions (Tyler, 2013). The necessary empirical measurements for beam commissioning include: percentage depth dose (PDD), output factor (OF) and beam profiles. Thus, especially for the consideration of the afore mentioned small radiation fields, it is important to ensure the most appropriate detector is chosen to conduct measurements of the treatment beams to achieve the highest possible accuracy in measurement of beam parameters.

Stereotactic Body Radiation Therapy (SBRT) requires precise delineation of the target using modern imaging modalities (MRI, CT etc.), accurate dosimetry to ensure the planned dose is delivered correctly and effective patient immobilisation. For extracranial sites the treatment accuracy is affected by tumour delineation which identifies the extent of the tumour volume and tumour motion resulting from the physical, biological and physiological processes of the human body. Delivery of radiation using highly conformal and small radiation beams presents challenges for dosimetry and quality assurance (Heydarian, 1996), (Das, 2008). To correctly measure dose in a small field an ideal dosimeter must exhibit properties including: small sensitive volume, near water equivalence, minimal beam perturbation and no dose-rate, energy or directional dependence (Pappas, 2008). Also, treatment planning for dose calculation must be conducted using algorithms which can account for the impact of the heterogeneities found in the abdomen and thoracic cavities to ensure calculation of the dose to tissue in regions with complex scattering conditions is accurate (Rubio, 2013).

In charged particle radiation therapy, the deposition of dose by charged particles within a small volume at the Bragg peak is uniquely sensitive to the particles penetration range, and it is directly dependent upon the incident beam energy and any small variations in material density and stopping power along the beam path (Mirandola, 2018). Significant tumour under/over dosage can be the result of incorrect estimation of in-patient beam penetration (Paganetti, 2012). The routine measurement and verification of percentage depth dose curves of Bragg peaks for charged particle

radiotherapy delivery systems is vital to ensure safe provision of radiotherapy treatment (Cantone, 2013). Unfortunately, devices providing a means of fast verification (for daily measurement) of beam energy stability in-phantom with high precision, accuracy and reliability are not readily available.

The Serial Dose Magnifying Glass (sDMG) is a multi-strip silicon detector designed by the Centre for Medical Radiation Physics (CMRP) and is comprised of two linear arrays of 128 diodes separated with pitch 0.2 mm. A monolithic silicon detector array, referred to and designated as DUO, designed by the CMRP is comprised of 505 silicon diodes arranged in two bisecting orthogonal linear arrays of 253 diodes, sharing a common central pixel, with pitch 0.2 mm.

This work examines the properties of the high spatial resolution linear silicon detector array, sDMG, for small field dosimetry and quality assurance (QA) of SRS, SBRT and Motion Adaptive Radiation Therapy (MART) using photons and the feasibility of the detector for fast, independent energy verification in charged particle beam radiation therapy. The 2D monolithic silicon detector array DUO was also investigated for dose verification in heterogeneous scattering conditions in MART and beam profiling in proton therapy.

Acknowledgments

I would first and foremost like to thank my supervisors, Distinguished Professor Anatoly Rosenfeld and Associate Professor Marco Petasecca. From the bottom of my heart I will never be able to thank both of you enough for your endless patience with me and tireless efforts to help and motivate me on this long but rewarding journey.

Anatoly, thank you so much for all your guidance and wisdom over the years. You've been a constant source of inspiration and support for me in both the times of great success and joy and the times of significant difficulty. I am so very grateful to have been your student and to learn from a foremost expert in medical radiation physics, particle therapy and solid state dosimetry. It is from your teaching and passion that ignited the spark within me to pursue and dedicate myself to a career in medical physics, and your faultless direction throughout this adventure that has driven me to be who I am today. I am forever thankful for the opportunities you offered and provided to me and the skills and knowledge you imparted to me throughout this journey.

Marco, I owe a tremendous thanks to you for everything you have done for me and all that you've taught me over the years. You instilled in me a deep passion for science and physics and a drive to pursue and achieve my goals. I am so very grateful and thankful to you for shaping my knowledge and skills. I have been inspired and guided by your actions and without you I could not have undertaken any of the amazing opportunities which were offered to me through working with you.

I would not be where I am today, with the knowledge and skills and wealth of experiences that I have, without the support and supervision of Marco and Anatoly, thank you to you both.

Claire, there aren't any words I can find that truly and completely capture how thankful and grateful I am for all your love and support. You have been my greatest cheerleader and motivator along the way and without you I couldn't have possibly completed this task.

To my parents and my brother, thank you all for your support, love and understanding over the many years. Without your care and guidance and encouragement I would not have been able to accomplish what I have today.

To all my friends and fellow postgraduate students at CMRP along the way, but especially to Saree Alnaghy, Anthony Espinoza, Mitchell Duncan, Lachlan Chartier and Trent Causer, I wish to deeply thank you for all your aid and encouragement over the years, I am truly grateful for everything you all have done for me. To all the staff and academics at CMRP, I wish to thank you all for your support.

To all my friends and colleagues at the Nelune Comprehensive Cancer Centre (NCCC) Prince of Wales Hospital (POWH) I want to thank every one of you so very much for all their enduring support.

Certification

I, Matthew Newall, declare that this thesis submitted in fulfilment of the requirements for the conferral of the degree Doctor of Philosophy, from the University of Wollongong, is wholly my own work unless otherwise referenced or acknowledged. This document has not been submitted for qualifications at any other academic institution.

Matthew Newall

August 2020

List of Abbreviations

1D	One-Dimensional
2D	Two-Dimensional
3D	Three-Dimensional
3DCRT	Three-Dimensional Conformal Radiation Therapy
AAPM	American Association of Physicists in Medicine
ACPSEM	Australasian College of Physical Scientists and Engineers in Medicine
ADC	Analogue-to-Digital Converter
AFE	Analogue Front End
ANT	Anterior
ART	Adaptive Radiation Therapy
ASIC	Application Specific Integration Circuit
BEV	Beams Eye View
BP	Bragg Peak
CAD	Computer Aided Design
CAX	Central Axis
CCE	Charge Collection Efficiency
CF	Correction Factor
cGy	Centigray
CMRP	Centre for Medical Radiation Physics
COP	Code of Practice
CPE	Charged Particle Equilibrium
CRT	Conformal Radiation Therapy
CSDA	Continuously Slowing Down Approximation
CT	Computed Tomography
DAQ	Data Acquisition
DMG	Dose Magnifying Glass
d_{\max}	Depth of dose maximum
DPP	Dose per Pulse

DVH	Dose-Volume Histogram
EBRT	External Beam Radiotherapy
EPID	Electronic Portal Imaging Device
EPOM	Effective Point of Measurement
FPGA	Field Programmable Gate Array
FF	Flattening Filter
FFF	Flattening Filter Free
FWHM	Full Width at Half Maximum
GUI	Graphical User Interface
GTV	Gross Tumour Volume
HIMAC	Heavy Ion Medical Accelerator in Chiba
IAEA	International Atomic Energy Agency
IC	Ionisation Chamber
IEEE	Institute of Electrical and Electronics Engineers
IMRT	Intensity Modulated Radiation Therapy
INF	Inferior
IPEM	Institute of Physics and Engineering in Medicine
IR	Infrared
ISO	Isocentre
LCPE	Lateral Charged Particle Equilibrium
LET	Linear Energy Transfer
LINAC	Linear Accelerator
LHS	Left Hand Side
M512	MagiPlate-512
MART	Motion Adaptive Radiation Therapy
MeV	Mega Electronvolt
MRI	Magnetic Resonance Imaging
MLC	Multi Leaf Collimator
MLIC	Multi-Layer Ionisation Chamber

MU	Monitor Unit
MV	Mega Volt
NIRS	National Institute of Radiological Sciences
NIST	National Institute of Standards and Technology
OAR	Organ-at-Risk
OD	Optical Density
OF	Output Factor
OSLD	Optically Stimulated Luminescent Dosimeter
PET	Positron Emission Tomography
PBP	Pristine Bragg Peak
PCB	Printed Circuit Board
PCHIP	Piecewise Cubic Hermite Interpolating Polynomial
PDD	Percentage Depth Dose
PGE	Prompt Gamma Emission
PMMA	Poly-(methyl methacrylate)
PMT	Photomultiplier Tube
POST	Posterior
PT	Proton Therapy
PTV	Planning Target Volume
PW	Penumbral Width
QA	Quality Assurance
RF	Radiofrequency
RGB	Red Green Blue
RHS	Right Hand Side
ROI	Region of Interest
RT	Radiotherapy
SAD	Source-to-Axis Distance
SBRT	Stereotactic Body Radiation Therapy
SD	Standard Deviation

sDMG	Serial Dose Magnifying Glass
SNR	Signal-to-Noise Ratio
SRS	Stereotactic Radiosurgery
SRT	Stereotactic Radiotherapy
SSD	Source to Surface Distance
SUP	Superior
TCPE	Transient Charged Particle Equilibrium
TIFF	Tagged Imaged File Format
TL	Thermoluminescence
TLD	Thermoluminescent Detector
TPS	Treatment Planning System
TRS	Technical Report Series
USB	Universal Serial Bus
UOW	University of Wollongong
VMAT	Volumetric Modulated Arc Therapy
WED	Water Equivalent Depth
WHO	World Health Organisation

Table of Contents

High Spatial Resolution Silicon Detectors for Independent Quality Assurance in Motion Adaptive Radiotherapy and Charged Particle Radiotherapy Energy Verification.....	i
Abstract	ii
Acknowledgments	iv
Certification	vi
List of Abbreviations	vii
Table of Contents	1
List of Figures	4
List of Tables.....	9
List of Publications.....	10
List of Conference Presentations	13
Chapter 1	14
Introduction.....	14
1.1 Overview	14
1.2 Objective of the study	15
1.3 Thesis structure.....	16
Chapter 2	18
Literature Review.....	18
2.1 Cancer and Radiation Therapy.....	18
2.2 External Beam Radiotherapy	20
2.2.1 3D Conformal Radiotherapy (3DCRT)	20
2.2.2 Intensity Modulated Radiotherapy	21
2.2.3 Stereotactic Body Radiotherapy & Stereotactic Radiosurgery	22
2.2.4 Motion Adaptive Radiation Therapy	23
2.3 Charged Particle Beam Radiotherapy	25
2.3.1 Proton Therapy	26
2.3.2 Carbon-ion Therapy	29
2.4 Quality Assurance in Radiation Therapy	30
2.4.1 Small Field Dosimetry.....	31
2.4.2 Current QA tools	35
2.4.3 Gamma Analysis	48
2.4.4 Charged Particle Range Verification.....	51
2.5 Devices designed by Centre for Medical Radiation Physics.....	53
2.5.1 Serial Dose Magnifying Glass (sDMG)	53
2.5.2 Monolithic silicon detector array (DUO)	55
2.5.3 Data Acquisition System	56
2.5.4 Graphical User Interface.....	57
Chapter 3	60
Device characterisation of Serial Dose Magnifying Glass (sDMG)	60
3.1 Introduction	60
3.2 Materials and Methods.....	60

3.2.1 Evaluation of the spatial resolution required by a pixelated detector	60
3.2.2 Radiation Hardness Characterisation.....	64
3.2.3 Dose Linearity	64
3.2.4 Dose per Pulse Dependence	64
3.2.5 Percentage Depth Dose Measurements	65
3.2.6 Beam Profile Measurements.....	65
3.2.7 Output Factor Measurements	66
3.3 Results	67
3.3.1 Evaluation of the spatial resolution required by a pixelated detector	67
3.3.2 Radiation Hardness Characterisation.....	69
3.3.3 Dose Linearity	70
3.3.4 Dose per Pulse Dependence	71
3.3.5 Percentage Depth Dose Measurements	72
3.3.6 Beam Profile Measurements.....	74
3.3.7 Output Factor Measurements	76
3.4 Discussion.....	77
3.5 Conclusion	79
Chapter 4	81
Quality Assurance of stereotactic radiotherapy combined with electromagnetic MLC tracking using silicon detectors.....	81
4.1 Introduction	81
4.2 Materials and Methods.....	82
4.2.1 DUO and sDMG.....	82
4.2.2 Phantom Scattering Conditions	82
4.2.3 Film Dosimetry.....	83
4.2.4 Dynamic treatment plan delivery	84
4.3 Results	87
4.3.1 DUO Dosimetric Validation.....	87
4.3.2 Dynamic treatment plan delivery with varying scattering conditions	88
4.4 Discussion.....	103
4.5 Conclusion	104
Chapter 5	105
Quality Assurance in Proton spot scanning radiation therapy.....	105
5.1 Introduction	105
5.2 Materials and Methods.....	106
5.2.1 Equalisation of detector	106
5.2.2 Lateral profiles	107
5.2.3 Edge-on acquisition	108
5.2.4 Energy Reconstruction	109
5.3 Results	112
5.3.1 Lateral Profiles	112
5.3.2 Edge-on acquisition	115
5.4 Discussion.....	118

5.5 Conclusion	120
Chapter 6	121
Energy Verification in heavy-ion radiation therapy	121
6.1 Introduction	121
6.2 Materials and Methods.....	122
6.2.1 Energy Reconstruction	123
6.3 Results	126
6.4 Discussion.....	130
6.5 Conclusion	131
Chapter 7	133
Conclusions.....	133
7.1 Summary.....	133
7.2 Impact & Future Directions	136
List of References	138
Appendices	147
Appendix A	147
Appendix B	166

List of Figures

Figure 2.1 (a) The Calypso panel and intrafraction motion monitoring system, the panel is extended and positioned over the patient during treatment (<i>Calypso / Varian</i> , 2020). (b) The 17G transponder beacon can be implanted in any soft tissue for localisation using Calypso (Bertholet, 2019).	25
Figure 2.2 PDD profile comparison between 21 MeV photons, 148 MeV protons and 270 MeV/U ¹² C ions (Schulz-Ertner, 2007). Figure reproduced with permission from ASCO Publications.	26
Figure 2.3 Diagram of the relative dose distributions from the surface of the skin for protons, carbon ions and X-rays. The SOBP of the proton and carbon-ion beams are generated by the summation of contributions from pristine Bragg peaks to cover the tumour target volume (Ishikawa, 2019). Figure reproduced with permission from Wiley.	27
Figure 2.4 Schematic illustration of the two primary methods of particle beam delivery, specific to proton therapy. (a) Passive scattering method – a broad particle beam is generated by scatterers, the SOBP is generated by a ridge filter, a binary range shifter alters the beam energy, and patient specific compensation bolus and collimator is used to conform the distal edge of the SOBP to the target in the patient. (b) Pencil beam scanning – a collimator defines the field size and scanning magnets are utilised to scan the pencil beam in three dimensions through the target (Ishikawa, 2019). Figure reproduced with permission from Wiley.	28
Figure 2.5 Schematic diagram illustrating the phenomenon of partial source occlusion (Palmans, 2018). Figure reproduced with permission from Wiley.	33
Figure 2.6 A Gaussian (solid black) curve approximates a small radiation field in one dimension, the dotted black curve demonstrates the measurement of a detector with a volume effect (5 mm wide), the deviation between the curves is displayed as a dot-dashed black line (Palmans, 2018). Figure reproduced with permission from Wiley.	34
Figure 2.7 An example of a thermoluminescent glow curve for LiF:Mg,Ti (TLD-100) material, which is readout following different pre-irradiation annealing processes. The peaks 1-5 identify the trapping centres (Kry, 2020). Figure reproduced with permission from Wiley.	40
Figure 2.8 Schematic drawing identifying the thickness and structure of EBT3 Gafchromic film (Devic, 2016). Figure reproduced with permission from Elsevier.	41
Figure 2.9 Schematic diagram of a silicon p-n junction as a radiation detector. The incident radiation generates excess electron (●) and hole pairs (○) which diffuse, over one diffusion length L_p , to the p-n junction and are subsequently swept across by the built-in potential and collected by the electrometer (Shi, 2003). Figure reproduced with permission from Wiley.	44
Figure 2.10 One-dimensional representation of dose-difference and distance to agreement evaluation between dose values which possess one spatial dimensions (Low, 1998). Figure reproduced with permission from Wiley.	49
Figure 2.11 Two dimensional representation of gamma analysis using the ellipsoid dose difference	

and distance to agreement evaluation method (Low, 1998). Figure reproduced with permission from Wiley.	50
Figure 2.12 The Zebra multi-layer ionization chamber device (<i>Zebra - Scan monolayer & SOBp measurements / IBA Dosimetry, 2020</i>).	52
Figure 2.13 The Serial Dose Magnifying Glass (sDMG). (a) Schematic diagram of silicon strip detector, DMG (Debrot, 2018). (b) sDMG mounted and wired bonded to a thin printed circuit board (PCB). Figure 2.13(a) reproduced with permission from Wiley.	54
Figure 2.14 sDMG enclosed within Solid Water phantom and connected to data acquisition system.	55
Figure 2.15 The DUO detector mounted and wire bonded to the thin PCB.	55
Figure 2.16 The sDMG detector connected to the AFE DAQ system with FPGA.	57
Figure 2.17 The AFE-Histogram graphical user interface (GUI) for acquisition, visualisation and analysis of sDMG measurements.	58
Figure 2.18 The AFE-DUO graphical user interface (GUI) for acquisition, visualisation and analysis of DUO measurements.	59
Figure 3.1. Dose profiles for various field sizes measured in a Solid Water block phantom using EBT3 film. (a) At depth 5 cm in Solid Water field sizes 0.5x0.5 cm ² to 10x10 cm ² . (b) At depth 10 cm in Solid Water field sizes 0.5x0.5 cm ² to 10x10 cm ²	62
Figure 3.2 One-sided Fourier amplitude spectra for the penumbral regions (3-97%) of various field sizes. (a) Fourier spectrums of profiles acquired at depth 5 cm in a Solid Water phantom. (b) Fourier spectrums of profiles acquired at depth 10 cm in a Solid Water phantom.	68
Figure 3.3 Experimental result for the measurement of the response of five pixels normalised to the pre-irradiation condition of the sDMG detector as a function of accumulated dose. Each pixel in the legend is denoted as a ‘Ch’, this is an abbreviation for channel, which relates to the chronological number of the individual pixel in the linear array.	70
Figure 3.4 The accumulated charge measured within the central channel of the sDMG detector as a function of applied photon radiation dose.	71
Figure 3.5 The dose per pulse response for the sDMG detector normalized to the estimated dose per pulse delivered at 1.5cm depth in water and 100cm SSD of 2.78×10^{-4} Gy/pulse.	72
Figure 3.6 PDD response measured with the sDMG detector and Markus ionisation chamber for a 6MV photon beam with 10 x 10 cm ² field size at 100cm SSD and percentage difference. (a) Uncorrected PDD response of sDMG detector. (b) PDD response of sDMG detector corrected for intrinsic dose per pulse dependence of sDMG detector.	73
Figure 3.7 sDMG and EBT3 film measured beam profiles for 6MV photon beam at 10cm deep and 90cm SSD for small radiation fields. (a) Field size 0.5 x 0.5 cm ² . (b) Field size 1 x 1 cm ² . (c) Field size 1.5 x 1.5 cm ² . (d) Field size 2 x 2 cm ² . (e) Field size 4 x 4 cm ² . (f) Field size 5 x 5 cm ²	75

Figure 3.8. Response of sDMG detector and EBT3 film to varying field size of a 6 MV photon beam normalised to response of detector to 10 x 10cm² field size. Percentage difference between sDMG and EBT3 film presented as a function of radiation field size. (a) Uncorrected OF response of sDMG detector. (b) OF response of sDMG detector corrected for intrinsic dose per pulse dependence... 77

Figure 4.1 Cross-sections illustrating the material composition of the three scattering conditions investigated and dimension of air gap. (a) Homogenous Solid Water phantom. (b) Homogenous timber phantom. (c) Heterogeneous timber phantom with Solid Water target. 83

Figure 4.2 (a) The sDMG detector positioned upon the HexaMotion platform above 6cm of Solid Water for backscatter and beneath 1.5cm of Solid Water. The Calypso motion tracking array is suspended above the detector, beneath the linac head, with the transponders suspended upon a foam insert above the detector to enable tracking. (b) The temporal pattern supplied to the HexaMotion phantom to mimic the motion of a lung in x and y direction during irradiation of the detector, x direction is into the image. 85

Figure 4.3 Comparison of EBT3 film and DUO beam profiles for 6 MV linac in homogenous timber phantom. (a) Superior-Inferior direction. (b) Left-Right direction. 88

Figure 4.4 6 MV Photon beam profiles measured with sDMG detector and EBT3 film at 1.5 cm deep and 100 cm SAD (isocentre) for characterisation of high resolution dynamic quality assurance capabilities with different field sizes. (a) No motion, 1 x 1 cm², along y-direction. (b) Motion, 1 x 1cm², along y-direction. (c) Motion and Tracking, 1 x 1 cm², along y-direction. (d) No motion, 1 x 1 cm², along x-direction. (e) Motion, 1 x 1 cm², along x-direction. (f) Motion and Tracking, 1 x 1cm², along x-direction. (g) No motion, 3 x 3 cm², along y-direction. (h) Motion, 3 x 3 cm², along y-direction. (i) Motion and Tracking, 3 x 3 cm², along y-direction. 90

Figure 4.5 3DCRT 6MV linac beam profiles for the three different scattering conditions and three different motion cases (No Motion, Motion and Motion+Tracking) using DUO and the corresponding point-to-point profile comparison. (a) Sup-Inf direction with homogenous Solid Water phantom. (b) Left-Right direction with homogenous Solid Water phantom. (c) Sup-Inf direction with homogenous timber phantom. (d) Left-Right direction with homogenous timber phantom. (e) Sup-Inf direction with heterogeneous timber and Solid Water target phantom. (f) Left-Right direction with heterogeneous timber and Solid Water target phantom. 94

Figure 4.6 IMRT 6MV linac beam profiles for the three different scattering conditions and three different motion cases (No Motion, Motion and Motion+Tracking) using DUO and the corresponding point-to-point profile comparison. (a) Sup-Inf direction with homogenous Solid Water phantom. (b) Left-Right direction with homogenous Solid Water phantom. (c) Sup-Inf direction with homogenous timber phantom. (d) Left-Right direction with homogenous timber phantom. (e) Sup-Inf direction with heterogeneous timber and Solid Water target phantom. (f) Left-Right direction with heterogeneous timber and Solid Water target phantom. 101

Figure 5.1 Schematic diagram (not to scale) of the experimental setup of DUO detector in proton pencil beam delivery for lateral profile measurements. Detector is positioned beneath increasing

depths of Solid Water material and aligned with the central axis of the pencil beam and the treatment isocentre, setup is repeated for sDMG and MatriXX.	108
Figure 5.2 Schematic diagram (not to scale) of the experimental setup of edge-on acquisition of proton pencil beam spot delivery for pristine Bragg peak energy reconstruction with sDMG. (a) Schematic of experimental setup, various depths of polystyrene are placed in front of the detector. (b) Delivery of proton pencil beam spot to sDMG detector, the treatment isocentre is identified by the green lasers, aligned to the front of the sDMG.	109
Figure 5.3 NIST calculated CSDA range for protons with energy from 1 to 235 MeV for silicon, polystyrene and water (Berger, 2017). (a) Visualised with Proton Energy as the ordinate and Projected Range the abscissa. (b) Visualised with Projected Range as the ordinate and Proton Energy the abscissa.	111
Figure 5.4 Lateral profiles of the proton pencil beam spot for varying depths in Solid Water compared between the sDMG and MatriXX. (a) 1.38 cm water equivalent depth. (b) 5.45 cm water equivalent depth. (c) 10.51 cm water equivalent depth. (d) 12.59 cm water equivalent depth.	112
Figure 5.5 Lateral profiles of the proton pencil beam spot for varying depths in Solid Water compared between DUO and MatriXX. (a) 1.38 cm water equivalent depth. (b) 5.45 cm water equivalent depth. (c) 10.51 cm water equivalent depth. (d) 12.59 cm water equivalent depth.	114
Figure 5.6 Schematic diagram (not to scale) of the experimental setup of the sDMG in edge-on acquisition with “Depth in Silicon” coordinate system described.	116
Figure 5.7 Results of the edge-on acquisition with sDMG in a proton pencil beam spot with varying thickness of polystyrene phantom material in front of the detector, with measured initial Bragg peak position highlighted in each callout box. (a) 60 mm polystyrene. (b) 70 mm polystyrene. (c) 80 mm polystyrene. (d) 90 mm polystyrene.	117
Figure 6.1 Setup of edge-on acquisition of sDMG detector in ^{12}C ion beam. (a) Schematic representation (not to scale) of the exposure of the linear detector array to the mono-energetic carbon ion beam for varying depths in PMMA phantom material. (b) Setup of experimental measurements at the carbon ion beam facility.	123
Figure 6.2 The calculated projected ranges from SRIM-2013 (Ziegler, 2013). (a) Determination of residual energy of ^{12}C ions at the entrance to silicon from Bragg peak measurement in depth of silicon. (b) Determination of the projected range of ^{12}C ions in PMMA without silicon present. (c) Determination of the energy of ^{12}C ions at the PMMA phantom surface from measurement of Bragg peak in PMMA without silicon present.	125
Figure 6.3 Combined measurements results of sDMG detector exposed to ^{12}C ion beam in edge-on acquisition mode with varying depths of PMMA phantom material preceding detector. (a) Results presented with abscissa describing the depth of the pristine Bragg peak delivered in depth in Silicon of linear sDMG array. (b) Results presented with abscissa describing the depth of PBP delivered in depth in PMMA phantom.	127

Figure 6.4 Individual measurements results of sDMG detector exposed to ^{12}C ion beam in edge-on acquisition mode with varying depths of PMMA phantom material preceding detector. (a) 54 mm PMMA. (b) 64 mm PMMA. (c) 89 mm PMMA. (d) 102 mm PMMA. 129

List of Tables

Table 2.1 Currently available commercial detector array systems, summarizing properties of both 2D and 3D dose acquisition systems (<i>OCTAVIUS 4D</i> - PTW Freiburg GmbH, 2020; <i>ArcCHECK®</i> - Sun Nuclear, 2020; <i>Products</i> , 2020; <i>MapCHECK® 3</i> - Sun Nuclear, 2020; <i>OCTAVIUS Detector 1600 SRS</i> - PTW Freiburg GmbH, 2020; <i>SRS MapCHECK®</i> - Sun Nuclear, 2020).	46
Table 3.1 Penumbral width (PW) and Full-Width at Half-Maximum (FWHM) measurements for EBT3 film dose profiles.	67
Table 3.2 90% bandwidth measurements and corresponding Nyquist resolutions for various field sizes.	69
Table 3.3 sDMG and EBT3 film measurement FWHM and penumbral width (20%-80%) comparison for different small field sizes.	75
Table 4.1 Comparison of Full-width at Half Maximum (FWHM) and Penumbral Width (PW) measurements for EBT3 Film and DUO in Superior-Inferior (Sup-Inf) and Left-Right directions.	88
Table 4.2 sDMG and EBT3 film measurement FWHM and penumbral width (20%-80%) comparison for cases without motion, with motion and with motion and tracking enabled.....	90
Table 4.3 Percentage agreement from global gamma analysis for 2%/2mm criterion for Superior-Inferior and Left-Right directions between ‘no motion’ (NM) and ‘motion’ (M) or ‘motion+tracking’ (MT) for 3DCRT plan delivery with DUO.	96
Table 4.4 Mean absorbed dose in PTV for Superior-Inferior axial profiles of 3DCRT delivery. ..	97
Table 4.5 Mean absorbed dose in PTV for Left-Right axial profiles of 3DCRT delivery.....	97
Table 4.6 Mean absorbed dose in PTV for Superior-Inferior axial profiles of IMRT delivery.	102
Table 4.7 Mean absorbed dose in PTV for Left-Right axial profiles of IMRT delivery.	102
Table 5.1 sDMG and MatriXX measurements of FWHM and penumbral width for left hand side (LHS) only (20%-80%) for PBP pencil beam spot at different depths.....	113
Table 5.2 DUO and MatriXX measurement FWHM and penumbral width (20%-80%) comparison for PBP pencil beam spot for different depths.....	114
Table 5.3 Results of the measured Bragg peak in silicon using the sDMG in edge on acquisition	118
Table 6.1 Results of the measurement of the pristine Bragg peak location in the sDMG detector for various depths of PMMA phantom material and the calculation of the incident ^{12}C ion beam energy at the PMMA phantom surface (E_0).	130

List of Publications

The following is a complete list of peer-reviewed publications during my candidature.

- Aldosari, A. H., Petasecca, M., Espinoza, A., **Newall, M.**, Fuduli, I., Porumb, C., Alshaikh, S., Alrowaili, Z. A., Weaver, M., Metcalfe, P., Carolan, M., Lerch, M. L. F., Perevertaylo, V. and Rosenfeld, A. B. (2014) ‘A two dimensional silicon detectors array for quality assurance in stereotactic radiotherapy: MagicPlate-512’, *Medical Physics*, 41(9). doi: 10.1118/1.4892384.
- Alnaghy, S. J., Gargett, M., Liney, G., Petasecca, M., Begg, J., Espinoza, A., **Newall, M.** K., Duncan, M., Holloway, L., Lerch, M. L. F., Lazea, M., Rosenfeld, A. B. and Metcalfe, P. (2016) ‘Initial experiments with gel-water: towards MRI-linac dosimetry and imaging’, *Australasian Physical and Engineering Sciences in Medicine*, 39(4), pp. 921–932. doi: 10.1007/s13246-016-0495-1.
- Debrot, E., **Newall, M.**, Guatelli, S., Petasecca, M., Matsufuji, N. and Rosenfeld, A. B. (2018) ‘A silicon strip detector array for energy verification and quality assurance in heavy ion therapy’, *Medical Physics*, 45(2), pp. 953–962. doi: 10.1002/mp.12736.
- Duncan, M., **Newall, M. K.**, Caillet, V., Booth, J. T., Keall, P. J., Lerch, M., Perevertaylo, V., Rosenfeld, A. B. and Petasecca, M. (2018) ‘Real-time high spatial resolution dose verification in stereotactic motion adaptive arc radiotherapy’, *Journal of Applied Clinical Medical Physics*, 19(4), pp. 173–184. doi: 10.1002/acm2.12364.
- Fuduli, I., **Newall, M. K.**, Espinoza, A. A., Porumb, C. S., Carolan, M., Lerch, M. L. F., Metcalfe, P., Rosenfeld, A. B. and Petasecca, M. (2014) ‘Multichannel Data Acquisition System comparison for Quality Assurance in external beam radiation therapy’, in *Radiation Measurements*, pp. 338–341. doi: 10.1016/j.radmeas.2014.05.016.
- Merchant, A. H., **Newall, M.**, Guatelli, S., Petasecca, M., Lerch, M., Perevertaylo, V., Milluzzo, G., Petringa, G., Romano, F., Cirrone, G. A. P., Cuttone, G., Jackson, M. and Rosenfeld, A. B. (2017) ‘Feasibility study of a novel multi-strip silicon detector for use in proton therapy range verification quality assurance’, *Radiation Measurements*, 106, pp. 378–384. doi: 10.1016/j.radmeas.2017.03.017.
- Metcalfe, P., Alnaghy, S. J., **Newall, M.**, Gargett, M., Duncan, M., Liney, G., Begg, J.,

- Oborn, B., Petasecca, M., Lerch, M. and Rosenfeld, A. (2017) ‘Introducing dynamic dosimaging: Potential applications for MRI-linac’, in *Journal of Physics: Conference Series*. doi: 10.1088/1742-6596/777/1/012007.
- **Newall, M. K.**, Petasecca, M., Duncan, M., Fuduli, I., Shukaili, K. Al, Booth, J. T., Keall, P., Corde, S., Pereveratylo, V., Lerch, M. and Rosenfeld, A. B. (2017) ‘Innovative detectors for quality assurance dosimetry in SBRT of stationary and movable targets’, in *Journal of Physics: Conference Series*. doi: 10.1088/1742-6596/777/1/012014.
 - Petasecca, M., Alhujaili, S., Aldosari, A. H., Fuduli, I., **Newall, M.**, Porumb, C. S., Carolan, M., Nitschke, K., Lerch, M. L. F., Kalliopuska, J., Perevertaylo, V. and Rosenfeld, A. B. (2015) ‘Angular independent silicon detector for dosimetry in external beam radiotherapy’, *Medical Physics*, 42(8), pp. 4708–4718. doi: 10.1118/1.4926778.
 - Petasecca, M., **Newall, M. K.**, Booth, J. T., Duncan, M., Aldosari, A. H., Fuduli, I., Espinoza, A. A., Porumb, C. S., Guatelli, S., Metcalfe, P., Colvill, E., Cammarano, D., Carolan, M., Oborn, B., Lerch, M. L. F., Perevertaylo, V., Keall, P. J. and Rosenfeld, A. B. (2015) ‘MagicPlate-512: A 2D silicon detector array for quality assurance of stereotactic motion adaptive radiotherapy’, *Medical Physics*, 42(6), pp. 2992–3004. doi: 10.1118/1.4921126.
 - Porumb, C. S., Aldosari, A. H., Fuduli, I., Cutajar, D., **Newall, M.**, Metcalfe, P., Carolan, M., Lerch, M. L. F., Perevertaylo, V. L., Rosenfeld, A. B. and Petasecca, M. (2016) ‘Characterisation of Silicon Diode Arrays for Dosimetry in External Beam Radiation Therapy’, *IEEE Transactions on Nuclear Science*, 63(3), pp. 1808–1817. doi: 10.1109/TNS.2016.2567446.
 - Shukaili, K. A., Petasecca, M., **Newall, M.**, Espinoza, A., Perevertaylo, V. L., Corde, S., Lerch, M. and Rosenfeld, A. B. (2017) ‘A 2D silicon detector array for quality assurance in small field dosimetry: DUO’, *Medical Physics*, 44(2). doi: 10.1002/mp.12060.
 - Stansook, N., Petasecca, M., Utitsarn, K., **Newall, M.**, Metcalfe, P., Carolan, M., Lerch, M. and Rosenfeld, A. B. (2017) ‘The angular dependence of a two dimensional monolithic detector array for dosimetry in small radiation fields’, in *Journal of Physics: Conference Series*. doi: 10.1088/1742-6596/777/1/012020.
 - Stansook, N., Utitsarn, K., Petasecca, M., **Newall, M. K.**, Duncan, M., Nitschke, K.,

Carolan, M., Metcalfe, P., Lerch, M. L. F., Perevertaylo, V. L., Tomé, W. A. and Rosenfeld, A. B. (2017) 'Technical Note: Angular dependence of a 2D monolithic silicon diode array for small field dosimetry: Angular', *Medical Physics*, 44(8). doi: 10.1002/mp.12377.

List of Conference Presentations

The following is a list of oral presentations related to this work during my candidature:

- **Newall, M. K.**, Petasecca, M., Porumb, C. S., Fudili, I., Carolan, M., Kron, T., Hardcastle, N., Lerch, M. L. F. and Rosenfeld, A. B. (2013) 'Characterisation of a High spatial resolution multi-strip detector (Serial Dose Magnifying Glass) for dose profiling', Presenting author at Engineering and the Physical Sciences in Medicine (EPSM) conference 2013
- **Newall, M. K.**, Petasecca, M., Aldosari, A. H., Lerch, M. L. F., Carolan, M., Booth, J. T., Colvill, E., Keall, P. J., Jackson, M., Barton, M., Kron, T., Tomé, W. A., Metcalfe, P. and Rosenfeld, A. B. (2014) 'The serial dose magnifying glass: A unique tool for the study of moving targets in radiotherapy', Presenting author Combined Scientific Meeting (CSM) 2014
- **Newall, M.**, Petasecca, M., Bolst, D., Cassel, C., Guatelli, S., Lerch, M. L. F., Matsufuji, N. and Rosenfeld, A. B., (2014) 'Characterisation of a silicon strip fetector for QA in heavy ion therapy', Presenting author at Institute of Electrical and Electronics Engineers (IEEE) Nuclear Science Symposium (NSS) & Medical Imaging Conference (MIC) 2014
- **Newall, M.**, Petasecca, M., Duncan, M., Alosari, A. H., Al Shukaili, K., Porumb, C. S., Fuduli, I., Booth, J. T., Colvill, E., Keall, P., Lerch, M. L. F., Perevertaylo, V. and Rosenfeld, A. B. (2015) 'High spatial and timing resolution silicon based dosimeter for quality assurance of real time adaptive radiotherapy', Presenting author at 3rd European Society for Radiotherapy and Oncology (ESTRO) Forum 2015
- **Newall, M.**, Duncan, M., Caillet, V., Booth, J. T., Keall, P. J., Petasecca, M. and Rosenfeld, A. B. (2016) 'Dose verification in real time motion adaptive radiotherapy in heterogeneous medium', Presenting author at Engineering and the Physical Sciences in Medicine (EPSM) conference 2016

Chapter 1

Introduction

1.1 Overview

Radiation therapy is a cancer treatment modality which is both safe and effective for many different types of cancers. Treatment by radiotherapy comprises the precise application of radiation to abnormal cancerous cells and involves the use of different forms of radiation, such as; high energy X-rays, gamma rays, electrons, protons or carbon-ions, to damage and/or kill cancerous cells while preserving healthy cells and thus prevent the cancer cells from growing abnormally within the human body (*What is Radiation Therapy? - Targeting Cancer*, 2020).

Stereotactic Radiosurgery (SRS) and Stereotactic Body Radiation Therapy (SBRT) require precise delineation of the target using modern imaging modalities (MRI, CT etc.), accurate dosimetry to ensure the planned dose is delivered correctly and effective patient immobilisation. For extracranial sites, in SBRT, the treatment accuracy is affected by tumour delineation which identifies the extent of the tumour volume and tumour motion resulting from the physical, biological and physiological processes of the human body.

Delivery of radiation using highly conformal and small radiation beams, of photons or charged particles, presents challenges for dosimetry and quality assurance (Heydarian, 1996), (Das, 2008). To correctly measure dose in a small field, an ideal dosimeter must exhibit properties including:

small sensitive volume, near water equivalence, minimal beam perturbation and no dose-rate, energy or directional dependence (Pappas, 2008).

In charged particle radiation therapy the deposition of dose by charged particles within a small volume at the Bragg peak is uniquely sensitive to the particles penetration range, and it is directly dependent upon the incident beam energy and any small variations in material density and stopping power along the beam path (Mirandola, 2018). Significant tumour under/over dosage can be the result of incorrect estimation of in-patient beam penetration (Paganetti, 2012). The routine measurement and verification of percentage depth dose (PDD) curves of Bragg peaks for charged particle radiotherapy delivery systems is vital to ensure safe provision of radiotherapy treatment (Cantone, 2013). Unfortunately, devices providing a means of fast verification (for daily measurement) of beam energy stability in-phantom with high precision, accuracy and reliability are not readily available.

This work investigates the utilisation and accuracy of silicon detector arrays, designed and developed at the Centre for Medical and Radiation Physics (CMRP) at the University of Wollongong (UOW), for independent dose verification of small photon radiation beams in motion adaptive radiation therapy and fast independent energy verification in charged particle radiation therapy.

1.2 Objective of the study

The objective of this work is to examine the properties of the high spatial resolution linear silicon detector array, Serial Dose Magnifying Glass (sDMG), for small field dosimetry and quality assurance (QA) of Stereotactic radiosurgery (SRS), Stereotactic Body Radiation Therapy (SBRT) and Motion Adaptive Radiation Therapy (MART) using photons and the feasibility of the detector for fast, independent energy verification in charged particle beam radiation therapy. The 2D monolithic silicon detector array DUO was also investigated for dose verification in heterogeneous scattering conditions in MART and beam profiling in proton therapy.

1.3 Thesis structure

This thesis is composed of 7 chapters investigating the use of two silicon detectors as QA devices across photon and charged particle beam radiation therapy. This chapter, Chapter 1, provides; a short introduction, an overview of the thesis objective and the essential structure of the work.

Chapter 2 provides a literature review and background to introduce the forms of advanced external beam radiotherapy treatment delivery modalities available today, such as; IMRT, SBRT, SRS, proton therapy and carbon-ion therapy. The chapter describes the necessity and importance of quality assurance processes, discusses and highlights the complexities of small field dosimetry relative to available quality assurance devices and summarises the specifications of the commercially available systems.

Chapter 3 characterises the dosimetric properties of the Serial Dose Magnifying Glass (sDMG) under photon irradiation, investigating and presenting the results of measurements of radiation hardness, dose linearity, dose per pulse dependence, percentage depth dose measurement, beam profiling and output factor relative to the gold standard clinical dosimeters, ionisation chambers and radiochromic film. This chapter also proposes an investigation into the optimum resolution required to reconstruct beam profiles in stereotactic radiation therapy (SRT) modalities based on an analysis of high resolution radiochromic film data, conducted to generate recommendations for the pixel separation required to accurately measure beam penumbræ and profiles.

Chapter 4 is centred on the complexities of QA and dose verification of treatments of small volume tumours within the lungs which require small conformal radiation beams and real time motion adaptation to improve treatment efficiency and reduce normal tissue toxicity. Motion adaption is achieved through Multi Leaf Collimator (MLC) tracking, which has been applied clinically to lung Stereotactic Ablative Body Radiotherapy (SABR) treatments (Booth et al., 2016). The combination of small field dosimetry, target motion and heterogeneous scattering conditions is challenging for accurate dose measurement in real-time and thus measurements utilising sDMG and DUO in phantoms with various scattering conditions and motion strategies are discussed. The measurements undertaken in Chapter 4 investigate the effects of homogenous and heterogeneous scattering

conditions upon the delivered dose distribution in the treatment of dynamic targets using small photon radiation fields and aims to evaluate the performance of the sDMG and DUO detectors compared to the gold standard of high spatial resolution two-dimensional dosimetry, EBT3 film.

Chapter 5 aims to introduce the use of the sDMG and DUO detectors for lateral beam profile measurements in a clinical proton radiation beam with energy 129.46 MeV at the Francis H. Burr Proton Therapy Center (FHBPTC) at Massachusetts General Hospital (MGH). The measured results from sDMG and DUO for exposure to a proton pencil beam spot, used in proton pencil beam scanning, will be compared to a commercially available ionisation chamber array, MatriXX, used routinely in the clinic. The experimental results of an investigation will be presented into the efficacy and accuracy of the sDMG as a fast, independent proton energy verification system.

Chapter 6 introduces the use of the sDMG as a fast, independent energy verification system for use in charged particle therapy with a heavy-ion carbon beam.

Chapter 7 concludes the work undertaken to investigate the properties of the high spatial resolution silicon detector arrays, sDMG and DUO, for small field dosimetry and QA of SRS, SBRT and MART using photons and the feasibility of the sDMG for fast, independent energy verification in charged particle beam radiation therapy.

Chapter 2

Literature Review

This chapter aims to introduce some of the forms of advanced external beam radiotherapy treatment delivery modalities available today, such as; IMRT, SBRT, SRS, proton therapy and carbon-ion therapy. The necessity and importance of quality assurance processes is highlighted and the complexities of small field dosimetry are described. Finally, the operation and utility of essential dose measurement devices are described and the tools and devices commercially available are summarized.

2.1 Cancer and Radiation Therapy

Cancer refers to a disease of the cells of the human body in which abnormal cells grow in an uncontrolled way into a mass, known as a tumour. These abnormal cells eventually damage or invade surrounding healthy tissues and may spread to other parts of the body and cause further harm through uncontrolled growth of additional tumours (*What is cancer? | Cancer Australia, 2020*). This invasive action of abnormal cells spreading throughout the body and forming secondary tumours is referred to as a process known as metastasizing.

The World Health Organisation (WHO) describes cancer as the second leading cause of death worldwide, being responsible for approximately 9.6 million deaths in 2018 (*Cancer, 2018*). The three leading modalities for the treatment of cancer are surgery, chemotherapy and radiation therapy (radiotherapy) (*Types of Cancer Treatment - National Cancer Institute, 2020*).

In 2018, the most common causes of cancer related death worldwide were (*Cancer*, 2018):

- Lung – 1,760,000 deaths
- Colorectal – 862,000 deaths
- Stomach – 783,000 deaths
- Liver – 782,000 deaths
- Breast – 627,000 deaths

Radiation therapy is a cancer treatment modality which is both safe and effective for many different types of cancers. Treatment by radiotherapy comprises the precise application of radiation to abnormal cancerous cells and involves the use of different forms of radiation, such as; high energy X-rays, gamma rays, electrons, protons or carbon-ions, to damage and/or kill cancerous cells while preserving healthy cells and thus prevent the cancer cells from growing abnormally within the human body (*What is Radiation Therapy? - Targeting Cancer*, 2020). The applied radiation physically damages the DNA in the abnormal cancerous cells which biologically interrupts the cancer cells ability to multiply, this leads to shrinking and eventually destruction of the tumour. Unlike the cancer cells, normal healthy cells within the human body can recover from the effects of the radiation more easily (*What Is Radiotherapy? Benefits & Side Effects - TROG Cancer Research*, 2020).

The potential benefits of radiotherapy to the patient, in contrast to chemotherapy and surgery, include (*What Is Radiotherapy? Benefits & Side Effects - TROG Cancer Research*, 2020):

- Patients find that radiotherapy treatments have minimal impact upon their daily schedules,
- Radiotherapy treatments are generally conducted without requiring prolonged hospitalisation,
- Individual treatment sessions often require less than one hour to be completed, sometimes less than thirty minutes.

Radiation therapy may be prescribed as a definitive treatment modality in some cases, but it is most often prescribed in combination with other treatment modalities, such as; chemotherapy and surgery,

to achieve the greatest curative benefit to the patient.

2.2 External Beam Radiotherapy

External Beam Radiotherapy (EBRT) describes the most common method of providing and delivering radiotherapy and primarily includes the utilization of a linear accelerator, often referred to as a linac. The linac generates high energy photon or electron beams of radiation, outside of the patient, which are precisely directed at a target within the patient (Mayles, 2007).

2.2.1 3D Conformal Radiotherapy (3DCRT)

The essential form of modern external beam radiotherapy delivered to patients is referred to as 3D Conformal Radiotherapy (3DCRT). The goal of conformal radiotherapy is to achieve the delivery of a high-dose, which conforms to the targeted volume, whilst ensuring the organs-at-risk (OARs) receive a low-dose, so as not to cause any complications (Mayles, 2007). 3DCRT involves the utilisation of three primary technological advances (Elith, 2011):

- Advanced imaging modalities, such as; computed tomography (CT), magnetic resonance imaging (MRI) and positron emission tomography (PET), to visualise and provide a 3D anatomical model of the target and OARs for accurate identification,
- Improvements in computational technology enabling the treatment planning system (TPS) to incorporate these images and produce dose calculations visualised on the images,
- Development of the MLC allowing precise shaping of the radiation beam to the shape of the target volume in the beams-eye view (BEV).

The combination of these advances enabled three-dimensional images to guide the treatment planning process. This form of EBRT is widely used in the treatment of tumours in; the central nervous system, head and neck, thorax, pancreas, prostate and rectum (Purdy, 2008). The most significant disadvantage of 3DCRT is the limited ability to generate conformal doses to concave targets, this results in higher organs-at-risk doses as the target wraps around critical structures.

2.2.2 Intensity Modulated Radiotherapy

Intensity Modulated Radiotherapy (IMRT) is a form of external beam radiotherapy delivery which utilises radiation beams with non-uniform radiation fluence (Webb, 2003). IMRT enables the delivery of comparatively improved dose distributions relative to 3DCRT due to the capability to sculpt and conform the dose distribution around targets which are composed of complex shapes (Elith, 2011).

The features of IMRT which were not associated with 3DCRT include (Galvin, 2007):

- Inverse treatment planning methodology, the treatment plan is generated algorithmically based on supplied dose and target constraints
- Large numbers of treatment fields and/or subfields which produce a radiation field with a modulated intensity

Modulation of the radiation field intensity is possible using custom designed beam compensators, however the patient specific design and production process would be impractical for modulating large numbers of treatment fields across multiple patients. The MLC is key in modulating the beam fluence and thus making the delivery of IMRT possible, IMRT is delivered with fixed gantry angles with either static MLC dose segments, often referred to as step-and-shoot IMRT (or static MLC), or with dynamic MLC dose segments, often referred to as sliding window IMRT (or dynamic MLC or DMLC). In sliding window IMRT, the MLC leaf pairs move across the radiation field throughout beam delivery to deliver a fluence modulated dose which is conformed to the target shape (Mayles, 2007). The capability to modulate the radiation fluence within the beam allows for significant improvements in the sparing of surrounding critical structures due to the rapid dose falloff (Lee, 2008).

IMRT offers significant advantages in generating conformal dose to complex targets in close proximity to critical structures (OARs), but there are some disadvantages. A significantly larger number of monitor units (MU) are required to deliver a comparable prescription dose to 3DCRT due to the increased utilisation of multiple subfields with small MLC apertures (Purdy, 2008). Additionally, due to the increased number of radiation beams and beam directions used when

delivering IMRT, there is an increase in the volume of normal healthy tissue which is exposed to a lower radiation dose, when compared to conventional radiotherapy (Hall, 2003), resulting from the increased exposure to head scatter and leakage radiation from the linac.

2.2.3 Stereotactic Body Radiotherapy & Stereotactic Radiosurgery

Stereotactic Radiotherapy (SRT) and Stereotactic Radiosurgery (SRS) are a class of radiotherapy treatment characterised by the use of highly conformal photon beams to deliver high doses with minimal geometric error within a hypofractionated regimen (Charlie Ma, 2019).

The application of this treatment methodology to tumour sites within the body, known as Stereotactic Body Radiation Therapy (SBRT), requires accurate target delineation of the tumour volume relative to the surrounding healthy tissue and minimisation of the safety margins resulting from the biological and physiological motions of the tumour (Kavanagh, 2006). These goals are realised through the implementation of accurate pre-treatment imaging protocols, image guidance and motion management strategies. SBRT is generally utilised for the treatment of tumours with diameters less than 5 cm (Hanna, 2015). Within the thoracic and abdominal region, possible treatment sites may include: lung, liver and kidneys (Kavanagh, 2006),(Rubio, 2013).

Essentially, SBRT is classified as the treatment of tumours with 1-5 dose fractions which occur outside of the brain (extracranial). SRS is generally classified as the treatment of intracranial tumours with a single or few fractions. Dose fractions of 5 Gy or more for extracranial treatment sites are generally considered stereotactic with fractions of 10 Gy or more for intracranial tumours (Brown, 2014).

SBRT requires precise delineation of the target using modern imaging modalities (MRI, CT etc.), accurate dosimetry to ensure the planned dose is delivered correctly and effective patient immobilisation. For extracranial sites the treatment accuracy is affected by tumour delineation which identifies the extent of the tumour volume and tumour motion resulting from the physical, biological and physiological processes of the human body. Delivery of radiation using highly conformal and small radiation beams presents challenges for dosimetry and quality assurance (Heydariyan, 1996), (Das, 2008). To correctly measure dose in a small field an ideal dosimeter must

exhibit properties including: small sensitive volume, near water or tissue equivalence, minimal beam perturbation and no dose-rate, energy or directional dependence (Pappas, 2008). Also, treatment planning for dose calculation must be conducted using algorithms which can account for the impact of the heterogeneities found in the abdomen and thoracic cavities to ensure calculation of the dose to tissue in regions with complex scattering conditions is accurate (Rubio, 2013).

There are a several hypothesised radiobiological effects which describe the greater antitumour efficacy exhibited by doses per fraction of 10 Gy and above, these include (Brown, 2014):

- Damage to endothelial cells may enhance the cytotoxic effect of irradiation of tumour cells
- Vascular damage which is induced by high doses of radiation lead to indirect tumour cell death
- Irradiation of a tumour at one site, with high doses, induces an antitumour immunological rejection of any metastatic lesions present at a distant site

SBRT can be delivered using any modern linac, provided the appropriate access to image guidance and immobilisation devices. Radiosurgery can currently be delivered via a number of contemporary systems which include; the Gamma Knife Perfexion (Elekta AB, Stockholm, Sweden), Cyberknife (Accuray, Sunnyvale, USA), TrueBeam STx (Varian, Palo Alto, USA) (Sheehan, 2014) and Versa HD (Elekta AB, Stockholm, Sweden).

2.2.4 Motion Adaptive Radiation Therapy

Modern cancer therapy utilising external beam radiation therapy (EBRT) is becoming increasingly complex having progressively introduced radiation beam shaping, intensity modulation and moving forward to clinical implementation of radiation therapy treatments which adapt to the changing internal anatomy attributable to patient breathing, motion and positioning.

Real-time adaptive radiation therapy (ART) is an emerging class of highly advanced external beam radiotherapy which aims to improve the conformal delivery of radiation dose and minimise the need for large treatment margins which are accounting for motion. These effects are achieved by re-optimising the treatment based upon the patient-specific changes in anatomy which occur during

treatment. Within the abdomen and thorax of the patient, periodic changes in anatomy are predominantly attributed to the motion resulting from patient breathing; such intrafraction organ motions, can adversely impact treatment accuracy (Shirato, 2004).

Motion management strategies seek to mitigate the effects of target motion, such strategies include: gating (Kubo, 1996), breath-hold techniques, compression and tumour tracking (Bertholet, 2019). Tumour tracking methodologies re-position the treatment beam and/or patient robotically (Depuydt, 2011; Lang, 2014) to compensate for tumour motion. In all forms of tracking, the position of the tumour site must be localised in real-time. Numerous technologies offer real-time localisation capabilities, including; optical imaging of external markers or surrogates (Heinzerling, 2020), implanted internal markers (active or passive), fluoroscopic imaging and on-board imaging (such as kV or MV imaging) (Ng, 2012), MRI (Green, 2018), (Henke, 2018), (Keall, 2020).

Multi-Leaf Collimator (MLC) tracking (Booth, 2016), (Keall, 2014) is a motion adaptive strategy that applies real-time tumour localisation to modify and re-position the MLC shape during treatment. Tumour localisation can be provided using implanted radiofrequency emitters, named beacons (Shah, 2011), within the patient. The beacons are positioned within close-proximity to the target and deliver surrogate motion data to localize the position of the target during irradiation.

The Calypso (Varian, Palo Alto, CA) system, Figure 2.1, is the most commonly used means of providing non-ionising continuous real-time 3D localization of implanted transponders. For clinical use of localisation and monitoring of an internal target, three transponders are implanted in or near to the target. Each transponder is an electromagnetic resonance circuit with a different resonance frequency (300-500 kHz), sealed in a glass capsule for tissue compatibility and protection. A panel positioned above the patient contains an array of excitation coils and a second array of receiver coils. Each transponder is excited in series and the signal localised by triangulation to provide a 3D spatial coordinate of the centroid of the transponder with a frequency of 10-25 Hz relative to the position of the panel. The position of the transponders is then determined relative to the linac isocentre based on the calibration of three in-room cameras detecting infrared (IR) markers on the panel (Bertholet, 2019). The panel is present in the path of the treatment beam throughout delivery with the influence of the Calypso panel on dose difference was found to be clinically insignificant (Zou, 2013).



(a)



(b)

Figure 2.1 (a) The Calypso panel and intrafraction motion monitoring system, the panel is extended and positioned over the patient during treatment (*Calypso / Varian, 2020*). (b) The 17G transponder beacon can be implanted in any soft tissue for localisation using Calypso (Bertholet, 2019).

2.3 Charged Particle Beam Radiotherapy

Charged particle beam radiotherapy, also referred to as ion or hadron therapy, utilises beams of charged particles, such as protons or heavier ions, like carbon, instead of photons, to deliver dose to the target (Mayles, 2007).

Particle beams exhibit an increase in energy deposition, and physical absorbed dose, with increasing penetration depth, reaching a sharp maximum value of energy deposition which occurs at the end of the particles range in the material through which it traverses. For a mono-energetic beam of

particles this is referred to as the pristine Bragg peak (Schulz-Ertner, 2007). This behaviour of particles is in direct contrast to the initial maximum intensity deposited by photons upon reaching charged particle equilibrium in the medium followed by decay in intensity due to attenuation. A percentage depth dose (PDD) comparison between photons, protons and carbon ions is shown in Figure 2.2.

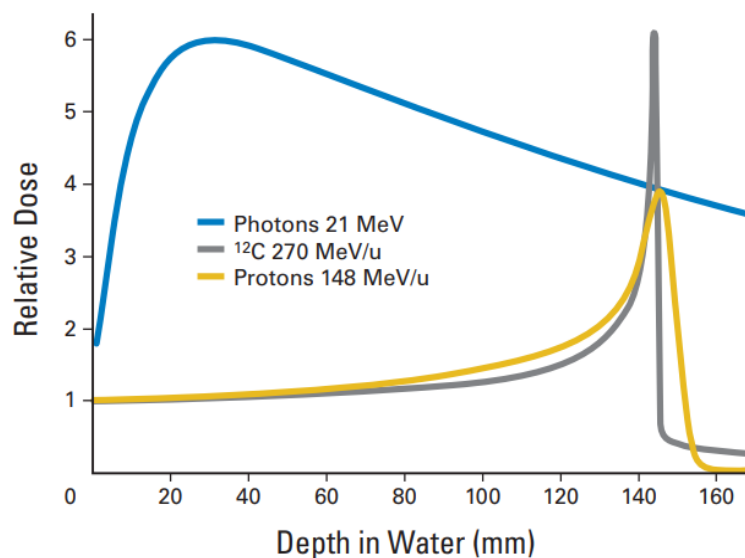


Figure 2.2 PDD profile comparison between 21 MeV photons, 148 MeV protons and 270 MeV/U ¹²C ions (Schulz-Ertner, 2007). Figure reproduced with permission from ASCO Publications.

The range of the particle in the medium is directly determined by the energy of the incident particles. Particle beams also demonstrate steep dose fall-off at the field edges, this effect combined with the Bragg peak means that particle beams can localise dose to the target with greater precision than photons (Trikalinos, 2009).

2.3.1 Proton Therapy

The pristine Bragg peak of a mono-energetic proton beam is too narrow and sharp to be used directly to treat tumours of the various shapes and sizes necessary for cancer treatment. Thus, it is necessary to broaden the peak of the beam to conform to the shape of the tumour, the spread-out Bragg peak (SOBP). This is generally achieved using one of two methods, either; passive scattering or pencil beam scanning, Figure 2.4.

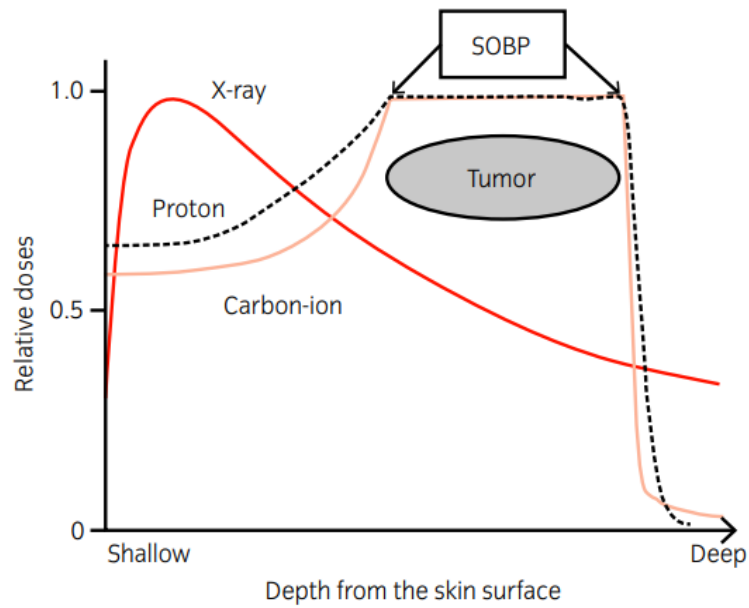


Figure 2.3 Diagram of the relative dose distributions from the surface of the skin for protons, carbon ions and X-rays. The SOBP of the proton and carbon-ion beams are generated by the summation of contributions from pristine Bragg peaks to cover the tumour target volume (Ishikawa, 2019). Figure reproduced with permission from Wiley.

Passive scattering utilises a ridge filter to generate a spread-out Bragg peak which corresponds to the necessary size to cover the targeted volume. Pencil beam scanning dynamically alters the path of the particle beam using powerful scanning magnets, allowing generation of the SOBP by the deposition of dose as individual spots within the target volume. This is often termed dose painting and in proton therapy can be most commonly achieved by one of two methods; slice-by slice where dose is delivered from the most distal to proximal layer of the target sequentially (Saini, 2016) or volumetrically where repeated scans through the target volume are delivered in depth (Zenklusen, 2010). The clearest advantages of pencil beam scanning relative to passive scattering result from the capability to optimise dose delivery, in terms of absorbed dose conformity, at both the distal and proximal extents of a target. Additionally, availability of inverse planning methods allows for deposition of multiple dose levels within a single field (Saini, 2016).

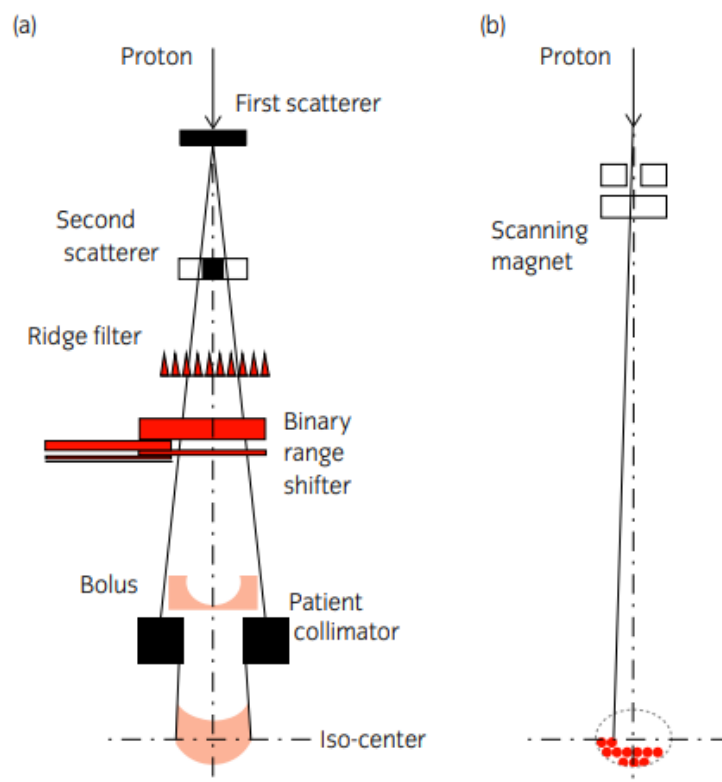


Figure 2.4 Schematic illustration of the two primary methods of particle beam delivery, specific to proton therapy. (a) Passive scattering method – a broad particle beam is generated by scatterers, the SOBP is generated by a ridge filter, a binary range shifter alters the beam energy, and patient specific compensation bolus and collimator is used to conform the distal edge of the SOBP to the target in the patient. (b) Pencil beam scanning – a collimator defines the field size and scanning magnets are utilised to scan the pencil beam in three dimensions through the target (Ishikawa, 2019). Figure reproduced with permission from Wiley.

Proton beams deposit very little physical dose within the medium beyond the depth of the Bragg peak, shown in Figure 2.2. Thus, the physical radiation dose delivered to normal tissues at the entrance of the radiation field and beyond the targeted area is less for protons when compared to photons (Trikalinos, 2009).

In terms of the biological advantages of protons in comparison to photons, protons exhibit a higher linear energy transfer (LET) than photons, however, the radiobiological properties of protons are not that substantially different to photons (Morimoto, 2014). LET is the rate at which a particle beam loses energy when penetrating into tissue. Photons, electrons and protons are considered to be sparsely ionizing radiations and often referred to as low-LET radiations (Tsuji, 2012).

2.3.2 Carbon-ion Therapy

Important differences exist between carbon ions and protons. The foremost physical difference between carbon ions and protons is that the peak-to-plateau ratio in the PDD profile (Figure 2.2) is greater in carbon ion beams than it is in proton beams (Shioyama, 2015). Additionally, the beam penumbra is smaller in carbon ion beams compared to protons beams as a result of the reduced influence of Coulomb scattering for particles with a larger mass. Carbon ion beams also exhibit an energy spread and range straggling that is smaller than proton beams thus carbon ion beams possess an improved lateral dose fall-off at the field edges. Carbon ion beams demonstrate a higher physical dose at the distal end beyond the Bragg peak compared to protons, this is caused by the primary carbon ions undergoing nuclear interactions and fragmenting into lower atomic number particles, referred to as a fragmentation tail (Tsujii, 2012).

In contrast to the biological comparison of protons and photons, heavy ions, such as carbon, exhibit the similarly favourable physical properties of protons, in addition to superior biological advantage over protons, in comparison to photons (Morimoto, 2014). Carbon-ions are densely ionising particles and are thus considered to be a high-LET radiation type. The LET of a particle is an important parameter to consider to evaluate biological effect as the relative biological effectiveness (RBE) of a radiation type increases with increasing LET. The RBE is defined as the delivered dose of radiation under investigation which is required to produce the same biological effect as a delivered dose of reference radiation (assumed to be a Co-60 source) (Mayles, 2007). In terms of different common radiotherapy particle types; the RBE of photons is assumed to be 1.0, for protons an RBE of 1.1 is generally clinically used and for carbon-ions the RBE is assumed by most institutions to be 3.0 (Lühr, 2018). These assumptions introduce uncertainties in establishing the radiobiological dose to targets and thus more sophisticated methods of modelling RBE are in constant active development. Carbon ions exhibit an advantageous radiobiological property whereby the LET of carbon ions increases with increasing depth, reaching a maximum in the Bragg peak where the targeted tumour will be located (Tsujii, 2012).

The tumour sites generally targeted for treatment using carbon ions include; non-small cell lung cancer, malignant tumours in the head, neck and spine, ocular melanoma, prostate cancer, uterine cancer and bone and soft tissue sarcomas (Trikalinos, 2009).

2.4 Quality Assurance in Radiation Therapy

The processes of quality assurance (QA) in radiation therapy involve the ongoing evaluation of functional performance characteristics of the treatment machine (Low, 2011). Assessment and routine validation of the stability and consistency of such performance characteristics is vital for ensuring safe patient treatment as the functional performance of a radiotherapy machine directly influences the geometrical and dosimetric accuracy of the delivered treatment. Evaluation of functional performance characteristics are conducted with high accuracy and precision during the commissioning of a radiotherapy treatment delivery system. From these initial measurements routine QA check methods utilizing the most appropriate tool or detector are established to ensure functional performance characteristics are accurately and efficiently monitored for fluctuation or fault. The development of new QA tools and devices which offer measurements with high spatial resolution without requiring laborious clinical time on the machine are important for improving treatment delivery outcomes throughout radiotherapy.

It is important and necessary to establish a distinction between routine quality assurance checks of machine performance characteristics and patient specific quality assurance to measure the magnitude and distribution of dose intended to be delivered to a patient.

For complex external beam radiotherapy treatment modalities (i.e. VMAT or IMRT; step and shoot or sliding window) it is important to conduct patient specific quality assurance (QA) involving physical measurements (i.e. in-phantom). This practice encompasses the investigation and evaluation of the dose distribution delivered by the treatment machine compared to the predicted dose distribution calculated by the treatment planning system (TPS) (Miften, 2018).

The most appropriate dosimeter and phantom for measurement-based patient specific verification practices is dependent upon a number of factors:

- Detector-related performance characteristics, such as; effective point of measurement, tissue-equivalency, energy dependence, resolution, volume averaging, sensitivity, active area, angular dependence, dose-rate dependence, output information

- Delivery technique-related characteristics, such as; beam energy, flattening filter free, dose-rate, field sizes, dose distribution gradients, gantry rotation

Dose verification can be conducted as spatial analysis in one-dimension (a single point or line), two-dimensions (a plane) or three-dimensions (a volume). The method of assessment of delivered dose must be carefully chosen considering the strengths, weaknesses, available equipment, intended treatment technique and time (Miften, 2018):

- 1D measurements - provide accurate absolute dose measurement at a single point or along a line-profile in a phantom
- 2D measurement methods - must be calibrated (to yield absolute dose) and provide more comprehensive information for plan analysis, but only in a single predetermined plane of interest within the phantom
- 3D methods - can be either; true 3D measurements or calculated from 2D projections based on reconstruction algorithms. They must also be calibrated and offer three-dimensional assessment of the delivered dose throughout a representative volume, but are increasingly complex and to provide accurate QA results (i.e. tolerance and action limits) must be carefully commissioned assessing the error detection capability

2.4.1 Small Field Dosimetry

The physics of small radiation fields is an important area of investigation due to the increasing utilization of SBRT and SRS worldwide in the treatment of cancer. Accurate and precise measurement of absorbed dose in small radiation fields is vital to ensure radiation therapy is safely provided to patients who will be able to directly benefit from the improvements in local control and overall survival demonstrated by SBRT and SRS in the treatment of some cancers.

The characteristics of the ideal dosimeter for use in small field dosimetry, and consequently SBRT, may be summarised to include the properties: near water equivalence, minimal beam perturbation and high spatial resolution due to small sensitive volume and minimal extra cameral material, as

well as dose-rate, energy and directional independence (Pappas, 2008). Several detectors and dosimetry systems possess a number of these properties.

The treatment of small volume cancers often requires small area radiation beams to minimise effects on healthy tissue. Measuring the physical effects of small radiation fields requires specialised detectors. The challenges of small photon field dosimetry include: steep dose gradients, partial occlusion of the beam source and lateral electron disequilibrium, as well as considerations related to beam perturbation effects, detector size and detector packaging composition (Heydarian, 1996; Das, 2008; Bouchard, 2015, 2015). The implications of the three main physical small field conditions will be summarized.

2.4.1.1 Lateral Charged Particle Equilibrium

A loss of lateral charged particle equilibrium (LCPE, often referred to as lateral electron disequilibrium) is found to occur if the maximum range of secondary electrons is larger than the half width (or radius) of the photon beam (Aspradakis, 2010). A parameter is determined which describes the minimum radius of a circular photon field for which at the centre of the field, the absorbed dose to water and the collision kerma in water are equal, equation (2.1) (Palmans, 2017).

$$r_{LCPE} = 8.369 \times TPR_{20,10}(10) - 4.382 \quad (2.1)$$

The r_{LCPE} establishes the relationship between the minimum detector size, for which the conditions of LCPE exist, and the photon beam field size. This parameter is dependent upon the ratio of the measured tissue-phantom ratio (TPR) at 20cm depth in water to 10cm depth in water, this is a common energy specifier in MV radiotherapy (Andreo, 2006). In a region in which the LCPE condition does not exist; absorbed dose is not equal to the collision kerma in water and thus a detector (or cavity) is unable to accurately measure absorbed dose.

2.4.1.2 Partial Source Occlusion

The focal spot of the X-ray beam is not a point but can be represented by the full-width at half maximum (FWHM) of the bremsstrahlung photon fluence distribution that is exiting the X-ray

target, which can be termed the direct beam source. This distribution is typically represented by a Gaussian distribution and is the result of blurring of the finite-size electron pencil beam striking the X-ray target caused by bremsstrahlung production and electron scattering (Aspradakis, 2010).

From the point of measurement, less of the direct beam source is visible as the collimator setting is decreased, Figure 2.5. Thus, the indirect and extra-focal scatter becomes less important to the measurement of dose at the point of measurement. That is, for small collimator settings, such as those for small radiation beams, the direct beam source is obstructed (or shielded) from the view of the point of measurement. Thus, the number of primary photons reaching the isocentre, and the point of measurement, is reduced, this phenomenon is referred to as partial source occlusion (Aspradakis, 2010).

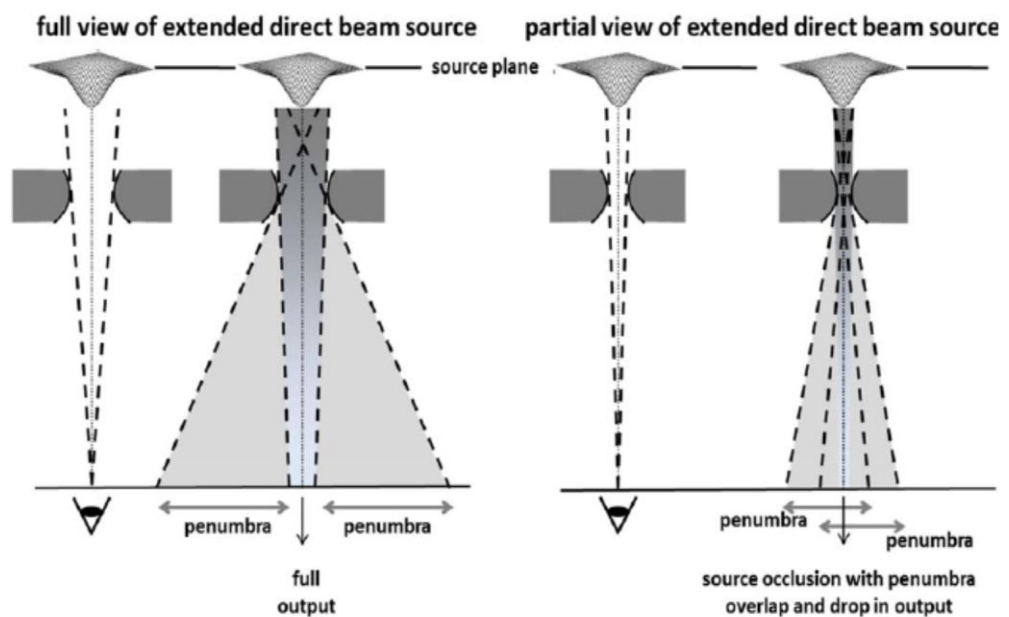


Figure 2.5 Schematic diagram illustrating the phenomenon of partial source occlusion (Palmans, 2018). Figure reproduced with permission from Wiley.

2.4.1.3 Volume Averaging

The size of the detector relative to the size of the radiation field is an important feature of the physics of small field dosimetry. The signal produced within a detector (measuring absorbed dose), in response to a radiation field, is proportional to the mean absorbed dose over its sensitive volume. This signal is also influenced by the homogeneity of the absorbed dose over the volume of detection

and this effect results in volume averaging. Figure 2.6 is an illustrative depiction of the consequences, in one-dimensional (1D) space, of volume averaging upon a physical measurement of a small radiation beam, which exhibits Gaussian curvature, by a detector which is 5 mm wide. The dimensions of the ideal and circular detector, relative to the ideal and circular radiation beam, are depicted in Figure 2.6 as two black dots, upon the plot. This is a theoretical depiction of the consequences of attempting to measure the Gaussian curve (black solid line) of a small radiation beam with a detector with volume averaging over a dimension of 5 millimetres (black dotted line) (Wuerfel, 2013). The result measured by the detector (black dotted line) is shown to not perfectly record the intensity of the small radiation beam, exhibiting underestimation of the radiation peak and overestimation of the beam penumbra. Additionally, the presence of the detector within the radiation field results in a perturbation of the charged particle fluence, this perturbation effect is entangled with volume averaging (Palmans, 2018).

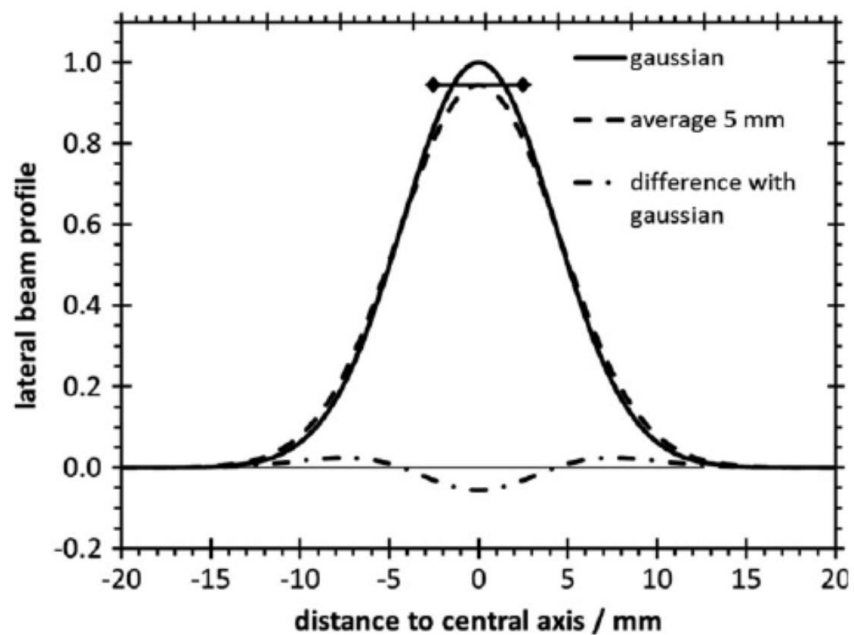


Figure 2.6 A Gaussian (solid black) curve approximates a small radiation field in one dimension, the dotted black curve demonstrates the measurement of a detector with a volume effect (5 mm wide), the deviation between the curves is displayed as a dot-dashed black line (Palmans, 2018). Figure reproduced with permission from Wiley.

2.4.2 Current QA tools

2.4.2.1 Ionisation Chamber

The ionisation chamber is the simplest form of a gas-filled detector and consists of a receptacle filled with gas and two opposing electrodes. A voltage is applied between the electrodes and as the gas is (theoretically) a perfect insulator, no electric current flows between the two electrodes. Incident radiation traversing the gas will interact with and ionise the gas, the electric field present between the electrodes causes the diffusion of the ions produced by the radiation in the gas towards the electrodes. This produces a current which can be measured using an electrometer (Mayles, 2007).

Cavity ionisation chambers encompass two basic geometries of ionisation chamber: cylindrical (or thimble) chambers and parallel-plate (or plane-parallel) chambers. Both of these geometries of ionisation chamber are designed to perform as Bragg-Gray cavities in megavoltage photon qualities.

The Bragg-Gray cavity theory establishes a link between the absorbed dose in a medium and the absorbed dose measured in a detectors sensitive volume (often referred to as a cavity). If the cavity is small and doesn't perturb the fluence of charged particles in the medium and if the absorbed dose in the cavity is solely deposited by particles crossing it then the cavity is said to obey the Bragg-Gray conditions. Under the conditions of Bragg-Gray cavity theory the dose in the medium, D_{med} can be related to the absorbed dose in the cavity, D_{cav} through the ratio of the average unrestricted mass stopping powers of the medium and the cavity.

$$D_{med} = D_{cav} \left(\frac{\bar{S}}{\rho} \right)_{med,cav} \quad (2.2)$$

For the chamber to behave as a good approximation of a perfect Bragg-Gray cavity it should possess the following features (Mayles, 2007):

- The air cavity should be small such that the sensitive volume is well-defined.

- The central electrode and wall should be constructed from materials which are as homogenous and water-equivalent as possible.
- The chamber walls should be as thin as possible.

The Spencer-Attix cavity theory is an extension of the Bragg-Gray cavity theory which accounts for the production of secondary electrons resulting from the hard collisions of primary electrons that are slowing down while traversing the cavity. These secondary electrons may possess enough kinetic energy, above a cut-off value (often denoted Δ), to either escape the sensitive volume or produce further ionisations, thus they must be considered a part of the electron spectrum traversing the cavity. To account for this phenomenon modification is required to the stopping power calculated within the cavity to include this additional particle fluence (Mayles, 2007). Thus, the absorbed dose in the medium can be related to the absorbed dose in the cavity through the mean restricted mass collision stopping power ratio of the medium to the cavity.

In the case of small field dosimetry and small sensitive volumes it is necessary to utilise Monte Carlo simulation to accurately model and determine the electron fluences. The accurate determination of the particle fluence allows the use of the Spencer-Attix cavity theory for the determination of the necessary stopping powers for calculation of dose within the medium (Bouchard, 2015).

Deviations of the design and construction of ionisation chambers away from being perfect Bragg-Gray and Spencer-Attix cavities necessitates the use of perturbation correction factors to ensure accurate measurement of absolute dose to the medium. These correction factors include (Andreo, 2006):

- Chamber cavity - The presence of an air-filled ionisation chamber introduces a low-density heterogeneity into the medium.
- Chamber wall - The electron fluence within the air cavity of an ionisation chamber consists partly of electrons generated in the uniform medium surrounding the chamber which traverse the wall, and partly of secondary electrons generated by interactions within the chamber wall.

- Central electrode material - The cylindrical ionisation chamber has a central electrode which is generally composed of either aluminium or graphite.
- Replacement of medium by chamber - A certain volume of the medium is displaced by the presence of the detector when a measurement with an ionisation chamber is performed.

Furthermore, the charge collected within an ionisation chamber can be different from the charge produced by the complete interactions of radiation within the chamber gas. This difference arises from the practicalities of electrical design and the physics of ion transport. The phenomena which affect the charge collected include; air density correction at time of measurements, ion recombination, polarity effects and stem (and leakage) effects. The mechanism of influence for each phenomena must be understood and the appropriate means of correction or mitigation (or minimisation of effect) applied.

2.4.2.2 Diamond Detector

Diamond detectors operate as a form of solid-state ionisation chamber (Laub, 2014). Ionising radiation incident upon the diamond crystal produces electron-hole pairs which move freely through the crystal lattice altering the electrical conductivity of the diamond. With the application of an external bias voltage the current generated by ionising radiation is proportional to the incident radiations dose-rate.

As diamond is composed almost entirely of carbon (except for some necessary impurities), diamond detectors exhibit near tissue equivalent properties as the ratio of the mass attenuation coefficients of water to carbon are nearly constant for all photon energies (*X-ray Mass Attenuation Coefficients / NIST*, 2020). Diamond detectors are well suited for dosimetry in stereotactic radiosurgery and high dose gradient regions due to their high resistance to radiation damage (Plansky, 1980), negligible directional dependence (Veselsky, 2018), high sensitivity (Vatnitsky, 1993), stability in prolonged response (Hoban, 1994), small physical size (high spatial resolution) and near energy independence. Synthetic single crystal diamond detectors with sensitive volumes of about 0.0038 mm³ have been fabricated for relative dosimetry in small photon and electron beams. The investigated small volume synthetic diamond dosimeter demonstrated good linearity, dose rate independence, energy independence and minimal angular and temperature dependences (Ciancaglioni, 2012).

To achieve accurate and reproducible dose measurements with diamond detectors it is necessary to stabilize their dose response with pre-irradiation prior to use (Veselsky, 2018). The irradiation prior to use reduces the impact of the polarization effect where the electric field generated by the external bias is reduced by electrons captured in ionized traps. Diamond detector exhibit very small temperature dependence (Veselsky, 2018) which is easily corrected and dose-rate dependence which must be appropriately corrected to yield accurate results (Hoban, 1994).

2.4.2.3 Thermoluminescent Detectors (TLD)

The thermoluminescent dosimeter (TLD) is an ionising radiation detector which operates using the principle of thermoluminescence (TL) (Kron, 1994, 1995). TLDs are composed of specific types of crystal which upon exposure to ionising radiation absorb and store the delivered energy within their crystal lattice structure, when heated the crystals re-emit that energy as light (Mayles, 2007). TL materials are generally produced by doping phosphors with activators as with lithium fluoride doped with magnesium and titanium (LiF:Mg-Ti) and lithium borate doped with copper (Li₂B₄O₇:Cu) (Sadeghi, 2015). Detection and measurement of the light output (generally using a photomultiplier tube, PMT) upon heating can be used to identify the magnitude of dose previously delivered to the crystal (Kry, 2020).

The processes of TL within a crystal can be explained using band theory. When the crystal is irradiated, holes and free electrons are produced within the lattice. The free electrons may travel within the conduction band for a short time until they are either (Mayles, 2007):

- Trapped at defects within the crystal lattice, recombining with holes either radiatively (e.g. fluorescence) or non-radiatively within the valence band or,
- Captured at activated luminescence centres, and thus deactivating the centre by emission of light.

When the crystal is heated after irradiation the electrons which were trapped within the defects in the lattice are provided with sufficient thermal energy to escape into the conduction band. Once in the conduction band the free electrons will again travel freely until they are either:

- Trapped at defects,
- Recombine with holes within the valence band (either radiatively or non-radiatively) or,
- Captured and recombine at the luminescence centres which are activated by holes (thermoluminescence).

The final of the three processes mentioned above is responsible for the capability to accurately measure the magnitude of dose to which the crystal was exposed by measurement of the luminescence. The light output from the crystal is measured during the readout heating cycle using a photomultiplier tube (PMT), converting the luminescence or light output into a current. Different temperatures are required to readout the intensity of light emitted from different trapping centres which possess different depths within the crystals bandgap structure. The temperature of the TLD is increased while monitoring the light output forming a glow curve graph of signal vs temperature. The thermoluminescence signal over a region of interest or the maximum intensity of a thermoluminescence peak defines the measured signal from the crystal (Kry, 2020). Following the heating and readout cycles the crystal will either return to its natural state or may require additional heating, known as annealing, to restore it to its natural state.

The appropriate and accurate clinical utilisation of TLD's in radiotherapy requires consideration of the detectors clinical advantages and disadvantages. TLD's exhibit near tissue equivalence as a result of the chosen crystal composition. Appropriate clinically acceptable TLD materials must be chosen to appropriately minimise the dosimetric performance related to energy dependence for the radiation quality being measured. The limitations in use of TLD's in a radiotherapy clinic are related directly to the functional physical size, temperature dependence, thermal and optical fading, dose dependence (supralinearity) and accuracy and the significant read-out and handling requirements.

Optically stimulated luminescent dosimeters (OSLD) function similarly to TLD's except are read-out using optical stimulation rather than heat. The properties of these dosimeters are similar to TLD's with similar disadvantages related to handling and read-out and physical size.

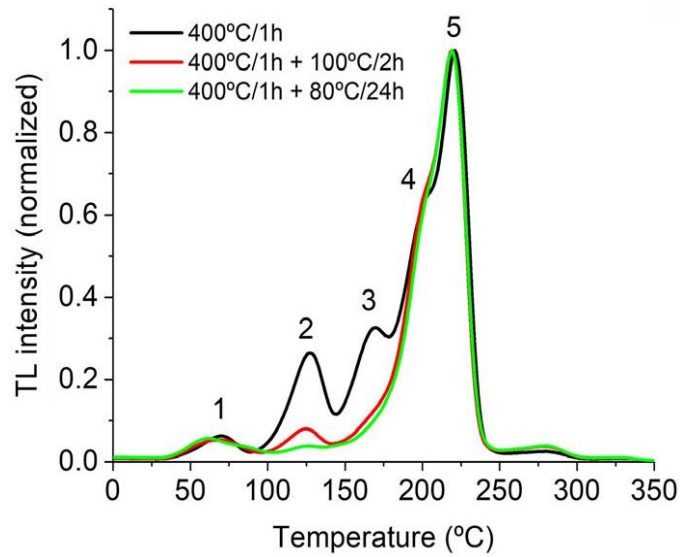


Figure 2.7 An example of a thermoluminescent glow curve for LiF:Mg,Ti (TLD-100) material, which is readout following different pre-irradiation annealing processes. The peaks 1-5 identify the trapping centres (Kry, 2020). Figure reproduced with permission from Wiley.

2.4.2.4 Radiochromic (EBT3) Film

Radiochromic (often referred to as Gafchromic) film is a transparent and colourless film medium which responds to ionising radiation and ultraviolet light by turning deep blue, exhibiting two nominal absorption bands at 636 nm and 582 nm (León-Marroquín, 2016). The colour change induced by the ionising radiation traversing the film material is proportional to radiation dose and formed by a process of solid-state polymerisation within the sensitive layer. The radiation-induced molecular process produces conjugated double bonds between the ends of neighbouring polymer chains, combining to form longer structures which absorb light. This polymerisation process is responsible for the characteristic darkening of the film and occurs over time without the need for additional thermal, optical or chemical processing (Mayles, 2007).

The polymer chains produced within the sensitive layer upon exposure to ionising radiation absorb light. The transmission of light through the film and thus the image present within the film can be read out by a standard flat-bed transmission scanner (or other densitometer). The attenuation of light traversing the film medium is described by the Beer-Lambert law relating the properties of the film to the absorption of light. The blue image generated within film is stable up to temperatures of 60°C, above these temperatures the image changes from blue to red.

Radiochromic (radiotherapy) films are manufactured and sold in a number of standard configurations designed for different purposes i.e. EBT3, EBT-XD, RTQA2, MD-V3, HD-V2. In general these film configurations are intended for different dose ranges and are composed of different active and base layer thicknesses (*Radiotherapy Films - GAFchromic™*, 2020). EBT3 film is the standard radiochromic film for patient dosimetry and IMRT verification and is designed for the dose range 0.2-10 Gy. The structure of EBT3 film is symmetrical, consisting of a single active layer (~28 μm of active component, marker dye and stabilisers) between two clear polyester base substrate laminates (~125 μm) (Niroomand-Rad, 1998). The active component of radiochromic EBT3 film is lithium-10, 12-pentacosadiyonate (LiPCDA) in crystalline form (Lewis, 2016). The surface of the polyester substrates is treated to contain microscopic silica spheres which prevent the formation of Newton's Rings interference patterns when scanning using a flatbed scanner (Marroquin, 2016). Other configurations (e.g. asymmetrical layer geometries) of radiochromic film are available, optimised for different intended purposes.

The photon mass energy absorption coefficient (μ_{en}/ρ) and electron mass collision stopping power for radiochromic film are very similar to those for skeletal muscle and water. This can be attributed to the near tissue equivalent composition of radiochromic films (9.0% hydrogen, 60.6% carbon, 11.2% nitrogen, 19.2% oxygen) (Avevor, 2017). Thus, radiochromic films (EBT3) may be considered near tissue equivalent in response, exhibiting minimal energy dependence over the therapeutic (MV & kV) photon energy ranges (Ataei, 2019).

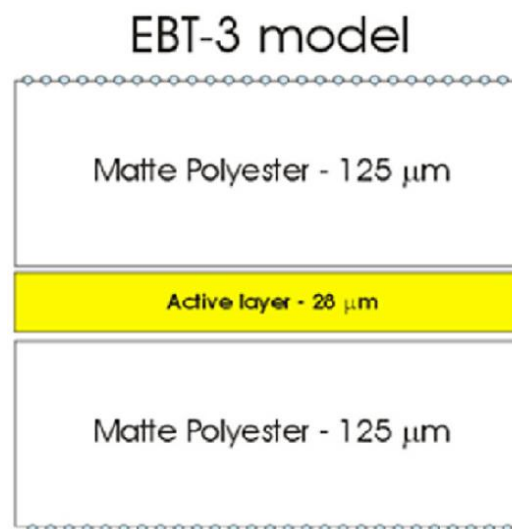


Figure 2.8 Schematic drawing identifying the thickness and structure of EBT3 Gafchromic film

(Devic, 2016). Figure reproduced with permission from Elsevier.

After irradiation the degree to which the radiochromic film darkens in response to the delivered dose to the sensitive layer can be quantified by measuring how much light is attenuated as it passes through the film. The darkening is measured in terms of net optical density (OD) which is defined as the \log_{10} of the ratio of the intensity of light transmitted through the film prior to irradiation (I_0) to the intensity of light transmitted through the film after exposure to radiation (I) (Butson, 2003). This quantity is proportional to dose (within certain limiting conditions):

$$\text{Net Optical Density, } OD = \log_{10} \frac{I_0}{I} \quad (2.3)$$

For the purposes of radiotherapy dosimetry, film is generally scanned in 48-bit RGB (Red Green Blue) colour mode at a nominal spatial resolution with the results saved in .TIFF file format. The intensity across the film is digitised over a grid determined by the selected spatial resolution and quantified in terms of a 16-bit pixel value describing the magnitude of red, green and blue colour at each pixel location.

To derive dose from the intensity quantified as a 16-bit pixel value (in one of the three colour channels), a calibration curve is necessary to relate the net optical density to dose. Ideally the relationship between these two quantities should be linear, however in reality it is not and is only linear over a short range, and may differ based on film batch number. Thus, the characteristic or dose calibration curve should be established for each film batch by exposing a set number of film pieces to known dose quantities, measuring the resultant film darkening after a standardised period of time. Fitting the data of the calibration curve (dose as a function of net optical density) with a polynomial (or other interpolant method) enables determination of dose values from measured net optical densities. Further film pieces may now be irradiated with complex dose deliveries, the delivered dose distribution along the plane of the films' sensitive layer will be recorded and may be read out and converted to dose values for interrogation of the delivery quality.

In practice, for dosimetry in radiotherapy applications the red colour channel is most often used as it provides the best sensitivity up to doses of 8-10 Gy. The green channel is used to measure higher dose values (Papaconstadopoulos, 2014) while the blue channel offers homogeneity correction (Chen, 2016).

Radiochromic film represents an effective solution for dosimetry in SBRT as it is high spatial resolution, near water equivalent in response (Huet, 2014) and does not require chemical processing to develop (Low, 2011). Film dosimetry offers a planar two dimensional measurement of dose distributions and has been used extensively within intensity modulated radiation therapy (IMRT) quality assurance. However, dosimetry with radiochromic film possesses significant limitations, particularly in adaptive radiotherapy, as it is not a real-time dose measurement tool and demands a strict calibration and handling protocol to achieve an acceptable accuracy (Tyler, 2013).

2.4.2.5 Semiconductor (silicon) detectors

Diodes are generally composed of crystals of semiconductor (i.e. silicon, germanium etc.) where the energy of electrons within the crystal (or amorphous solid) are described by electronic band structure theory. Band structure theory describes the ranges of energy an electron may possess (known as bands, a continuum of acceptable energy levels) and may not possess (known as band gaps, ranges of forbidden energies) as a part of the crystal lattice structure of the solid, a result of obeying the Pauli Exclusion Principle (Mayles, 2007).

The controlled introduction of impurities (known as doping) alters the electronic characteristics (i.e. electrical conductivity) of the crystal. Impurities refer to the additional ions of alternate elements to the main constituents of the crystal which when introduced may act as either an electron donor or electron acceptor within the crystal. Doping with electron donor elements causes an excess of electrons (negative charge carriers) and produces an n-type semiconductor whereas doping with electron acceptor elements creates a deficit of electrons (or excess of electron holes, positive charge carriers) and produces a p-type semiconductor (Rosenfeld, 2020).

The most common form of diode for radiation dosimetry is the p-n diode which is composed of the junction of a p-type (positive majority charge carrier, excess of electron holes) semiconductor with

an n-type (negative majority charge carrier, excess of electrons) semiconductor. At the junction of the two semiconductors the confluence between the excess electrons and excess holes produces a region devoid of charge carriers (known as the depletion region). The terminals of the p-n diode are attached to the n-type region (the cathode) and the p-type region (the anode). When a sufficiently high voltage (of the correct polarity) is applied to the cathode the width of the depletion region is narrowed until forward conduction of the majority charge carriers is allowed. The nature of the p-n junction prevents the movement of electrons in the opposite direction.

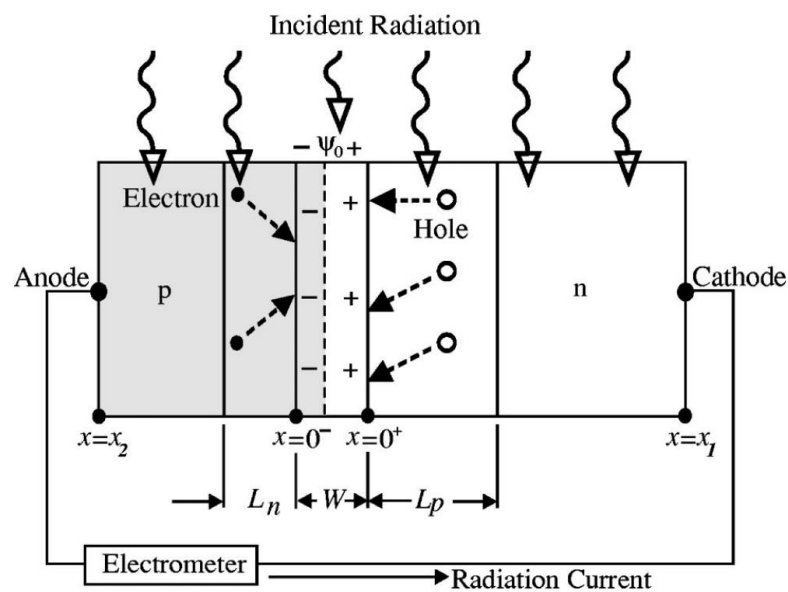


Figure 2.9 Schematic diagram of a silicon p-n junction as a radiation detector. The incident radiation generates excess electron (●) and hole pairs (○) which diffuse, over one diffusion length L_p , to the p-n junction and are subsequently swept across by the built-in potential and collected by the electrometer (Shi, 2003). Figure reproduced with permission from Wiley.

Ionising radiation traversing the semiconductor junction (which forms the sensitive detection volume of the diode) generates electron-hole pairs by collision processes (either directly or indirectly) along its track through the crystal lattice, Figure 2.9. For dosimetry, the quantity of practical interest is the average energy lost by the primary ionising particle which is necessary to produce an electron-hole pair within the crystal, known as the ionization energy. This quantity is independent of incident radiation type and energy and provided the particle is fully stopped within the sensitive volume of the detector, allows interpretation of the number of electron-hole pairs generated as an indicator of the energy absorbed within the diode as a result of irradiation. The

production of the majority and minority charge carriers in the form of electron-hole pairs and their consequent movement within the semiconductor junction forms an electrical current within the diode which is collected and measured. The magnitude of the collected current within the junction under irradiation may be related to the delivered radiation dose under known conditions.

For reliable dosimetry using semiconductor detectors the correction factors and dependencies which need to be considered include:

- Diode Calibration –
 - For single point diodes it is necessary to calibrate the response of the diode to a known radiation dose to convert charge collected to dose (Gy).
 - For arrays consisting of multiple diodes it is also necessary to expose the diodes to a uniform stimulus to identify the independent intrinsic gains and sensitivities (resulting from manufacturing tolerances in diode doping and pre-amplifier gain) in each channel and correct for the discrepancies.
- Temperature Dependence – diode response is expected to increase with ambient temperature (Welsh, 2001). This effect may be attributed to the increasing thermal energy of the charge carrying electrons.
- Directional Dependence – the geometrical construction and packaging of diodes is commonly asymmetrical, i.e. the shape, composition and relation of components (terminals, etc.) to one another is different for different orientations. This asymmetry can affect the response of the detector to irradiation as the beam traverses the diode at different angles of incidence (Jursinic, 2009). Correcting for directional dependence is vital for reliable dosimetry with semiconductor detectors in rotational treatment modalities. Semiconductor diodes exist which exhibit minimal directional dependence as a result of improved fabrication technology and packaging design (Petasecca, 2015).
- Dose Dependence – semiconductors suffer ongoing radiation damage affects with increasing accumulated dose as atoms within the crystalline lattice are displaced forming recombination centres which capture charge carriers. This effect reduces sensitivity as it limits charge carrier collection. The effects of dose dependence in diodes are reduced by pre-irradiation (American Association of Physicists in Medicine Radiation Therapy Task

Group 62, 2005).

- Energy Dependence – diodes are composed of high effective atomic number materials (i.e. silicon doped with phosphorous or boron) and thus are not directly tissue equivalent for all photon energies (especially low energies) (Mayles, 2007).


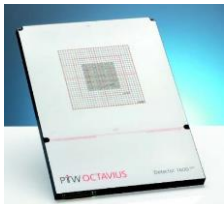




Silicon diodes are commonly used in small field dosimetry (Tyler, 2013) and the quality assurance of complex radiotherapy modalities as both point detectors and arrays. Diodes may be designed and fabricated with a small sensitive area and size, and arrays of diodes can possess submillimeter spatial resolution, especially in the case of a monolithic diode array topology (Wong, 2010). Silicon diodes are not tissue equivalent but dependencies upon energy, dose-rate, temperature and angle of radiation incidence can be corrected.

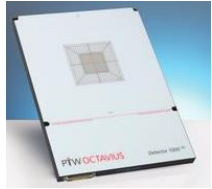
The metal oxide field effect transistor (MOSFET) dosimeter is technologically similar to a semiconductor diode but is composed of semiconductor silicon substrate, a layer of insulating oxide and a metal gate. The MOSFET as a dosimeter shares similar advantages and disadvantages with a diode such as; small sensitive volume, temperature dependence, directional dependence and energy dependence. Due to the increased complexity of the MOSFET junction they are not as readily available in the form of pixelated arrays.

2.4.2.6 (Pixelated) Array Detectors

Pixelated detectors or array detectors are a composite dosimeter in which numerous individual detectors are combined together in a structured geometric pattern to form an array for simultaneous measurement across a plane or volume in a radiation field. These detector arrays are generally composed of a series of semiconductor dosimeters or ionisation chambers forming the individual pixels. The following table summarises the available commercial pixelated array detector systems for radiation dose measurements and patient specific QA in EBRT, Table 2.1.

Table 2.1 Currently available commercial detector array systems, summarizing properties of both 2D and 3D dose acquisition systems (*OCTAVIUS 4D - PTW Freiburg GmbH, 2020; ArcCHECK® - Sun Nuclear, 2020; Products, 2020; MapCHECK® 3 - Sun Nuclear, 2020; OCTAVIUS Detector 1600 SRS - PTW Freiburg GmbH, 2020; SRS MapCHECK® - Sun Nuclear, 2020*).

			
Detector:	SRS MapCHECK®	OCTAVIUS Detector 1600 SRS	MapCHECK® 3
Company:	Sun Nuclear	PTW	Sun Nuclear
Detector Type:	SunPoint® 2 diode detectors	Plane-parallel, liquid-filled ionization chambers	SunPoint® 2 diode detectors
Number of Detectors:	1013	1521	1527
Detector Spacing:	2.47 mm (centre-to centre), Checkerboard pattern: X & Y – 3.5 mm	2.5 mm in centre area (6.5 x 6.5 cm ²), 5.0 mm in outer area (15 x 15 cm ²)	7.07 mm (centre-to-centre), checkerboard pattern; X & Y – 10 mm
Detector Size:	0.48 x 0.48 mm (0.007 mm ³)	2.3 x 2.3 x 0.5 mm ³ 0.003 cm ³ (3 mm ³)	0.48 x 0.48 = 0.23 mm ² (0.007 mm ³)
Array Size: (mm ²)	77 x 77	150 x 150	320 x 260
Dose Distribution Analysis (i.e. 2D or 3D)	2D	3D (using Octavius 4D phantom)	2D
Weight	1.9 kg	5.9 kg	5.6 kg
			
Detector:	OCTAVIUS® 1500	MatriXX Evolution	MatriXX FFF
Company:	PTW	IBA	
Detector Type:	Plane-parallel vented ionization chambers	Air-vented parallel ionization chambers	
Number of Detectors:	1405	1020 (~ 32 x 32 grid)	
Detector Spacing:	7.1 mm (centre-to-centre), checkerboard pattern; X & Y – 10 mm	7.62 mm (centre-to-centre), matrix/grid pattern	
Detector Size:	4.4 x 4.4 x 3 mm ³ (60 mm ³)	4.5 (Φ) x 5 (h) mm ³ (80 mm ³)	4.5 (Φ) x 2 (h) mm ³ (32 mm ³)
Array Size: (mm ²)	270 x 270	244 x 244	
			320 x 260

Dose Distribution Analysis (i.e. 2D or 3D)	3D (using Octavius 4D phantom)	2D	2D
Weight	6.0 kg	10 kg	7.1 kg
			
Detector:	Delta4+	ArcCHECK®	OCTAVIUS® 1000 SRS
Company:	Scandidos	Sun Nuclear	PTW
Detector Type:	p-Si diodes	SunPoint® diode detectors	Plane-parallel, liquid-filled ionization chambers
Number of Detectors:	1069 (distributed on coronal and sagittal planes)	1386	977
Detector Spacing:	5 mm (central 6x6 cm ² area), 10 mm (outer area)	10 mm Helical Grid (HeliGrid)	2.5 mm (centre-to-centre) in centre (5.5 x 5.5 cm ²), 5 mm (centre-to-centre) in outer area (11 x 11 cm ²)
Detector Size:	2 (Φ) x 0.05 (h) mm ³ (0.04 mm ³)	0.64 mm ² (0.019 mm ³)	2.3 x 2.3 x 0.5 mm ³ 0.003 cm ³ (3 mm ³)
Array Size: (mm ²)	Max. field size: 200 x 200 mm ² (200 x 380 mm ² with merging)	210 x 210 (Array diameter x length)	110 x 110
Dose Distribution Analysis (i.e. 2D or 3D)	3D	3D	3D (using Octavius 4D phantom)
Weight	27 kg	15.4 kg	5.4 kg

2.4.3 Gamma Analysis

The measurement of an absorbed dose distribution by a detector system in two dimensions or three dimensions necessitates a method for quantifiable evaluation of the measured distribution compared to an expected (or reference) dose distribution. Quantifying the agreement between a measured and expected dose distribution is uniquely important for commissioning of a TPS, commissioning a new treatment technique and patient specific QA, the complexity of these tasks is compounded by the presence of small area radiation beams and steep dose gradients. One methodology for evaluation

of two and three dimensional distributions is through the use of gamma analysis.

Gamma analysis (Low, 1998) combines a distance to agreement criterion with a dose-difference criterion. It compares the dose difference at various points of interest in a measured and comparison dose distribution and evaluates the distance between points with the same magnitude of dose. The distance to agreement component is particularly important for measurements within high dose gradient regions. This method of gamma analysis can be summarised by defining two acceptance parameters; ΔD_M and Δd_M as the dose-difference criterion and distance-to-agreement criterion respectively.

The one-dimensional representation of the application of the dose and distance difference criterion for evaluation, gamma analysis, between two dose measurements, with one spatial dimension, is shown in Figure 2.10, the (measured) point of interest to be evaluated is at the origin, $D_m(x_m), x_m$.

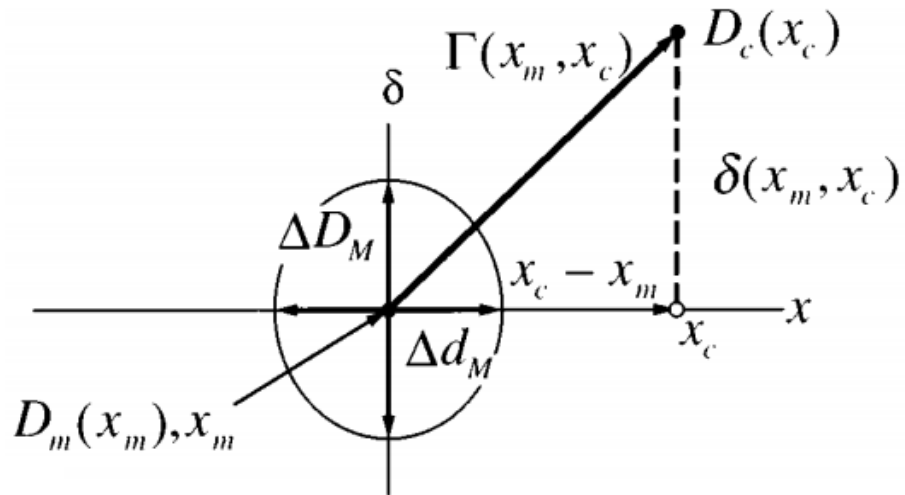


Figure 2.10 One-dimensional representation of dose-difference and distance to agreement evaluation between dose values which possess one spatial dimensions (Low, 1998). Figure reproduced with permission from Wiley.

The abscissa represents the spatial location of the points; measurement (x_m) and comparison (x_c), and the difference in spatial location is evaluated between them, i.e $x_c - x_m$. The ordinate represents the magnitude of dose of the points; measurement ($D_m(x_m)$) and comparison ($D_c(x_c)$), and the difference in dose magnitude is evaluated between the points, δ .

The two-dimensional representation of gamma analysis, utilizes an ellipsoidal surface to evaluate the dose-difference and distance to agreement simultaneously between points, shown in Figure 2.11. In this two-dimensional example the spatial notation is extended to be a vector of the two-dimensional location of each of the dose points. The evaluation of the gamma value between points can be further extended to a three-dimensional analysis.

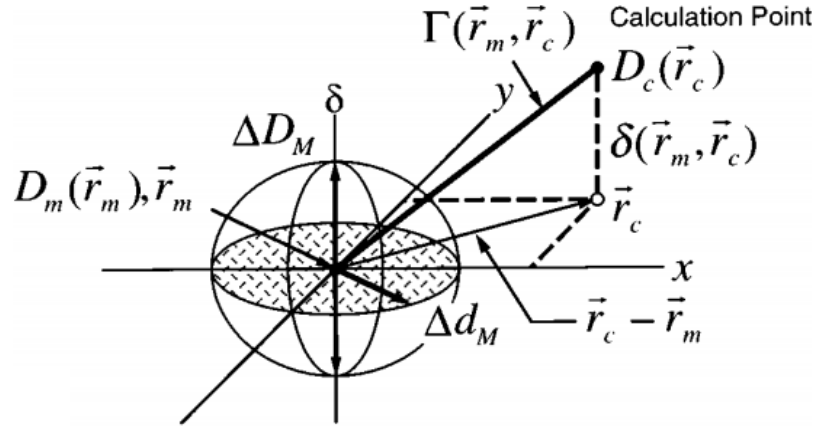


Figure 2.11 Two dimensional representation of gamma analysis using the ellipsoid dose difference and distance to agreement evaluation method (Low, 1998). Figure reproduced with permission from Wiley.

The surface of the ellipsoid, shown in Figure 2.11, describes the limits of acceptance and is defined by the following equation:

$$1 = \sqrt{\frac{r^2(\vec{r}_m, \vec{r})}{\Delta d_m^2} + \frac{\delta^2(\vec{r}_m, \vec{r})}{\Delta D_m^2}} \quad (2.4)$$

Where:

$$r(\vec{r}_m, \vec{r}) = |\vec{r}_m - \vec{r}| \quad (2.5)$$

$$\delta(\vec{r}_m, \vec{r}) = D(\vec{r}) - D_m(\vec{r}_m) \quad (2.6)$$

If any portion of the compared point $D_c(r_c)$ in Figure 2.11 intersects with the defined ellipsoids surface, the calculation is said to have passed at \vec{r}_m . A generalized acceptance criteria calculation can be defined using the right hand side of equation (2.3), Γ .

$$\Gamma(\vec{r}_m, \vec{r}) = \sqrt{\frac{r^2(\vec{r}_m, \vec{r})}{\Delta d_m^2} + \frac{\delta^2(\vec{r}_m, \vec{r})}{\Delta D_m^2}} \quad (2.7)$$

Points lying inside (and including) the surface of the ellipse, with axes having the criteria values, have a gamma value equal or smaller than one and therefore pass. That is, if $\gamma \leq 1$, pass or if $\gamma > 1$, fail. This evaluation method allows for a quantitative evaluation of the agreement between two-dimensional and three-dimensional dose distributions.

2.4.4 Charged Particle Range Verification

Verification of the constancy of radiation beam performance characteristics is a vital component of a routine QA program for the delivery of radiotherapy (Arjomandy, 2019). However, extensive or time consuming QA measurements and processes limit the time a machine is available for patient treatment.

The deposition of dose by charged particles within a small volume at the Bragg peak is uniquely sensitive to the particles penetration range, and it is directly dependent upon the incident beam energy and any small variations in material density and stopping power along the beam path (Mirandola, 2018). Significant tumour under/over dosage can be the result of incorrect estimation of in-patient beam penetration (Paganetti, 2012). The routine measurement and verification of PDD curves of Bragg peaks for charged particle radiotherapy delivery systems is vital to ensure safe provision of radiotherapy treatment (Cantone, 2013). Unfortunately, devices providing a means of fast verification (for daily measurement) of beam energy stability in-phantom with high precision, accuracy and reliability are not readily available.

In charged particle radiotherapy, measurements of the PDD distribution are routinely performed, commonly measured using an ionization chamber and a computerized scanning water tank dosimetry system. The measurement of the PDD distribution along the central axis of the charged particle radiation beam is time-consuming with a scanning water tank due to the prolonged and complex setup. Other dosimetry systems are available for verification of charged particle range/energy in-phantom.

Multi-layer ionization chamber (MLIC) systems are devices which are composed of a stack of numerous parallel plate ionization chambers sharing a single central axis of measurement (Yajima, 2009). These systems can be aligned to the central axis of the incident charged particle radiation beam for fast measurement of charged particle depth dose distributions. The Zebra (IBA dosimetry, Schwarzenbruck, Germany) is an MLIC consisting of 180 independent 2.5 cm diameter circular vented plane parallel ionization chambers with a 2 mm native resolution (Dhanesar, 2013), Figure 2.12. The Zebra system is a bulky device with a mass of 10 kg and measuring 43.9 cm x 19.5 cm x 17.5 cm (*Zebra - Scan monolayer & SOBP measurements / IBA Dosimetry, 2020*).



Figure 2.12 The Zebra multi-layer ionization chamber device (*Zebra - Scan monolayer & SOBP measurements / IBA Dosimetry, 2020*).

Radiochromic films in solid slab phantoms provide another means of charged particle range

verification in-phantom. Film dosimetry provides significant advantages in high spatial resolution, however also significant disadvantages in the time-consuming film processing requirements, and for charged particles specifically, significant energy dependence in the region of the Bragg peak (Castriconi, 2017).

Prompt Gamma Emission (PGE) and Positron Emission Tomography (PET) are potential imaging modalities which offer potential for accurate proton range verification.

Positron Emission Tomography for range verification utilises coincident gammas which result from the annihilation of emitted positrons with electrons, as a small fraction of protons traversing the medium will produce positron emitting isotopes (Rutherford, 2020). A PET camera can be used to observe the recombination of emitted positrons with an electron in the surrounding material. This method can be performed either 'off-line', after treatment or 'on-line', during treatment (Knopf, 2013). The beam range is able to be verified by PET imaging, in clinical head-and-neck patients to well-co-registered bony structures, to an accuracy of 1-2 mm (Parodi, 2007).

Prompt Gamma Emission is an indirect method which measures the emission of single photons (prompt gammas) which follow the inelastic collisions (and excitations) between the nuclei of the target and the incident protons. A direct correlation exists between the point of emission of the prompt gamma photons in the material and the range of the incident protons upon the material (Zarifi, 2017). This method is useful for online in-vivo verification as the time between excitation/de-excitation of the target nuclei and detection of the prompt gamma photon is of the order of nanoseconds (Knopf, 2013). This method has reported position verification accuracy of 1 to 2 mm at the Bragg peak of 100 MeV proton beam in a phantom (Min, 2006).

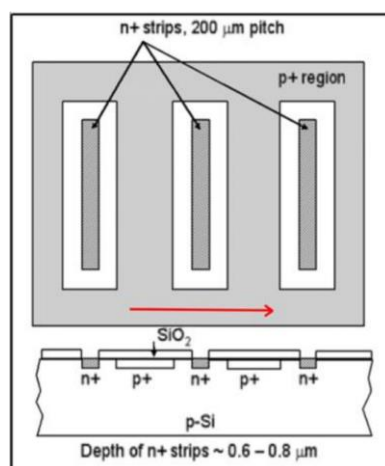
2.5 Devices designed by Centre for Medical Radiation Physics

2.5.1 Serial Dose Magnifying Glass (sDMG)

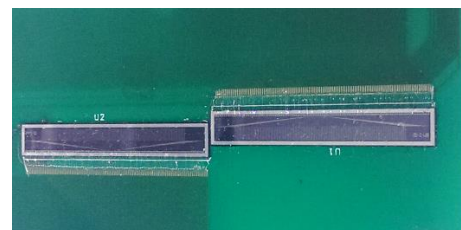
The Serial Dose Magnifying Glass (sDMG) is a multi-strip silicon detector designed by the Centre for Medical Radiation Physics (CMRP) and is comprised of two linear arrays arranged in sequence with each individual array consisting of 128 diodes, with physical thickness 0.04 mm, separated

with pitch 0.2 mm and each diode presenting a sensitive strip area of $0.02 \times 2 \text{ mm}^2$. The sDMG consists of n^+ silicon strips implanted upon a thin p-type silicon substrate and is operated in passive mode (without an external bias voltage applied). This linear array is based upon the technology of the Dose Magnifying Glass (DMG), which has been investigated for use in radiotherapy QA (Wong, 2011), IMRT QA (Wong, 2010) and helical tomotherapy QA (Wong, 2011). The density of silicon is 2.33 g/cm^3 thus the water equivalent thickness of each individual diode along the axis of the linear array is approximately 0.466 mm and perpendicular to the axis of the linear array is $0.0186 \mu\text{m}$.

The sDMG is composed of two linear arrays with a physical gap separating the linear arrays of 0.6 mm. The arrays are wire bonded end-to-end, to a flexible printed circuit board (PCB) which is 0.5mm thick, providing the connections to the readout electronics and data acquisition (DAQ) system. The single axis of detection of the sDMG measures a length of 50.8 mm. The detector and PCB are enclosed within a rigid holder composed of two slabs of recessed Solid Water (GAMMEX, WI, USA) material, 5 mm thickness each, to provide protection, rigidity and appropriate scattering conditions around the detector. The upper Solid Water slab which encompasses the detector is machined with a 2mm recess into the Solid Water larger than the dimensions of the detector, in which the detector sits, this leaves a 1.6mm air gap above the detector and a 1mm air gap surrounding the detector.



(a)



(b)

Figure 2.13 The Serial Dose Magnifying Glass (sDMG). (a) Schematic diagram of silicon strip detector, DMG (Debrot, 2018). (b) sDMG mounted and wired bonded to a thin printed circuit board (PCB). Figure 2.13(a) reproduced with permission from Wiley.

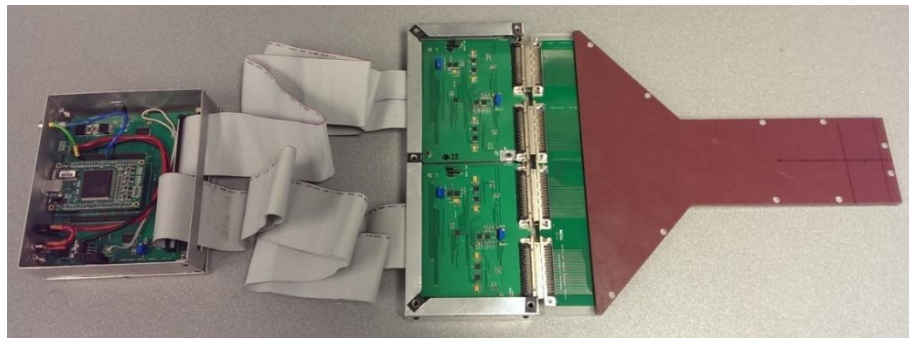


Figure 2.14 sDMG enclosed within Solid Water phantom and connected to data acquisition system.

2.5.2 Monolithic silicon detector array (DUO)

DUO is a monolithic silicon detector array designed by the CMRP and comprised of 505 silicon diodes arranged in two bisecting orthogonal linear arrays of 253 diodes, sharing a common central pixel. This form of the DUO detector array investigated was fabricated on a bulk p-type silicon substrate with thickness of $470\ \mu\text{m}$ and with a total area of $52 \times 52\ \text{mm}^2$. The individual diodes present a sensitive volume of $0.04 \times 0.8\ \text{mm}^2$ with diode pitch of $0.2\ \text{mm}$. The array is wire bonded to a $50\ \mu\text{m}$ thick printed circuit board which provides the connections to the data acquisition (DAQ) system for readout.

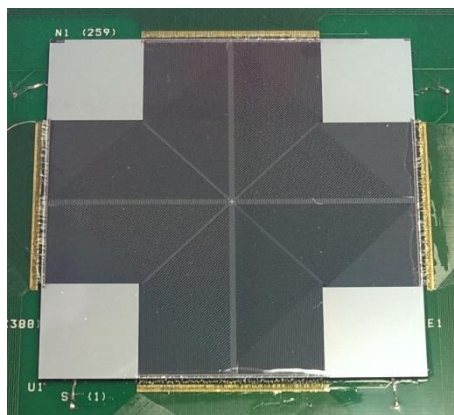


Figure 2.15 The DUO detector mounted and wire bonded to the thin PCB.

The central pixel of the DUO array is $0.18 \times 0.18 \text{ mm}^2$, the four pixels which directly surround the central pixel are $0.16 \times 0.2 \text{ mm}^2$, and the subsequent pixels which compose the orthogonal arms of the array are $0.04 \times 0.8 \text{ mm}^2$. The separation between each detector pixel in the DUO array is 0.2 mm. The monolithic silicon array and the PCB are enclosed between two recessed slabs of PMMA, each 5 mm thick, to provide protection, rigidity and scattering to the detector.

DUO is operated without an external bias applied to the p-n junctions. The performance of DUO for small field dosimetry has previously been reported including a detector characterization for dose-per-pulse dependence, dose-rate response, radiation damage, output factor, PDD and beam profiling (Al Shukaili, 2017).

2.5.3 Data Acquisition System

The data acquisition (DAQ) system utilised to readout the sDMG detector and DUO was designed and developed by CMRP and is based upon a custom-design multi-channel electrometer with Field Programmable Gate Array (FPGA) interface.

2.5.3.1 AFE

The electrometer, AFE0064 (Texas Instruments, Dallas, USA), is a current integrator and possesses 64 parallel input channels and two differential outputs. The current is measured individually from each detector channel and integrated over a capacitor for a user defined time-interval, the resulting output charge is normalised to the nominated dynamic scale, from 0.13 to 9.6 pC.

The DAQ system utilised in conjunction with the sDMG is comprised of four AFE0064 chips serving 256 individual channels and readout by two analogue to digital converters (ADC), with a resolution of 16 bit. The system utilised in conjunction with the DUO detector is comprised of eight AFE0064 chips serving 512 individual channels for readout by four ADC's with a resolution of 16 bit.

Synchronisation of the electronics is managed by the FPGA; enabling measurement, acquisition and transfer of data from the electrometers to the host computer via a USB2.0 communication protocol. Acquisition of data from the AFE0064 chips is triggered and synchronised by the FPGA to the

electron gun trigger pulses of the linac by a coaxial connection between the FPGA and the linacs sync pulse (Varian). An internal trigger generator can also be used to acquire signal from the detector, up to a frequency of 10 kHz, in case of irradiation by a continuous radiation source. For further information about the performance and design details of the AFE DAQ please refer to Fuduli et al. (Fuduli, 2014).

For the experiments described in Chapter 3, Chapter 4 and Chapter 5, the detectors used, were readout using the AFE DAQ technology.

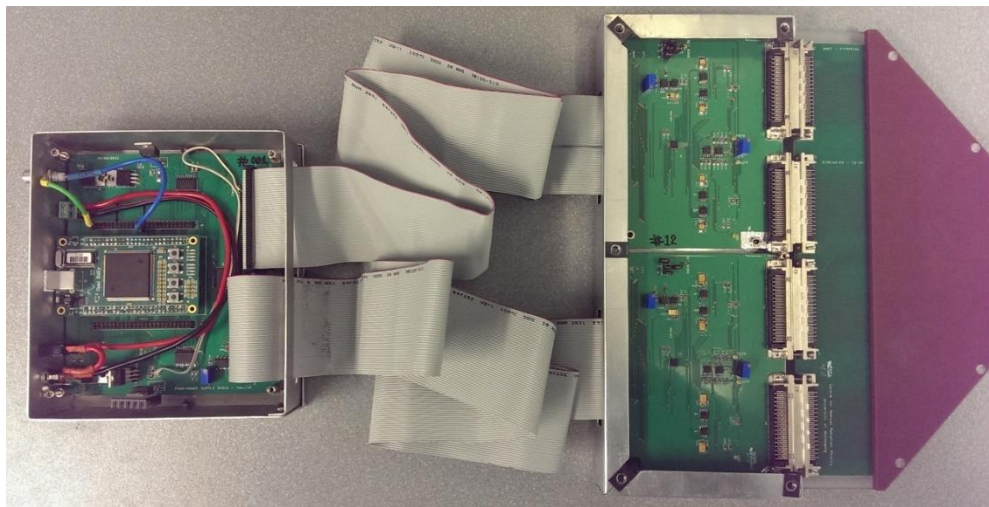


Figure 2.16 The sDMG detector connected to the AFE DAQ system with FPGA.

2.5.3.2 TERA

The TERA06 is a readout electrometer consisting of 64 channels per chip. The TERA06 chip is based on a charge to frequency converter and digital 16-bit counter, referred to as an application specific integration circuit (ASIC). The TERA06 DAQ system reads out the 256 detector channels of the sDMG with zero dead time and provides a large dynamic range and high temporal resolution (Fuduli, 2014). The sDMG is readout by four TERA06 chips synchronized and managed by the FPGA, connected to a personal computer by USB 2.0 interface.

2.5.4 Graphical User Interface

The graphical user interfaces (GUIs) which are used for; connection to the DAQ, acquisition of data

from the detector, visualisation and analysis, are designed by CMRP. The sDMG and DUO detectors utilise GUIs with different visualisations configurations, Figure 2.17 for sDMG and Figure 2.18 for DUO respectively, but the underlying architecture, programming and communication of the software with the DAQ is identical. The GUI is compiled in the C++ programming language and designed and developed using the Qt cross-platform software development toolkit. The USB connection between the dynamic language libraries and the DAQ is managed by the GUI, which initializes the USB connection and sends the necessary firmware to the FPGA. From the GUI the user is able to alter the data acquisition settings, which include (but are not limited to); integration time, acquisition time, acquisition frequency, gain, buffer size and external or internal generated trigger. Data acquired from the detector is displayed to the user in real time with both instantaneous response and integral response displayed in a logical representation of the geometry of the detector. Once acquisition is complete the user can save the file in an encoded file format, which can be decoded and visualised at any time for post-acquisition analysis.



Figure 2.17 The AFE-Histogram graphical user interface (GUI) for acquisition, visualisation and analysis of sDMG measurements.

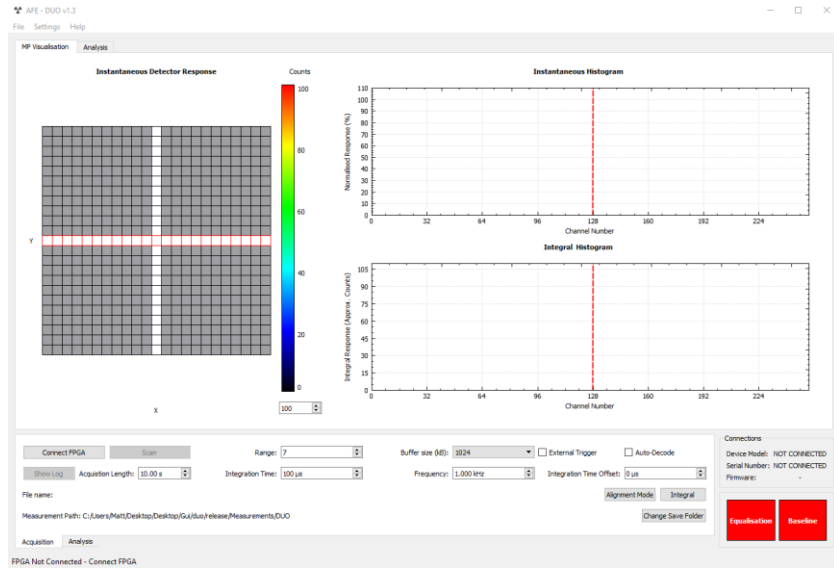


Figure 2.18 The AFE-DUO graphical user interface (GUI) for acquisition, visualisation and analysis of DUO measurements.

Chapter 3

Device characterisation of Serial Dose Magnifying Glass (sDMG)

3.1 Introduction

To independently assure the quality of planned treatments that use small radiation fields requires a unique instrument which combines high spatial and high temporal resolution. The sDMG is a multi-strip 1D silicon detector array to realize the requirements for an independent dosimetry tool for patient specific quality assurance and pre-treatment verification in real-time adaptive radiotherapy using small radiation fields matching, within the technological limitations of the number of channels able to be readout simultaneously for this project, the resolution required for an optimal dose profile reconstruction. This chapter first evaluates an optimum spatial resolution which would be necessary to reconstruct quantifiable detail in measured beam profiles and then presents the results obtained from the sDMG detector, with AFE readout, which will be compared to the gold standard detectors adopted clinically: the ionisation chamber and radiochromic film, under identical experimental conditions within each investigation.

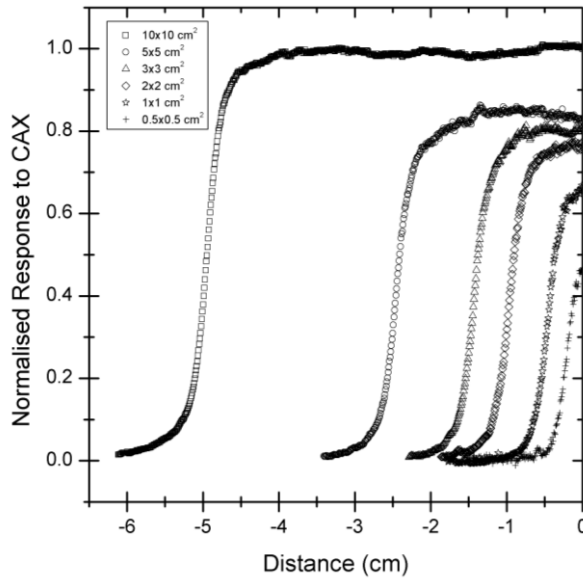
3.2 Materials and Methods

3.2.1 Evaluation of the spatial resolution required by a pixelated detector

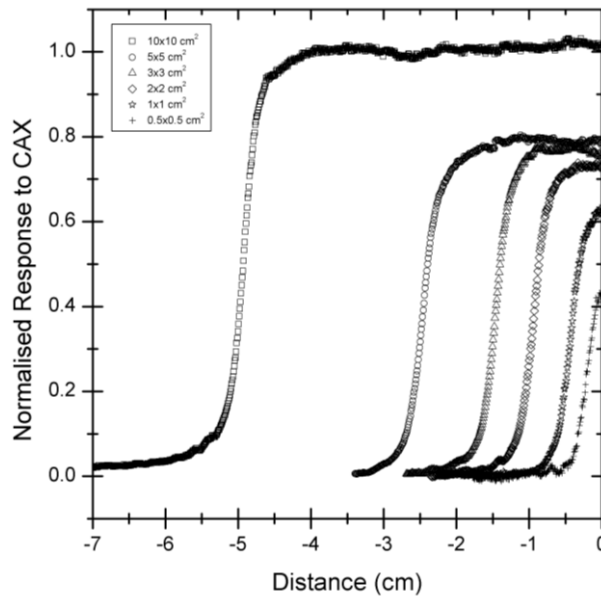
The optimum resolution required to reconstruct beam profiles in SRT modalities has never been

assessed using discrete-time Fourier analysis of measured high resolution EBT3 film beam profiles. This work presents an analysis of high resolution radiochromic film data conducted to generate recommendations for the pixel separation required to accurately measure the beam penumbra and profile.

Gafchromic EBT3 film (Ashland Advanced Materials, NJ, USA) represents the best option for high spatial resolution measurement of radiotherapy small field beams. In applications where real-time dosimetry is crucial, they must be substituted with a pixelated detector which should have comparable performance. A method has been established to evaluate the minimum spatial resolution required by a strip detector to measure the dose profile of jaw-defined square fields with the same accuracy of an EBT3 film readout at high resolution. The method has been applied to various beam sizes delivered by a 6MV Varian Clinac iX (Varian Medical Systems, Palo Alto, USA) medical linear accelerator (linac) at depths of 5 cm and 10 cm in a Solid Water (Standard Imaging, Madison, USA) block phantom. The EBT3 film pieces were scanned six times each using a MicroTek scanner (MicroTek, Hsinchu, Taiwan) before and 72 hours after irradiation in 48 bit RGB colour mode with a scanning resolution of 300 dpi (corresponding to 84.7 μm pixel size) and saved in .TIFF format. The images were analysed using ImageJ 1.47v where a second-order polynomial generated from an associated calibration curve was used upon the red colour channel to convert from pixel value to dose via a net optical density protocol. Line profiles were extracted along the central axis of the EBT3 film pieces for comparison. The dose profiles were normalised to the central axis (CAX) response of the 10 x 10 cm^2 field for the corresponding depth. Figure 3.1 illustrates the results of the line profiles extracted from the high resolution film scans for the various field sizes and depths in Solid Water.



(a)



(b)

Figure 3.1. Dose profiles for various field sizes measured in a Solid Water block phantom using EBT3 film. (a) At depth 5 cm in Solid Water field sizes 0.5x0.5 cm² to 10x10 cm². (b) At depth 10 cm in Solid Water field sizes 0.5x0.5 cm² to 10x10 cm².

In this initial study, the penumbral width (PW) was defined as the distance between either the 3% and 97% ($PW_{3-97\%}$) response values or the 20% and 80% response values ($PW_{20-80\%}$) and was measured on the left hand side (LHS) of the normalised dose profiles for all field sizes investigated. The full-width at half-maximum (FWHM) was also determined.

Within the scope of modern radiotherapy treatment modalities steep dose penumbrae are necessary to achieve highly conformal treatments. Accurate reconstruction of the penumbral features is necessary as treatment margins are reduced and the steep dose gradients generated by sharp field penumbrae approach critical organ boundaries.

Further investigation into the resolution required by a detector to reconstruct the penumbra in small field applications was conducted using discrete-time Fourier analysis to identify the frequency composition of the penumbral structures for different field sizes. For a discrete signal x_n with a finite-duration, sampled at N points with frequency k , the Fourier series representation of the sequence is:

$$x_n = \frac{1}{N} \sum_{k=0}^{N-1} X_k \cdot \left[\cos\left(\frac{2\pi}{N}kn\right) + i \sin\left(\frac{2\pi}{N}kn\right) \right] \quad (3.1)$$

The discrete Fourier Transform (DFT) (Oppenheim, 1999) is:

$$X_k = \sum_{n=0}^{N-1} x_n \cdot e^{-i(2\pi/N)kn} \quad (3.2)$$

And the normalised amplitude $|X_k|/N$, is defined as:

$$\frac{\sqrt{\text{Re}(X_k)^2 + \text{Im}(X_k)^2}}{N} \quad (3.3)$$

The bandwidths ($\text{BW}_{90\%}$) of the Fourier spectra generated in this work are defined as the width of the frequency band that contains 90% of the total area under the amplitude spectrum. The Nyquist-Shannon sampling theorem was applied to the identified frequency bandwidths for each field size's penumbral spectrum to calculate a recommended sampling resolution to accurately reconstruct the penumbra.

$$\text{Nyquist Resolution} = \frac{1}{2 \cdot \text{BW}_{90\%}} \quad (3.4)$$

3.2.2 Radiation Hardness Characterisation

The response of the sDMG detector was measured under irradiation by a photon beam from a 6 MV linac (Varian Medical Systems, Palo Alto, USA). The detector was positioned at 1.5 cm depth (d_{max} for 6 MV photons) in a phantom composed of Solid Water. The detector was then irradiated up to 40 kGy using a Co-60 gamma emission source in steps of 20 kGy without a bias applied to the detector during irradiation to mirror the standard operation procedure of the detector during clinical use. The response of the detector was then measured and recorded under 6 MV photon irradiation at 0, 20 and 40 kGy absorbed doses to evaluate the effect of radiation damage upon the detector response.

3.2.3 Dose Linearity

The linearity of the detector's response was examined and verified. The detector was positioned within a Solid Water phantom at a depth of 1.5 cm and irradiated using a 6 MV photon beam from a linac with a field size of 10 x 10 cm² and source to surface distance (SSD) of 100 cm. The delivery ranged from 50 MU to 500 MU at 600 MUmin⁻¹, corresponding to a dose range of 50 cGy to 500 cGy at these conditions in 50 cGy dose increments.

3.2.4 Dose per Pulse Dependence

An investigation into the dose per pulse dependence (DPP) of the sDMG detector was carried out within the range of 2.1x10⁻⁵ Gy pulse⁻¹ to 2.78x10⁻⁴ Gy pulse⁻¹. This was undertaken utilising a 6 MV linac beam with dose-rate 600 MU min⁻¹ and field size 10 x 10 cm². The detector was positioned at a depth of 1.5 cm (d_{max} for 6 MV photons) with 10 cm of backscattering material in a water equivalent phantom, the source to surface distance (SSD) was varied sequentially from 100 cm to 366 cm and the detector response tested by irradiating the detector with a 10 x 10 cm² field size (at 100 cm SSD). The detectors depth in the phantom remained constant for all measurements to minimise variation in the detectors response, which may be attributed to changes in the energy

spectrum of the incident radiation beam. A reference data set was collected through the repetition of the experiment utilising a CC13 (IBA Dosimetry, Schwarzenbruck, Germany) ionisation chamber in place of the sDMG detector. The response of the sDMG was normalised to the response of the ionisation chamber for each measurement point to quantify the detectors dependence upon dose per pulse values compared to the ionisation chamber.

3.2.5 Percentage Depth Dose Measurements

The detector is secured and encapsulated within a protective holder composed of two 5 mm pieces of Solid Water. The sDMG detector and holder was positioned between 30 x 30 cm² sections of Solid Water material to form a volume surrounding the detector possessing water-equivalent scattering conditions. A series of 30 x 30 cm² Solid Water slabs are placed beneath the detector, totalling 10 cm for backscattering and the amount of Solid Water above the detector is varied from 0.5 cm to 25 cm. The system is irradiated by a 6 MV linac photon beam with field size 10 x 10 cm² at a constant source to surface distance (SSD) of 100 cm, delivering 100 MU for each depth. The response of the sDMG detector is compared to the response of a Markus ionisation chamber (PTW-Freiburg, Freiburg, Germany) irradiated in Solid Water utilising the same procedure.

3.2.6 Beam Profile Measurements

The clinical megavoltage photon beam possesses an axial profile composed of inter-umbral, penumbral and out of field regions. Linacs which utilise flattening filters exhibit inter-umbral regions of dose uniformity, whereas the penumbral region of a beam profile describes the rapid dose-falloff at the radiation field edges. For small field dosimetry and stereotactic treatments, the penumbral width measured between the 20% and 80% points of the maximum dose intensity is an important metric. The beam profiles of small fields of 0.5 x 0.5 cm², 1 x 1 cm², 1.5 x 1.5 cm², 2 x 2 cm², 3 x 3 cm², 4 x 4 cm² and 5 x 5 cm² defined by the collimation jaws, with the MLC retracted, were measured. The sDMG was positioned at a depth of 10 cm in a Solid Water phantom with 10 cm of backscattering material. The system was irradiated at 90 cm SSD using a 6 MV linac for 200 MU at 600 MU min⁻¹ for each of the field sizes investigated. The detector was aligned to the central axis of 0.5 x 0.5 cm² field such that the axis of detection of the sDMG bisected the square field.

The measurements were repeated using Gafchromic EBT3 film. The film was cut into 4 x 4 cm²

pieces for field sizes $3 \times 3 \text{ cm}^2$ and below and $6 \times 6 \text{ cm}^2$ pieces for the larger field sizes. The film was aligned and irradiated with each of the square fields investigated by the sDMG detector. Prior to exposure to the radiation fields, each film piece was scanned using a MicroTek scanner, in 48-bit RGB colour mode. The film pieces were positioned in the centre of the scanner field of view and scanned at 72 dpi (corresponding to a 0.353 mm pixel size). Six scans were conducted for each individual film piece, the results saved in .TIFF format, with the first three scans for each film piece discarded. This procedure was repeated 72 hours after radiation exposure with care taken to maintain the orientation of the film pieces before, during and after irradiation. A further set of films from the same batch were prepared and irradiated following the outlined protocol to produce a dose calibration curve. Analysis was conducted using ImageJ 1.47v where the red channel was used for the pixel value to net optical density to dose conversion based upon a second-order polynomial derived from the associated film calibration curve. Line profiles were extracted along the same axis of measurement as the sDMG from the dose converted images for comparison and quantitative analysis. The full-width at half-maximum (FWHM) and penumbral widths of the profiles were measured for both the EBT3 film and sDMG detector and subsequently compared.

3.2.7 Output Factor Measurements

The output factor is defined, within this study, as the ratio of the dose per monitor unit measured at the centre of the radiation field size under investigation relative to dose per monitor unit measured at the centre of a specific reference radiation field. The reference field size considered was $10 \times 10 \text{ cm}^2$ with all measurements conducted at 10 cm depth and 90 cm SSD (isocentre) with 6 MV photon beams.

The square radiation fields under investigation were aligned with the detector to ensure that the centre of the radiation field coincided with the centre of the sDMG detector, the response within these channels was utilised to calculate the output factor values. Radiation fields ranging in size from $0.5 \times 0.5 \text{ cm}^2$ up to $10 \times 10 \text{ cm}^2$ were investigated. The measurements were repeated using EBT3 film for direct comparison between sDMG and EBT3 film under identical conditions. The film was scanned with resolution 72 dpi, the acquisition and analysis of the EBT3 film followed the procedure outlined above (3.2.1).

3.3 Results

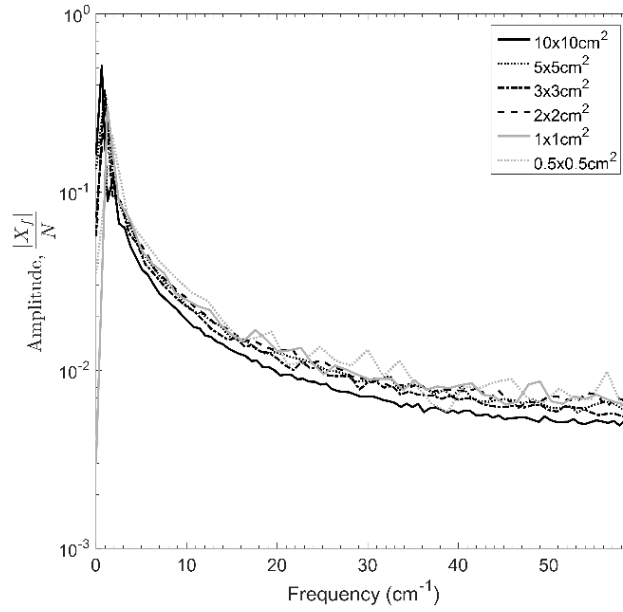
3.3.1 Evaluation of the spatial resolution required by a pixelated detector

The results of the measurements of FWHM and PW are presented in Table 3.1. It is evident that across the field sizes and depths investigated the $PW_{20-80\%}$ is shown to range between 2-3 mm. The $PW_{3-97\%}$ value ranges from 4-18 mm across the field sizes investigated as this metric incorporates both shoulders of the field penumbra. The distance over which the dose falls-off to zero is of the order of a few millimetres ($PW_{20-80\%}$) thus it is clear the penumbra of a jaw-defined square field contains steep dose gradients, Figure 3.1(a) and (b).

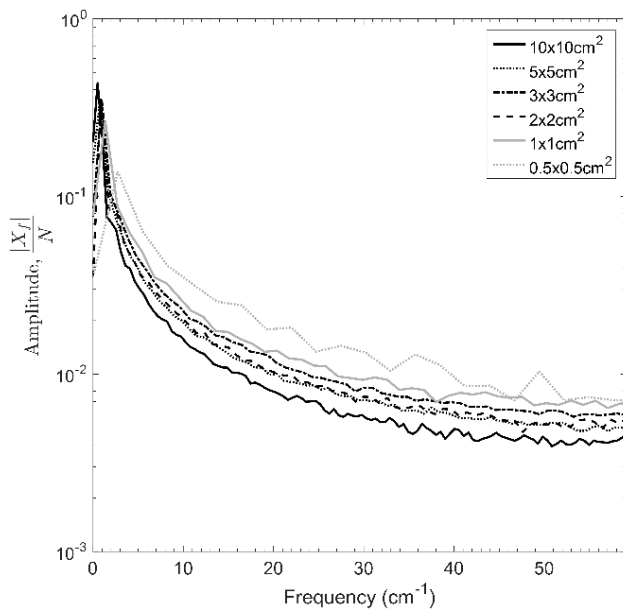
Table 3.1 Penumbral width (PW) and Full-Width at Half-Maximum (FWHM) measurements for EBT3 film dose profiles.

Square Field Size (mm)	Depth 5 cm			Depth 10 cm		
	$PW_{3-97\%}$ (mm)	$PW_{20-80\%}$ (mm)	FWHM (mm)	$PW_{3-97\%}$ (mm)	$PW_{20-80\%}$ (mm)	FWHM (mm)
100	15.79	3.12	103.84	18.65	3.20	105.47
50	12.19	3.28	51.50	12.51	3.22	52.41
30	10.57	2.97	30.01	10.97	3.04	31.35
20	9.69	2.92	20.34	9.96	2.94	20.13
10	6.64	2.55	9.88	7.30	2.57	10.57
5	4.16	1.98	4.88	4.87	2.05	5.07

Figure 3.2 illustrates the amplitude spectra generated from the calculation of the discrete Fourier transform of the 3–97% penumbral region response for the LHS of each field size investigated. Figure 3.2(a) presents the spectrums for the penumbrae of profiles acquired at 5 cm deep in a Solid Water phantom, Figure 3.2(b) shows the spectrums for profiles acquired at a depth of 10 cm in Solid Water.



(a)



(b)

Figure 3.2 One-sided Fourier amplitude spectra for the penumbral regions (3-97%) of various field sizes. (a) Fourier spectrums of profiles acquired at depth 5 cm in a Solid Water phantom. (b) Fourier spectrums of profiles acquired at depth 10 cm in a Solid Water phantom.

The bandwidths and Nyquist resolutions calculated for each field size and depth in Solid Water investigated are presented in Table 3.2. The analysis has identified a suggested resolution for the sampling of radiation field profiles to be of the order of 100-200 μm to effectively resolve the complex features of these profiles.

Table 3.2 90% bandwidth measurements and corresponding Nyquist resolutions for various field sizes.

Square Field Size (mm)	Depth 5 cm		Depth 10 cm	
	Bandwidth ₉₀ (cm ⁻¹)	Nyquist Resolution (μm)	Bandwidth ₉₀ (cm ⁻¹)	Nyquist Resolution (μm)
100	35.91	139.23	34.61	144.45
50	36.91	135.48	36.44	137.23
30	37.98	131.65	37.67	132.75
20	38.96	128.34	37.89	131.95
10	39.93	125.21	39.27	127.33
5	40.72	122.78	39.57	126.35

3.3.2 Radiation Hardness Characterisation

Figure 3.3 shows the response of five pixels of the sDMG detector normalised to the response attributed to the pre-irradiation condition of the detector. The normalised response is presented for five independent channels across the array as a function of accumulated dose delivered to the detector. These five pixels were chosen as exhibiting the maximum and minimum deviations in individual response from the mean normalised response of the array for each accumulated dose. The response is measured with the detector operated in passive mode and demonstrates the increase and stabilisation of the charge collection efficiency to within +/-5% for the whole detector array after 40 kGy of delivered dose. The error bars indicate an uncertainty corresponding to two standard deviations in the response of each pixel over three repetitions of the response measurements.

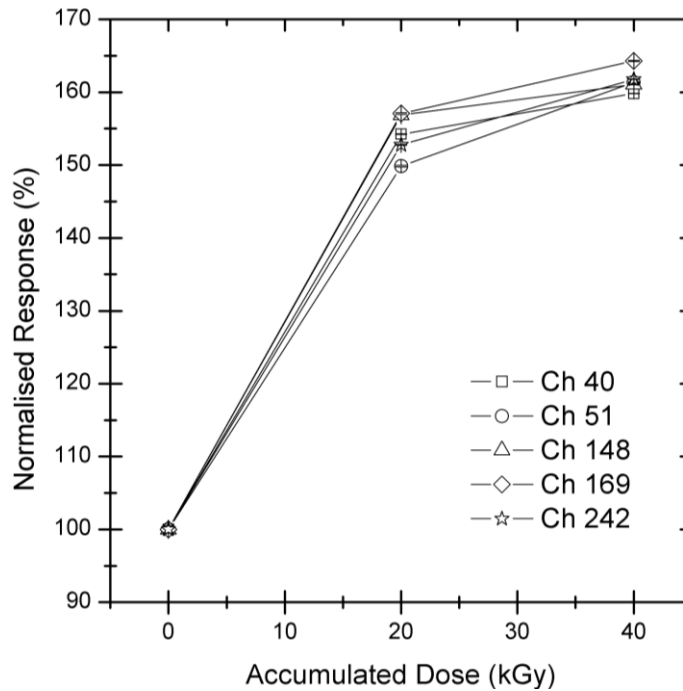


Figure 3.3 Experimental result for the measurement of the response of five pixels normalised to the pre-irradiation condition of the sDMG detector as a function of accumulated dose. Each pixel in the legend is denoted as a ‘Ch’, this is an abbreviation for channel, which relates to the chronological number of the individual pixel in the linear array.

3.3.3 Dose Linearity

Figure 3.4 illustrates the measured dose linearity for the sDMG detector within the dose range of 50 cGy to 500 cGy. The measurements were taken in increments of 50 cGy over the range investigated and the resulting accumulated charge measured within the central channel of the sDMG fitted with a linear function. The conversion factor determined from the linear fitting function is 105 pC/cGy. The error bars indicate an uncertainty corresponding to two standard deviations in the fluctuation of results recorded by the central pixels of the sDMG.

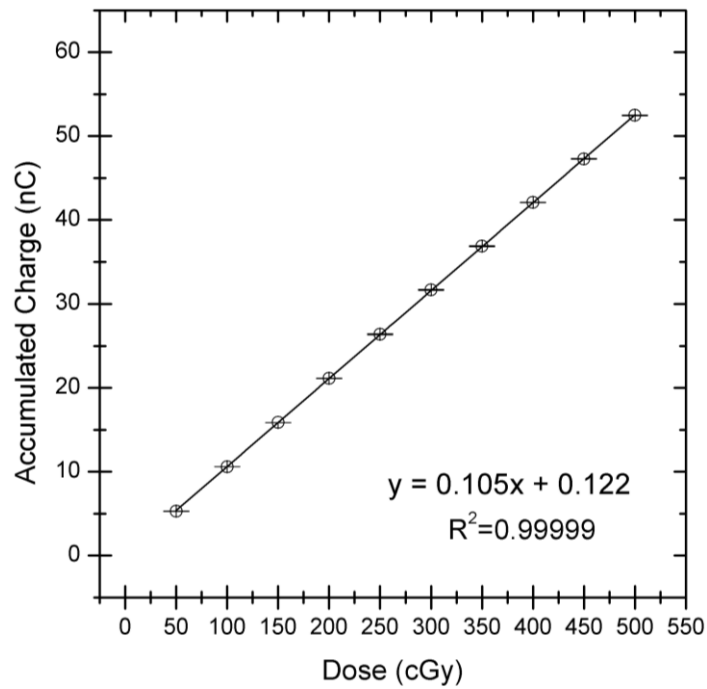


Figure 3.4 The accumulated charge measured within the central channel of the sDMG detector as a function of applied photon radiation dose.

3.3.4 Dose per Pulse Dependence

Figure 3.5 presents the dose per pulse dependence of the sDMG detector. The response of the sDMG is normalised to the response of a CC13 ionisation chamber (IBA dosimetry, Schwarzenbruck, Germany), at a depth of 1.5 cm (d_{max}) in a 10 x 10 cm² 6 MV photon beam. The value of 2.78×10^{-4} Gy/pulse corresponds to the dose per pulse experienced by the CC13 ionisation chamber under these conditions at 100cm SSD.

The results presented in Figure 3.5 illustrate that the sDMG possesses a maximum dose per pulse dependence of approximately -40 % across the range investigated. This significant dependence in the response of the sDMG detector, relative to the CC13 ionisation chamber, must be accounted for utilising correction factors. The methodology undertaken within this portion of the study assumes the response of the CC13 ionisation chamber is independent of the dose rate.

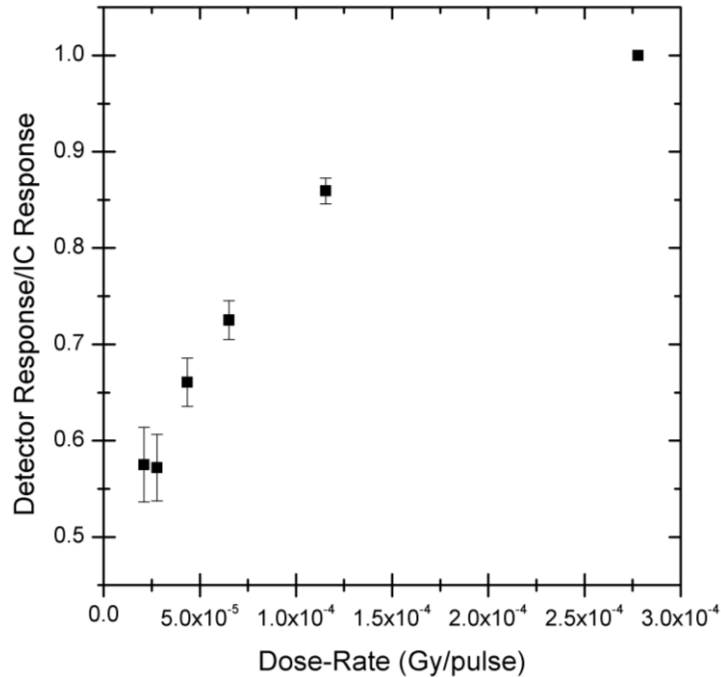


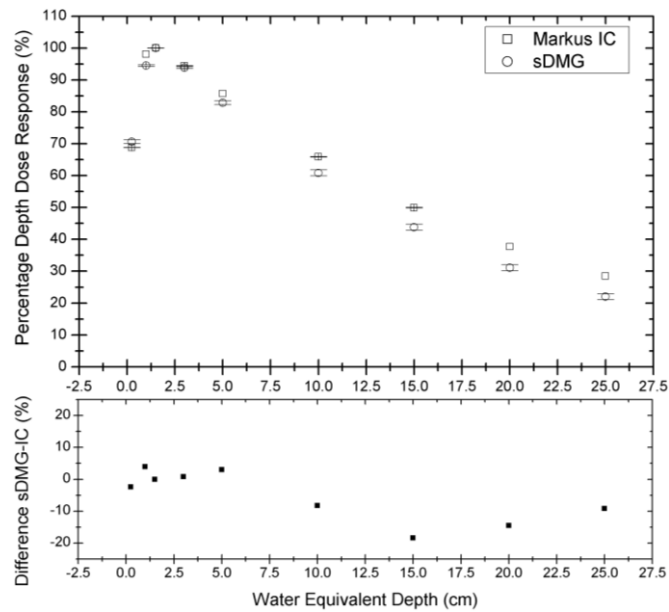
Figure 3.5 The dose per pulse response for the sDMG detector normalized to the estimated dose per pulse delivered at 1.5cm depth in water and 100cm SSD of 2.78×10^{-4} Gy/pulse.

3.3.5 Percentage Depth Dose Measurements

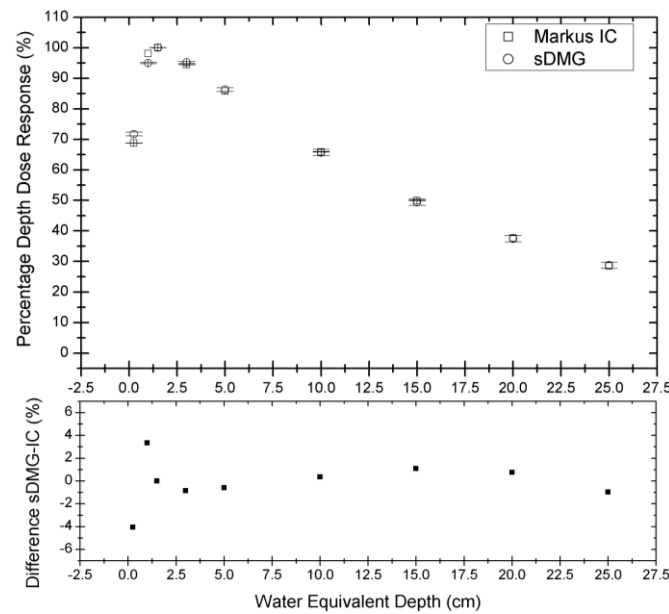
Figure 3.6 illustrates the PDD response of the sDMG detector measured under irradiation by a 6 MV photon beam with field size of $10 \times 10 \text{ cm}^2$ at 100cm SSD, compared to response of a Markus Ionisation chamber under the same conditions. The PDD was investigated within the range of 5 mm to 250 mm depth in Solid Water for both detectors. Figure 3.6(a) shows the sDMG detectors initial PDD behaviour, the exhibited agreement is within +/-8% for depths less than 5 cm in Solid Water, at greater depths the percentage difference between the sDMG and Markus chamber increases to a maximum of 20%.

This discrepancy at depths greater than 5 cm in Solid Water is the result of the intrinsic dose per pulse dependence of the sDMG detector. Following the characterisation of the dose per pulse dependence of the detector, this behaviour is able to be corrected. Correction factors are generated for the range of dose per pulse values experienced by the detector within the experiment by fitting a polynomial to the relationship shown in Figure 3.5. The dose per pulse experienced by the detector at each depth is calculated and the necessary correction factor is determined from the polynomial

equation. The dose per pulse correction factors are in turn applied to the sDMG results at each depth. The result of the application of the calculated correction factors is shown in Figure 3.6(b). The observed maximum difference is reduced from -20% (Figure 3.6(a)) to maintaining an overall agreement of $\pm 1.27\%$ for depths greater than 1.5cm in Solid Water.



(a)

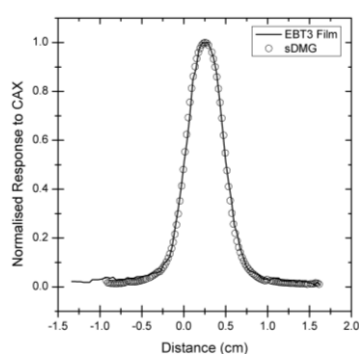


(b)

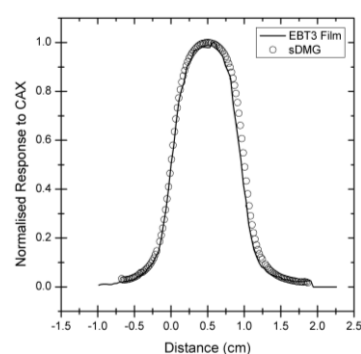
Figure 3.6 PDD response measured with the sDMG detector and Markus ionisation chamber for a 6MV photon beam with $10 \times 10 \text{ cm}^2$ field size at 100cm SSD and percentage difference. (a) Uncorrected PDD response of sDMG detector. (b) PDD response of sDMG detector corrected for intrinsic dose per pulse dependence of sDMG detector.

3.3.6 Beam Profile Measurements

Figure 3.7 presents the results measured from the sDMG detector for 6 MV photon beam field sizes ranging from $0.5 \times 0.5 \text{ cm}^2$ to $5 \times 5 \text{ cm}^2$ at 10cm in Solid Water and 90 cm SSD. The sDMG profiles are compared to those measured under identical conditions using Gafchromic EBT3 film. The sDMG profiles are normalised to the response of the central axis (CAX) pixel within the detector and are aligned to the left hand side spatial coordinate of the 50% response of the CAX pixel value. Profiles measured using the EBT3 film are normalised to the average pixel value within a 1 mm window surrounding the CAX of the film profile. A quantitative analysis of the agreement between the datasets was undertaken using MATLAB (R2013a MathWorks) and the Curve Fitting Toolbox. The individual datasets were fitted with a ‘Piecewise Cubic Hermite Interpolating Polynomial’, the data was interpolated to calculate the spatial coordinates of the 20%, 80% and 50% responses relative to the CAX within each profile. The left-hand side (LHS) penumbral width (20%-80%) and full width at half maximum, FWHM (50%-50%), were determined and compared between the detectors. The average uncertainty calculated across all measurements for the EBT3 film is $\pm 1.9\%$ (Aldosari, 2014) and for the sDMG detector is $\pm 1\%$. The results are summarised, including percentage difference between datasets, in Table 3.3.



(a)



(b)

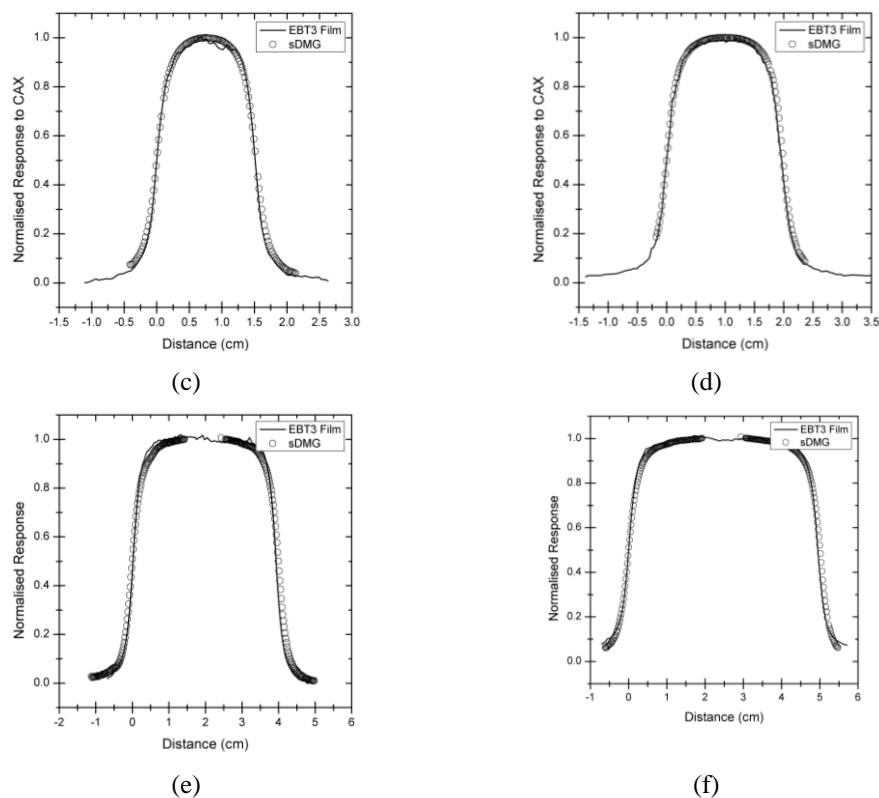


Figure 3.7 sDMG and EBT3 film measured beam profiles for 6MV photon beam at 10cm deep and 90cm SSD for small radiation fields. (a) Field size 0.5 x 0.5 cm². (b) Field size 1 x 1 cm². (c) Field size 1.5 x 1.5 cm². (d) Field size 2 x 2 cm². (e) Field size 4 x 4 cm². (f) Field size 5 x 5 cm².

The sDMG detector demonstrates an agreement with EBT3 film measurements within 0.90% for the determination of the FWHM of the radiation field sizes for all measured beams. The penumbral width exhibits an agreement within at most 60 μm that confirms that the spatial resolution of sDMG of 0.2 mm enables accurate reconstruction of the penumbral region in 6 MV photon fields for sizes below 5 x 5 cm².

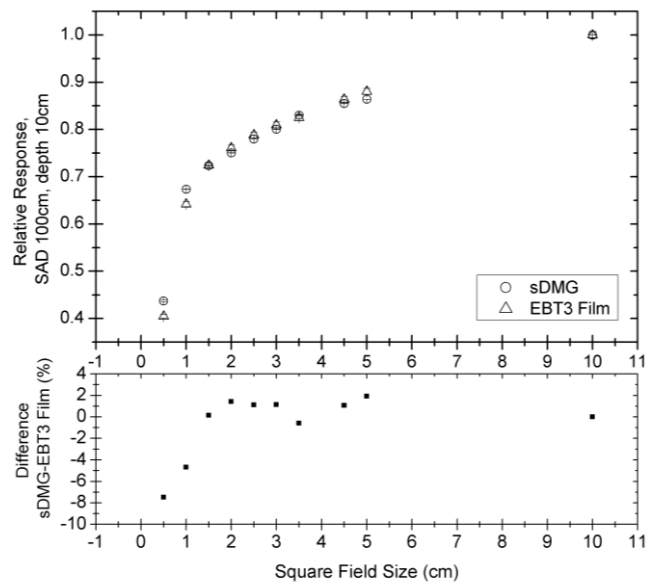
Table 3.3 sDMG and EBT3 film measurement FWHM and penumbral width (20%-80%) comparison for different small field sizes.

Square Field size (mm)	sDMG		EBT3		Difference (sDMG-EBT3)	
	FWHM (mm) $\pm 0.01\text{mm}$	Penumbra, LHS (mm) $\pm 0.01\text{mm}$	FWHM (mm) $\pm 0.1\text{mm}$	Penumbra, LHS (mm) $\pm 0.1\text{mm}$	ΔFWHM (μm)	$\Delta\text{Penumbra}$ (μm)

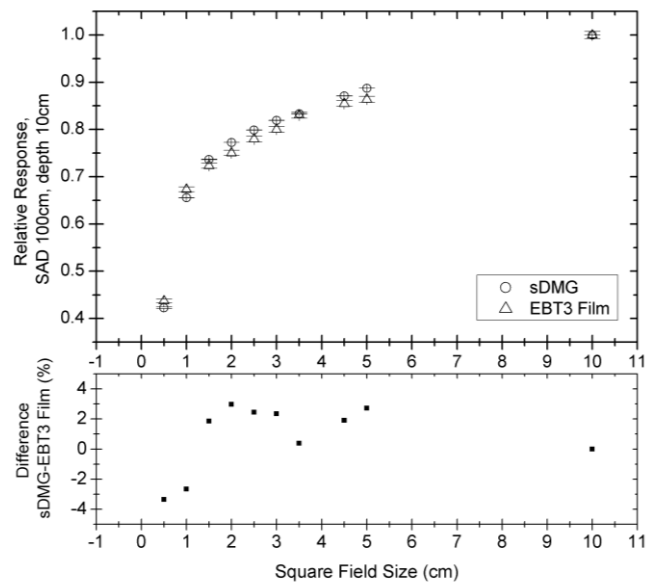
5	5.04	2.11	5.0	2.1	40	10
10	10.03	2.62	10.0	2.6	30	20
15	15.14	2.71	15.1	2.7	40	10
20	19.92	2.88	20.0	2.9	-80	-20
30	29.84	3.46	29.9	3.4	-60	60
40	40.00	3.85	39.8	3.8	160	50
50	50.12	3.75	49.7	3.7	450	50

3.3.7 Output Factor Measurements

Figure 3.8 illustrates the results of the experimental measurement of output factor utilising the sDMG detector and EBT3 film. The response of the pixels closest to the CAX of each field for sDMG and the pixel region surrounding the CAX for the EBT3 film for each field size is normalised to the response under irradiation by a 10 x 10 cm² field size. The results are investigated as a function of radiation field size, delivered at a depth of 10 cm at isocentre for a 6 MV photon beam. Figure 3.8(a) presents the uncorrected output factor results acquired with the sDMG. Based on the calculated output factor result of the EBT3 film for each field size investigated a dose per pulse correction factor is calculated and applied, as in 3.3.5, to the sDMG results for each field size, Figure 3.8(b). The sDMG is shown to under-respond relative to the EBT3 film for field sizes smaller than 1.5 x 1.5 cm² up to a maximum of 3.1% for the field size of 0.5 x 0.5 cm². For radiation field sizes greater than 1.5 x 1.5 cm² the sDMG detector is observed to over-respond relative to EBT3 film with the agreement remaining within 2%.



(a)



(b)

Figure 3.8. Response of sDMG detector and EBT3 film to varying field size of a 6 MV photon beam normalised to response of detector to 10 x 10cm² field size. Percentage difference between sDMG and EBT3 film presented as a function of radiation field size. (a) Uncorrected OF response of sDMG detector. (b) OF response of sDMG detector corrected for intrinsic dose per pulse dependence.

3.4 Discussion

The results of Table 3.2 identify a series of recommended sampling resolutions to accurately

reconstruct 90% of the features present in the radiation field penumbra for different field sizes and depths in Solid Water. The penumbral width of a radiation field decreases for smaller field sizes and shallower depths in phantom material, as shown in Table 3.1. It is evident from Table 3.2 that as the field size decreases the Nyquist resolution decreases, identifying a need for higher resolution sampling to resolve the sharper features of smaller field sizes. Also, as depth in phantom material decreases the penumbral width is shown to decrease, thus, penumbral features become sharper closer to the material surface.

The Serial Dose Magnifying Glass (sDMG), Figure 2.13, is a multi-strip silicon detector comprised of two linear arrays of 128 diodes with pitch 200 μm . The response of the detector operated in passive mode was measured under irradiation by a Co-60 gamma emission source. The radiation damage study illustrates the detectors response increase and stabilisation of the charge collection efficiency across the detector to within +/-5% for the array after 40 kGy of delivered dose. sDMG shows a variation of the response versus accumulated dose opposite to the expected trend from a silicon diode array. This behaviour has been extensively investigated and an explanation provided by means of Technology CAD simulations in Aldosari et al. (Aldosari, 2013) where a pad detector fabricated by the same p-type substrate manufacturing technology has been characterised. Additionally, it has been demonstrated previously that the charge collection efficiency of this detector technology remains stable up to 120 kGy of lifetime accumulated dose (Aldosari, 2013), assuming a conservative delivery of 200 Gy per week for quality assurance of stereotactic treatments, this would result in a minimum lifetime of approximately 7.7 years.

Normalised beam profile measurements were conducted for field sizes between 0.5 x 0.5 cm^2 and 4 x 4 cm^2 and compared between the sDMG and EBT3 film. The sDMG detector exhibited agreement to within 0.90 % for the determination of the FWHM of the radiation field sizes when compared with EBT3 film measurements. The disagreement in penumbral width measurements between sDMG and EBT3 film was found to be at most 60 μm difference for static 6 MV photon beam delivery. This disagreement between the detectors is restricted to the submillimeter scale and is at most 0.45 mm in the case of FWHM comparison. From Figure 3.1 and Table 3.1 it is evident that the penumbral gradient is similar for all field sizes when the beam profile is presented as an absolute dose distribution. As the penumbra is mostly determined by the scattering power of photons i.e.

their energy spectra and therefore should not be dependent on the field size. Based on this it is clear that the sDMG is applicable for penumbra measurements for field sizes both smaller and larger than $5 \times 5 \text{ cm}^2$, up to $10 \times 10 \text{ cm}^2$. These results confirm the requirement estimated by the discrete Fourier transform method for the minimum spatial resolution (Table 3.2) required for a pixelated detector to reconstruct dose measured by the EBT3 film.

Extensive characterisation of the DUO detector for 6 MV photons was conducted by Al Shukaili et al. (Al Shukaili, 2017). This characterisation followed the methodology outlined in this work and included investigation into dependence and response of DUO for dose rate (dose per pulse), PDD, beam profiles and output factors. The dose per pulse corrected PDD was demonstrated to agree within 1.5% of a Markus ionisation chamber for depths up to 25 cm in Solid Water. FWHM agreement was found to be within 1% and within 0.5 mm for penumbral width (20%-80%) measurements. These results compare favourably to the sDMG with similar beam profile accuracy and magnitude of dose per pulse corrected PDD agreement.

3.5 Conclusion

The Discrete Fourier Transform was used to generate Fourier spectrums for the 3-97% penumbral regions of response normalised, high spatial resolution radiochromic EBT3 film beam profiles of radiation fields with field sizes ranging from $0.5 \times 0.5 \text{ cm}^2$ up to $10 \times 10 \text{ cm}^2$. The bandwidth of the Fourier amplitude spectrum was defined to be the frequency band containing 90% of the total area under the curve. The Nyquist-Shannon sampling theorem was applied to the bandwidth measurements to calculate a recommended sampling spatial resolution for the field sizes investigated of the order of 130 - 200 μm .

The sDMG exhibits a maximum dose per pulse dependence of approximately 40% across the range of $2.1 \times 10^{-5} \text{ Gy pulse}^{-1}$ to $2.78 \times 10^{-4} \text{ Gy pulse}^{-1}$ investigated. The response of the detector was normalised to the response of the CC13 ionisation chamber irradiated under identical conditions. The results were used to generate a series of correction factors to account for the dose per pulse dependence within the sDMG detector. Based on the obtained results a recommendation is made to fabricate new generations of DMG on low resistivity bulk Si and later on epitaxial p-Si to improve

DPP dependence while providing the same spatial resolution.

PDD measurements for the sDMG were compared to a Markus ionisation chamber over the range 0.5 cm to 25 cm depth in Solid Water. Initially the exhibited agreement between the Markus IC and sDMG is within +/-8% for depths less than 5 cm in Solid Water, at greater depths the percentage difference between the sDMG and Markus chamber increases to a maximum of 20%. The discrepancy between the response of sDMG and the Markus IC is attributed to the intrinsic dose per pulse dependence of the sDMG. Utilising the calculated correction factors the observed maximum difference is reduced from $\pm 20\%$ to $\pm 4\%$ with the sDMG response maintaining agreement within $\pm 1.27\%$ for depths greater than 1.5cm in Solid Water.

The output factor for the sDMG was measured and compared to EBT3 film for field sizes ranging from $0.5 \times 0.5 \text{ cm}^2$ up to $10 \times 10 \text{ cm}^2$. For field sizes less than $1.5 \times 1.5 \text{ cm}^2$ the sDMG is observed to under-respond up to a maximum of 3.3% for the field size of $0.5 \times 0.5 \text{ cm}^2$ relative to EBT3 film. For field sizes greater than $1.5 \times 1.5 \text{ cm}^2$ the sDMG detector is observed to over-respond relative to EBT3 film with the agreement remaining within $\pm 2\%$. The disagreement between the EBT3 film and sDMG without dose rate dependence correction is within 8%, with dose rate dependence correction agreement is within 3.1%.

Dose linearity, dose per pulse dependence, PDD, beam profile and output factor measurements were conducted for the sDMG detector on a 6 MV linac. The results of these measurements demonstrate the applicability of the sDMG detector for use as an accurate tool for commissioning and QA of small area radiation fields.

Chapter 4

Quality Assurance of stereotactic radiotherapy combined with electromagnetic MLC tracking using silicon detectors

4.1 Introduction

The treatment of small volume tumours within the lungs requires small conformal radiation beams and real time motion adaptation to improve treatment efficiency and reduce normal tissue toxicity. MLC tracking has been applied clinically to lung SABR treatments, providing reduced target volumes whilst delivering the planned target dose in the presence of respiratory motion (Booth, 2016). The combination of small field dosimetry, target motion and heterogeneous scattering conditions is challenging for accurate dose measurement in real-time and necessitates a specialised tool for quality assurance (QA) and treatment verification.

This chapter investigates the effects of homogenous and heterogeneous scattering conditions upon the delivered dose distribution in the treatment of dynamic targets using small radiation fields and aims to evaluate the performance of the sDMG and DUO detectors with AFE readouts compared to the gold standard of high spatial resolution two-dimensional dosimetry, EBT3 film.

4.2 Materials and Methods

4.2.1 DUO and sDMG

DUO and sDMG are both pre-irradiated to stabilize the response of the detectors, DUO is pre-irradiated to 120 kGy (Al Shukaili, 2017) and sDMG is pre-irradiated to 40 kGy for uniform stabilisation of CCE across the array, as per results of 3.3.2. A uniformity equalization is applied prior to irradiation to correct the response of each pixel for intrinsic sensitivities and gain variations attributed to the individual preamplifier channels. The correction factor is generated under stimulation from a 20 x 20 cm² 6MV photon beam from a linac equipped with a flattening filter at 10 cm depth in Solid Water and 100cm SSD. In comparison to a 20 x 20 cm² radiation field the DUO is 5.2 x 5.2 cm² and the sDMG is 0.2 x 5.08 cm² with each detector aligned to the central axis of the radiation beam. The profile of the beam across the detectors at this depth is considered flat, with a clinically stated flatness (IEC 60976) measure in this region of 100.3, thus the stimulation of each pixel is assumed to be uniform. An array of correction factors is generated based upon the individual response of the pixels and the combined average response (Aldosari, 2014).

4.2.1.1 Dosimetric Validation

The results of profiling on a 6 MV linac photon beam in Solid Water using DUO has been investigated and reported previously (Al Shukaili, 2017). To ensure the dosimetric accuracy of the DUO detector is valid for a low-density medium, the detector was encapsulated within the homogenous timber phantom (Figure 4.1 (b)) and irradiated with the planned 3DCRT treatment. The irradiation was repeated with EBT3 Film within the homogeneous timber phantom and the results of the axial beam profiles from the two detectors compared.

4.2.2 Phantom Scattering Conditions

The DUO detector was encapsulated in three different phantoms to simulate various scattering conditions. Figure 4.1 illustrates the materials of the various phantoms in cross-section, with silicon representing the detector. The first scattering condition, Figure 4.1(a), consists of homogenous Solid Water (GAMMEX, WI, USA) surrounding the detector, the second scattering condition is composed of homogenous timber as an analogue for lung material with a density of approximately

0.4 g/cm³, Figure 4.1(b). Figure 4.1(c) represents the phantom designed to mimic the heterogeneous conditions of a tumour within the lung, consisting of a Solid Water spherical target with diameter of 1 cm within timber.

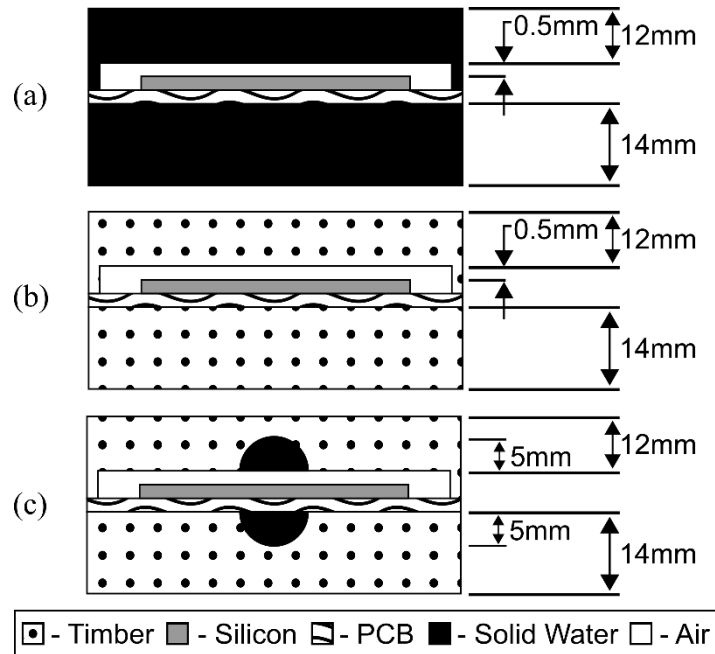


Figure 4.1 Cross-sections illustrating the material composition of the three scattering conditions investigated and dimension of air gap. (a) Homogenous Solid Water phantom. (b) Homogenous timber phantom. (c) Heterogeneous timber phantom with Solid Water target.

4.2.3 Film Dosimetry

Gafchromic EBT3 film (Ashland Inc., Wayne, NJ, USA) was used as the benchmark for the profile measurements due to its high spatial resolution, dosimetric accuracy (Sorriaux, 2013) and energy independence in the MV photon energy range (Borca, 2013). EBT3 film is a self-developing dosimetry film offering symmetrical layer configuration. A single active radiochromic layer of 30 μ m nominal thickness is laminated between two transparent polyester layers of 125 μ m nominal thickness (Huet, 2014).

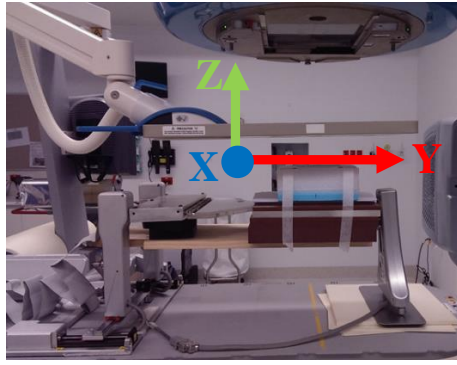
The EBT3 film was scanned before and 72 hours after irradiation, maintaining identical orientation in transmission mode using a MicroTek scanner without image corrections. Six scans were taken of each film piece in 48-bit RGB colour mode with a resolution of 72 dpi. The images were saved in

the .TIFF file format and were analysed and converted to optical density (OD) using ImageJ 1.47v. A second-order polynomial was generated from an associated calibration curve acquired from the same film batch. Using a net optical density protocol, the red colour channel information was converted from pixel value to OD to dose (Butson, 2006). Line profiles along the central axis of the EBT3 film pieces were examined for comparison to profiles acquired with DUO.

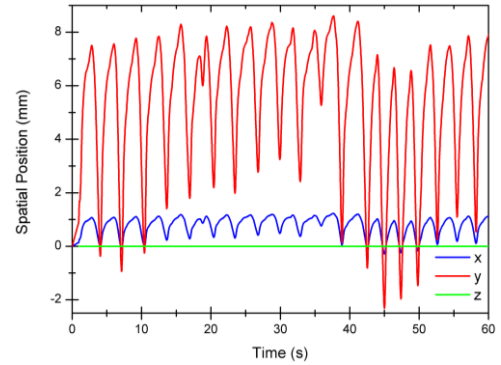
4.2.4 Dynamic treatment plan delivery

4.2.4.1 sDMG linear detector array

The sDMG detector was placed upon a HexaMotion 6D Motion platform manufactured by Scandidos (Sweden). The HexaMotion platform is capable of replication of motion along 6 axis of freedom and is designed as accessory for the Delta⁴ dosimetry phantom. The prototype of HexaMotion adopted in this work has been adapted for use with other detectors and dosimetry systems via the addition of a rigid timber platform between the pedestals. The detectors are positioned upon the timber platform above 6 cm of Solid Water backscattering, at a depth of 1.5cm in Solid Water (water equivalent depth) and 100 cm source to axis distance (SAD) (isocentre). The Calypso motion tracking array is placed above the system, consisting of a panel composed of a series of coils able to detect the electromagnetic signal from a set of three inductors (transponder beacons) positioned above the detector upon HexaMotion. The position of the Calypso EM tracking panel is registered by three infrared cameras to the room coordinate reference system (Shah, 2011) and the tracking information recorded by Calypso drives the algorithms which modify the position of the MLC leaves to compensate for motion of the target (Keall, 2014). Within this investigation the motion of the detector is limited to the 'x' and 'y' directions only. Figure 4.2(a) illustrates the direction of the spatial vectors relative to the physical experimental setup, Figure 4.2(b) shows the quantitative magnitudes of the spatial displacement expected along both spatial axis as a function of time. The temporal pattern shown in Figure 4.2(b) is indicative of real patient lung motion, the coordinates are supplied to the HexaMotion via a formatted text file as absolute 'x' and 'y' spatial displacements from the origin within the coordinate system of HexaMotion, every 20ms.



(a)



(b)

Figure 4.2 (a) The sDMG detector positioned upon the HexaMotion platform above 6cm of Solid Water for backscatter and beneath 1.5cm of Solid Water. The Calypso motion tracking array is suspended above the detector, beneath the linac head, with the transponders suspended upon a foam insert above the detector to enable tracking. (b) The temporal pattern supplied to the HexaMotion phantom to mimic the motion of a lung in x and y direction during irradiation of the detector, x direction is into the image.

Square MLC fields of sizes $1 \times 1 \text{cm}^2$ and $3 \times 3 \text{cm}^2$ are delivered from gantry angle of 0 degrees, to both the sDMG detector and Gafchromic EBT3 film independently within the experimental setup. The sDMG is first aligned along the 'y' direction of motion (Figure 4.2(a)), acquiring a complete data set and then rotated 90 degrees to be aligned along the 'x' direction to repeat acquisition of the dataset. The jaws within the linac head are retracted a further 1 cm in each direction from the MLC leaf end positions to minimise leaf-leakage out of field, without restricting the complete range of motion necessary for the MLC leaves. From Figure 4.2(b) the maximum displacement is +8mm in the 'y' direction and +2 mm in the 'x' direction for this temporal pattern.

The silicon detector, sDMG and the EBT3 film are irradiated with 1000 MU at 600 MUmin^{-1} with a 6MV photon beam for three cases; static platform (HexaMotion), dynamic platform without motion tracking and dynamic platform with motion tracking (MLC tracking enabled). Under the static platform conditions, the detector is positioned upon the platform, which remains stationary throughout the treatment time. The first dynamic case consists of the HexaMotion platform providing the temporal lung motion during the treatment time without motion tracking engaged. Lastly, the HexaMotion provides the dynamic lung motion during the treatment delivery while the Calypso system tracks the motion of the RF transponder beacons, relaying this information to the

MLC to compensate for this motion by re-positioning the beam aperture.

4.2.4.2 DUO monolithic detector array

The detector was irradiated using a 6MV Varian 21EX linac (Varian Medical Systems, Palo Alto, USA) photon beam to assess the performance of the detector and investigate the impact of motion and scattering conditions upon the delivered dose distribution. DUO placed in each of the phantoms (Figure 4.1) was placed upon the HexaMotion 6D motion platform. The HexaMotion platform is capable of replicating motion with 5 degrees of freedom.

The detector and HexaMotion platform were positioned at 100 cm source to axis distance (SAD) with the gantry at 0 degrees throughout delivery. A series of spatial coordinates in the form of absolute displacements from origin in the 'X' (Left-Right) and 'Y' (Superior-Inferior, 'Sup-Inf') directions are supplied to the platform. The platform drives to the coordinates in series, altering the position of the detector throughout treatment. The motion pattern supplied is a real patient's lung motion (Figure 4.2(a)) restricted to two-dimensional motion in the 'X' and 'Y' axis only, Figure 4.2 (b).

A planning CT was acquired with the detector encapsulated in the heterogeneous phantom (Figure 4.1(c)), positioned upon HexaMotion. From this image dataset, the Solid Water target was delineated as Gross Tumour Volume (GTV) and a +5 mm margin was applied to the GTV to form the Planning Target Volume (PTV). A 3-D Conformal Radiotherapy (3DCRT) plan and an Intensity Modulated Radiotherapy (IMRT) were generated with the Eclipse treatment planning system to deliver a mean dose of 500 cGy to the PTV for the 3DCRT plan and 540 cGy to the PTV for the IMRT plan. The 3DCRT plan consisted of a single beam conforming to the PTV using the MLC. The IMRT plan consisted of a single beam with MLC leaves beginning in a closed position and sweeping across the field while conforming to the shape of the PTV. The plans were exported to the linac and delivered to the detector for all experimental configurations (i.e. motion and scattering conditions).

4.2.4.3 Scattering conditions

For dynamic treatment plan delivery to DUO in each scattering condition, the Calypso panel (Varian

Medical Systems, Palo Alto, USA) was positioned above the moving platform. The location of the panel within the room coordinate system is determined by three fixed infrared cameras (Shah, 2011). The position of transponder beacons placed on the platform is recorded. The spatial localization information provided by Calypso is used to modify the position of the MLC aperture (Keall, 2014). The linac collimator is rotated such that the driven direction of the leaves is aligned with the Sup-Inf direction ('Y' direction, Figure 4.2(b)). A predictive algorithm is applied during MLC tracking to extrapolate the trends in the targets motion and predict the necessary position of the MLC aperture to mitigate motion effects and account for the expected time delay between motion detection and MLC re-positioning (Ruan, 2010).

The generated 3DCRT and IMRT plans are delivered for a series of motion cases: (i) 'no motion' (NM) which represents the ideal case where the platform remains stationary at its home position throughout delivery, (ii) 'motion' (M) where the platform is provided with the motion and moves during delivery with the MLC remaining static and not adapting, (iii) 'motion+tracking' (MT), the platform moves and the MLC tracking system is engaged to track and compensate for identified motion by adapting the MLC during delivery. The three motion management schemes were repeated for each of the three phantom scattering conditions.

4.3 Results

4.3.1 DUO Dosimetric Validation

The axial profiles for each motion case are aligned at 50% on the left-hand side penumbra. The 50% response coordinate is determined relative to the response of the pixel positioned along the central axis (CAX) of the beam. The charge to dose conversion factor for the DUO is (56.34 ± 0.04) pC/cGy/pixel. The conversion factor is used to transform the response of the detector from charge in pC to dose in cGy. Figure 4.3 demonstrates the direct comparison of the dose profiles measured by DUO to the dose profiles measured using EBT3 Gafchromic film.

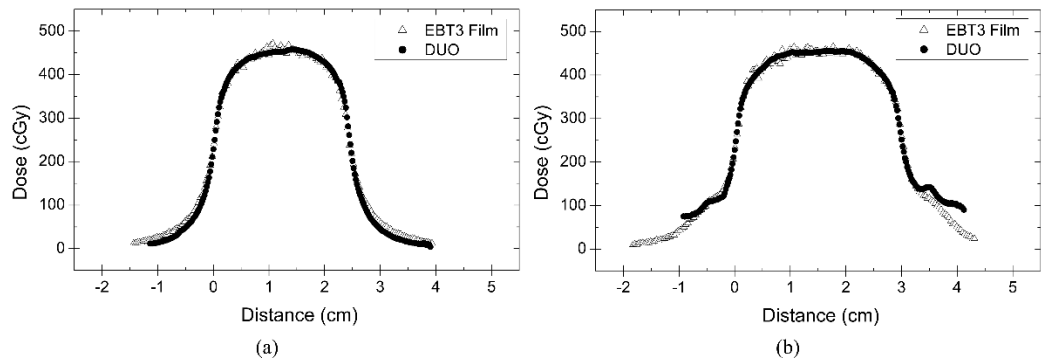


Figure 4.3 Comparison of EBT3 film and DUO beam profiles for 6 MV linac in homogenous timber phantom. (a) Superior-Inferior direction. (b) Left-Right direction.

Table 4.1 summarises the measurements of Full-Width at Half Maximum (FWHM) and left-hand side (LHS) penumbral width (PW) between the 20% and 80% response values for the EBT3 film and DUO.

Table 4.1 Comparison of Full-width at Half Maximum (FWHM) and Penumbral Width (PW) measurements for EBT3 Film and DUO in Superior-Inferior (Sup-Inf) and Left-Right directions.

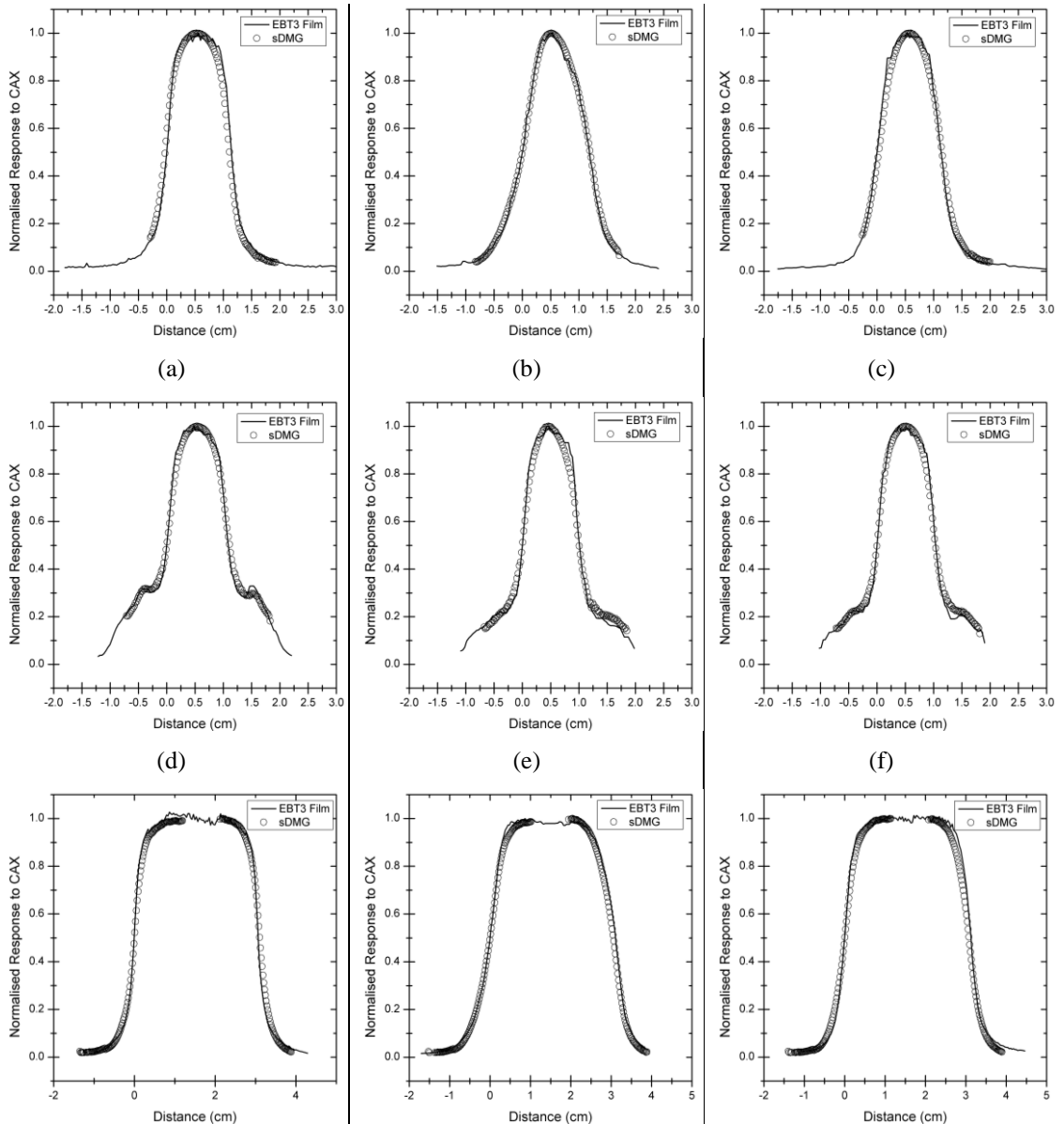
Profile Direction	DUO		EBT3 Film		Difference (DUO-EBT3)	
	FWHM (mm) ± 0.02 mm	PW, LHS (mm) ± 0.02 mm	FWHM (mm) ± 0.1 mm	PW, LHS (mm) ± 0.1 mm	Δ FWHM (mm)	Δ PW (mm)
Sup-Inf	2.48	0.44	2.46	0.51	0.012	-0.065
Left-Right	3.04	0.80	3.05	0.77	-0.015	0.030

4.3.2 Dynamic treatment plan delivery with varying scattering conditions

4.3.2.1 sDMG linear detector array

The diagrams in Figure 4.4 present a sample of the measurements of beam profiles along the 'y' and 'x' direction for the irradiation of the sDMG and EBT3 film by square MLC-defined fields under static and dynamic platform conditions. The one-dimensional beam profiles reconstructed from the sDMG detector are compared with profiles extracted under identical conditions from the

Gafchromic EBT3 film measurements. The beam profiles presented include those of 1 x 1 cm² in the 'y' and 'x' directions and 3 x 3 cm² in the 'y' direction. For the irradiation of the sDMG by the 3 x 3 cm² field size, the beam is centred on the physical gap between the sequential linear arrays. The radiation beam profile is reconstructed based on the accurately known distance separating the ends of the two linear arrays. The response of each channel within the sDMG detector is normalised to the response of the central axis (CAX) pixel within the profile. The EBT3 film response is normalised to the response of the pixels occupying a 1 mm window surrounding the CAX of the beam profile. The beam profiles acquired from both detectors are aligned such that origin lies at the coordinate corresponding to 50% response of the CAX beam profile pixel for sDMG and CAX beam axis pixels for the EBT3 film.



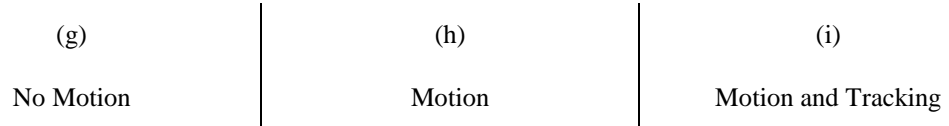


Figure 4.4 6 MV Photon beam profiles measured with sDMG detector and EBT3 film at 1.5 cm deep and 100 cm SAD (isocentre) for characterisation of high resolution dynamic quality assurance capabilities with different field sizes. (a) No motion, 1 x 1 cm², along y-direction. (b) Motion, 1 x 1cm², along y-direction. (c) Motion and Tracking, 1 x 1 cm², along y-direction. (d) No motion, 1 x 1 cm², along x-direction. (e) Motion, 1 x 1 cm², along x-direction. (f) Motion and Tracking, 1 x 1cm², along x-direction. (g) No motion, 3 x 3 cm², along y-direction. (h) Motion, 3 x 3 cm², along y-direction. (i) Motion and Tracking, 3 x 3 cm², along y-direction.

An investigation was conducted to evaluate the quantitative agreement between the EBT3 film and sDMG datasets using MATLAB (R2013a MathWorks) as in 3.2.6. The right-hand side (RHS) PW (20%-80%) and FWHM (50%-50%) were calculated and compared between the detectors. The average uncertainty across all measurements with the sDMG detector is $\pm 1.5\%$, induced by the RF generated by Calypso, which effects the SNR of the DAQ system. The results are summarised, including the associated percentage difference between the datasets, in Table 4.2.

Table 4.2 sDMG and EBT3 film measurement FWHM and penumbral width (20%-80%) comparison for cases without motion, with motion and with motion and tracking enabled.

Field size (mm)	Case	sDMG		EBT3		Percentage Difference (sDMG-EBT3)	
		FWHM (mm) $\pm 0.01\text{mm}$	Penumbra, RHS (mm) $\pm 0.01\text{mm}$	FWHM (mm) $\pm 0.1\text{mm}$	Penumbra, RHS (mm) $\pm 0.1\text{mm}$	ΔFWHM (%)	$\Delta\text{Penumbra}$ (%)
10	<i>No Motion</i>	11.39	2.94	11.4	2.6	-0.09	11.56
	<i>Motion</i>	11.99	4.94	11.9	4.6	0.75	6.88
	<i>Motion&Tracking</i>	11.20	3.98	11.1	3.4	0.90	14.57
30	<i>No Motion</i>	31.00	3.67	30.6	3.1	1.3	15.53
	<i>Motion</i>	30.53	5.43	31.0	5.4	-1.54	0.55
	<i>Motion&Tracking</i>	30.75	4.77	31.0	4.3	-0.81	9.85

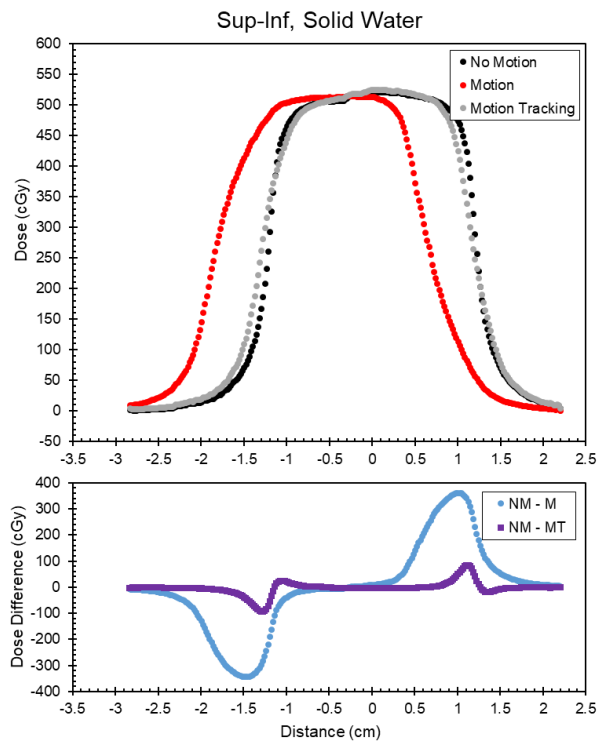
The motion supplied to the HexaMotion platform, experienced by the detectors, demonstrates a clear baseline shift along the 'y' axis of motion, Figure 3.1(b). This baseline shift is approximately +4 mm in magnitude from the platform origin and effectively distorts the dose profile along the 'y' axis in the positive 'y' direction.

Table 4.2 summarises the quantitative analysis of the independent detectors datasets and highlights the agreement between the devices. The agreement observed between the measurements of FWHM of the static and dynamic radiation field sizes was within 1.73 %. The most significant disagreement between the detectors was observed in the penumbral width measurements with a maximum spatial difference of 0.82 mm for the 3x3cm² static radiation field. Both datasets from the independent detectors confirm the effectiveness of MLC tracking to reduce the impact of dose smearing attributed to the supplied lung motion.

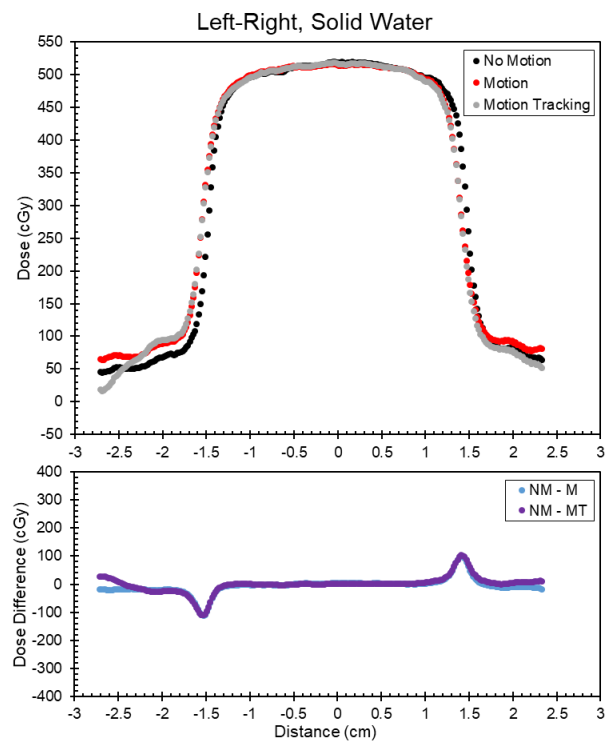
Figure 4.4 (d), (e) and (f) present the results of measurements taken along the 'x' direction of motion, evident in Figure 4.2(a). The 'x' motion supplied to the motion platform possesses an absolute spatial displacement in the 'x' direction of maximum 2 mm. This limits the effective distortion occurring to the reconstructed profile along this direction of motion. The beam profiles are still distorted by the 'y' component which is evident in Figure 4.4(e) and partially compensated in Figure 4.4(f). The distal penumbral regions of the profiles illustrate the effect of MLC inter-leaf leakage, radiation escapes along the edges of the MLC leaves until the retracted jaws shield the out of field regions.

4.3.2.2 DUO monolithic detector array

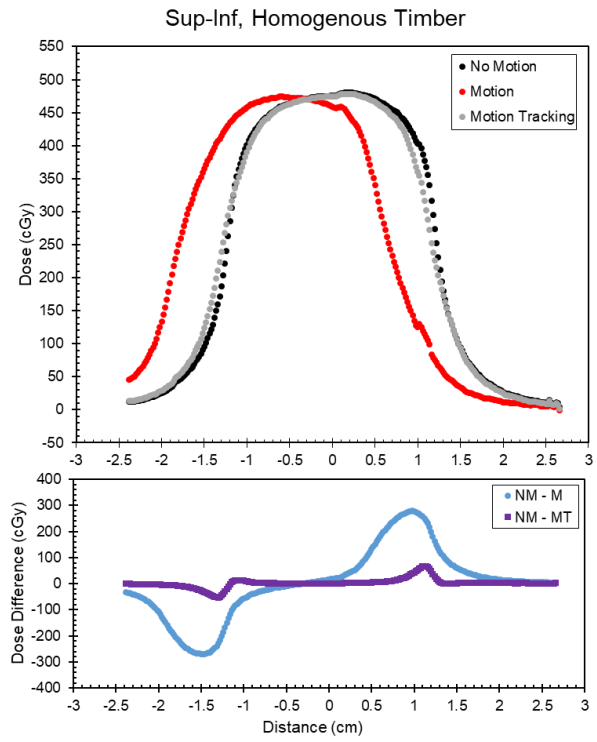
Axial profiles of a 6MV linac photon beam for the three separate motion cases with three different scattering conditions and two different treatment modalities were acquired, Figure 4.5 and Figure 4.6. The three motion cases are compared for each of the scattering conditions investigated. The average uncertainty calculated for the DUO is $\pm 1.5\%$, induced by fluctuations in the response baseline by the radiofrequency field generated by Calypso. The measured profiles of the dose distributions in the Left-Right and Sup-Inf directions are compared using a point-to-point validation to assess the similarity of the profiles to the 'no motion' case. Figure 4.5 illustrates the results and direct comparison of the three motion cases for each scattering condition with a 3DCRT delivery.



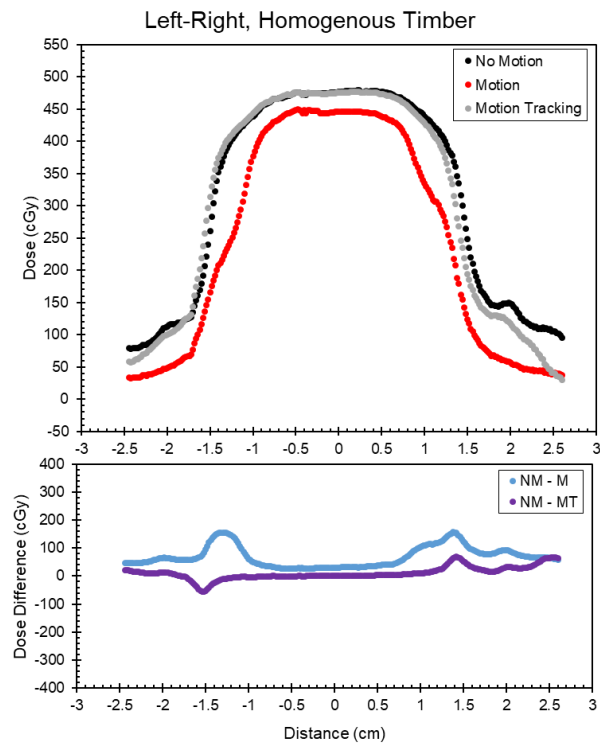
(a)



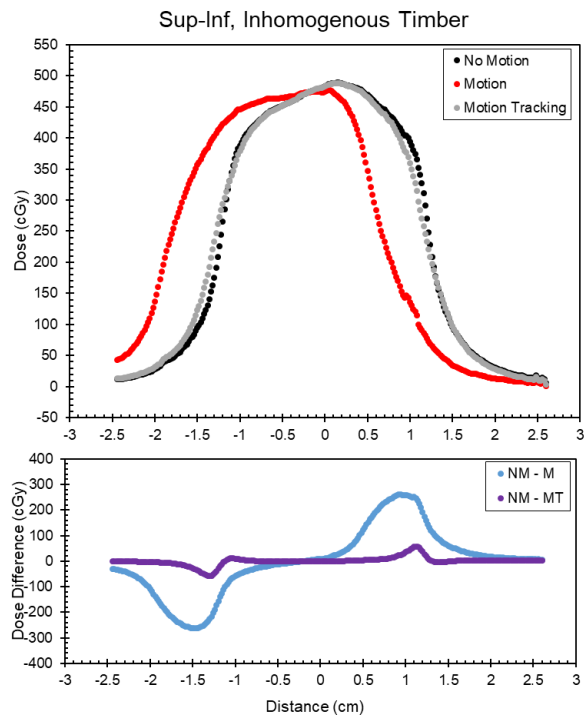
(b)



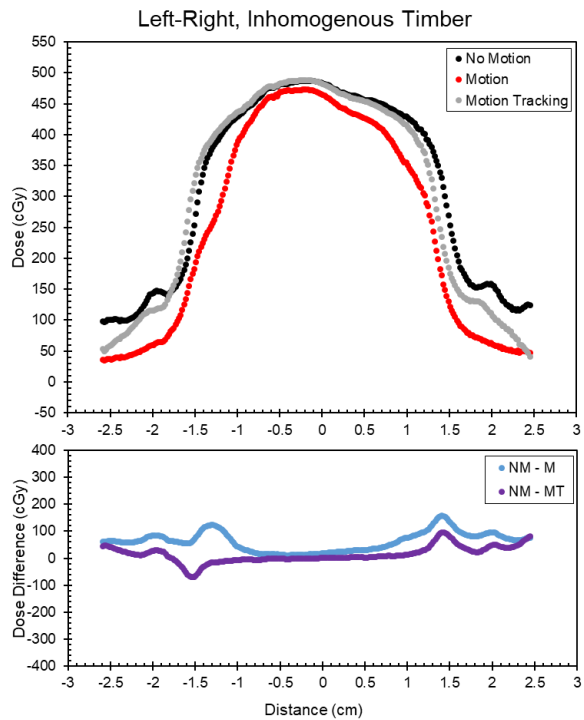
(c)



(d)



(e)



(f)

Figure 4.5 3DCRT 6MV linac beam profiles for the three different scattering conditions and three different motion cases (No Motion, Motion and Motion+Tracking) using DUO and the corresponding point-to-point profile comparison. (a) Sup-Inf direction with homogenous Solid Water phantom. (b) Left-Right direction with homogenous Solid Water phantom. (c) Sup-Inf

direction with homogenous timber phantom. (d) Left-Right direction with homogenous timber phantom. (e) Sup-Inf direction with heterogeneous timber and Solid Water target phantom. (f) Left-Right direction with heterogeneous timber and Solid Water target phantom.

Figure 4.5(a) illustrates the beam profile comparison in the Sup-Inf direction for the homogenous Solid Water phantom. The impact of the applied motion during treatment is evident because the central axis of the beam is displaced 0.5 cm and the penumbrae are smeared out with a difference between the ‘no motion’ and ‘motion’ profiles in the penumbral region at most 340 cGy (approximately 80%). The deformation or skewing of the profile is attributed to the slow periodicity of the applied motion pattern. The impact of motion produces a systematic under and overdosing outside the intended target volume. Implementation of MLC tracking returns the features of the delivered dose distribution to the ‘no motion’ case, with only small discrepancies in the penumbral regions at most 85 cGy (approximately 15%). The activation of the predictive algorithm with MLC tracking results in additional improvements within the penumbral region with the discrepancy reduced to at most 80 cGy difference. Figure 4.5(b) presents the results of the axial profiles in Solid Water for the Left-Right direction which is perpendicular to the direction of MLC leaf travel and shows the interleaf leakage out of field. The impact of the applied motion in this direction is minimal because the motion has a dynamic magnitude of approximately ± 0.5 mm (X axis in Figure 4.2(a)) and results in minor differences between the profiles.

Figure 4.5(c) and (d) show the axial beam profiles for the homogenous timber phantom. These profiles exhibit similar features to the Solid Water case. Relative to the homogenous Solid Water phantom the beam profiles within the lower density homogenous timber phantom show a less flat in-field dose deposition with broader penumbrae, as expected due to the larger lateral scattering range of the electrons [22]. Despite the broadening effect of the low-density material, the application of motion has a significant impact upon the total dose delivered in the Left-Right direction as shown in Figure 4.5 (d). The motion in the Sup-Inf direction displaces the beam from the central axis of the detector and the Left-Right profile measures across the beam penumbra where the field has narrowed leading to under-dosing of at most 150 cGy (Figure 4.5(d)), in direct contrast to Figure 4.5(b) where the effect from motion is almost absent. Introduction of MLC tracking is shown to

mitigate the effects of the applied motion upon the beam profiles and recovers the characteristics of the ‘no motion’ profile with minor discrepancies.

The results of axial beam profiles in the heterogeneous timber phantom with hidden Solid Water target are shown in Figure 4.5(e) and (f). Dose enhancement surrounding the higher density Solid Water hidden target is evident in the profiles. The effects of the applied motion and implementation of MLC tracking are similar to the observed effects in the homogeneous timber phantom where the magnitude of motion and the lateral range of the scattering electrons in the low-density medium interplay to cause greater discrepancy in the Left-Right direction.

To further investigate the impact of scattering conditions upon MLC tracking a 1D pass/fail gamma analysis (Low, 1998) was conducted on the 3DCRT results. Determination of the global normalisation gamma index in absolute dose was achieved with a 2%/2mm (Low, 2003) criterion and 0% dose threshold for each motion case beam profile compared with the ‘no motion’ case for DUO, Table 4.3. A 0% dose threshold was selected to include all measurement points within the comparison.

Table 4.3 Percentage agreement from global gamma analysis for 2%/2mm criterion for Superior-Inferior and Left-Right directions between ‘no motion’ (NM) and ‘motion’ (M) or ‘motion+tracking’ (MT) for 3DCRT plan delivery with DUO.

Motion Cases	Superior-Inferior Direction			Left-Right Direction		
	Solid Water	Homogenous Timber	Inhomogeneous Timber	Solid Water	Homogenous Timber	Inhomogeneous Timber
<i>NM-M</i>	27.2	19.3	17.7	76.4	4.7	16.1
<i>NM- MT</i>	99.6	100.0	100.0	91.7	86.2	79.5

Table 4.3 shows the global gamma analysis and the effectiveness of MLC tracking to mitigate the impact of motion. In the Solid Water scattering condition the percentage agreement between ‘no motion’ and ‘motion’ is 27.2% for the Superior-Inferior direction, with the implementation of MLC tracking the agreement between the axial profiles becomes 99.6%. For the homogeneous timber phantom, the motion is shown to have a greater effect as the initial agreement is 19.3%. Motion has

greater impact in the inhomogeneous timber phantom with the agreement reduced to 17.7%. With tracking the agreement between the beam profiles is found to be 100% for homogeneous and inhomogeneous scattering conditions in the Sup-Inf direction. For the Left-Right motion MLC tracking is shown to improve results for all scattering conditions and thus minimise the effects of motion upon the delivered dose distribution. It is shown to be less effective in the Left—Right direction in the inhomogeneous phantom than in the Solid Water phantom, this result may be attributed to the significant effect of the Sup-Inf motion to displace the central axis of the radiation beam from central axis of the detector.

The central pixel of the DUO detector was aligned to the linac treatment isocentre by the external room lasers, this point coincides with the centre of the hidden target and thus the PTV. A region of interest (ROI) was selected on each of the axial profiles to encompass the exact spatial location of the PTV (20 mm) and the mean absorbed dose calculated in this ROI and compared across the motion and scattering conditions investigated. The results of this analysis for the 3DCRT delivery are shown in Table 4.4 and Table 4.5.

Table 4.4 Mean absorbed dose in PTV for Superior-Inferior axial profiles of 3DCRT delivery.

Motion Cases	Solid Water		Homogenous Timber		Inhomogeneous Timber	
	Mean Dose in PTV (cGy)	Standard Deviation	Mean Dose in PTV (cGy)	Standard Deviation	Mean Dose in PTV (cGy)	Standard Deviation
<i>NM</i>	507.2	2.6%	458.6	4.5%	452.8	6.2%
<i>M</i>	430.0	30.0%	390.8	29.0%	392.8	28.7%
<i>MT</i>	504.7	4.3%	452.5	6.3%	448.6	7.5%

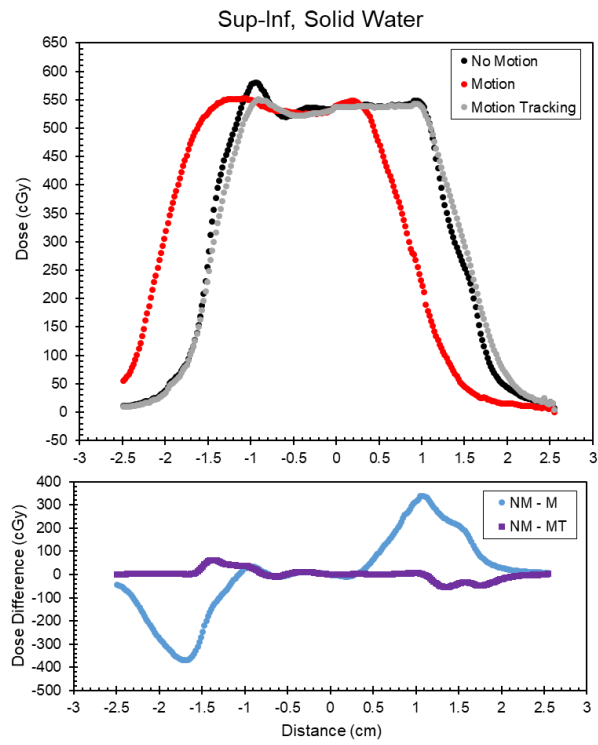
Table 4.5 Mean absorbed dose in PTV for Left-Right axial profiles of 3DCRT delivery.

Motion Cases	Solid Water		Homogenous Timber		Inhomogeneous Timber	
	Mean Dose in PTV (cGy)	Standard Deviation	Mean Dose in PTV (cGy)	Standard Deviation	Mean Dose in PTV (cGy)	Standard Deviation
<i>NM</i>	510.4	1.4%	468.6	2.3%	463.8	3.9%

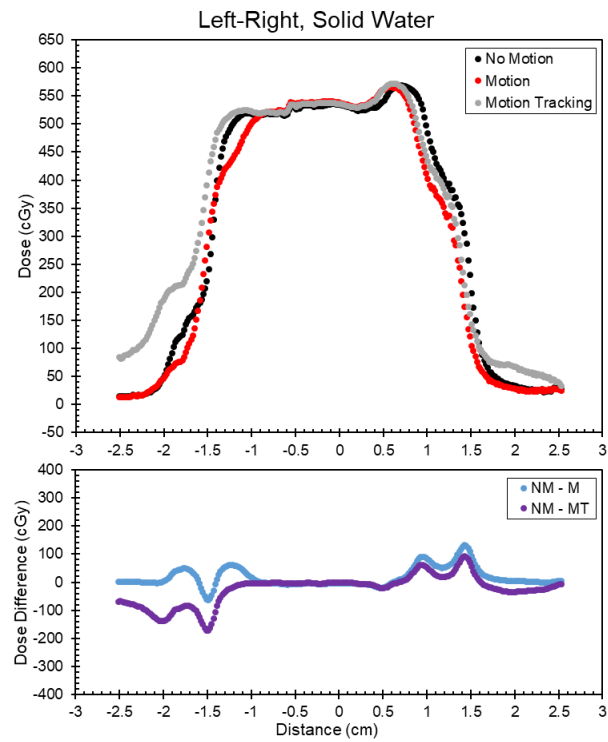
<i>M</i>	509.7	1.1%	428.7	6.3%	436.0	7.6%
<i>MT</i>	509.8	1.4%	467.0	2.5%	462.4	4.5%

The mean absorbed dose in the no motion case with Solid Water scattering achieves the prescription with 507.2 cGy delivered to the PTV. The introduction of the motion significantly affects the dose delivered to the PTV in the sup-inf direction, reducing the mean absorbed dose to 430 cGy. The introduction of the MLC tracking improves the delivery of dose to the PTV, achieving the prescription with 504.7 cGy mean dose. The introduction of the timber in the homogenous and inhomogeneous timber scattering conditions significantly affects the mean absorbed dose to the PTV as the dose in the PTV region decreases due to the significant change in density of the phantom material. In each case of scattering condition the MLC tracking system works effectively to compensate for the physical motion of the phantom and detector and achieve a dose delivered to the target similar to the case without motion.

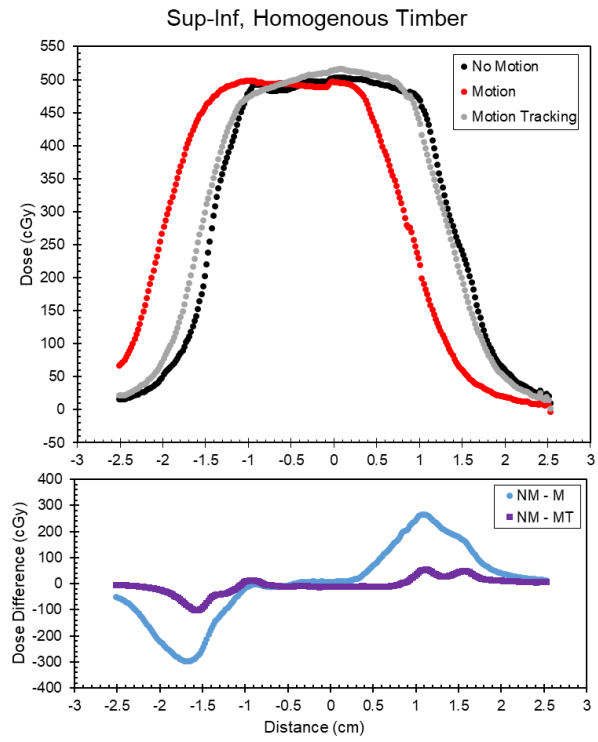
Figure 4.6 illustrates the results and direct comparison of the three motion cases for each scattering condition with an IMRT delivery.



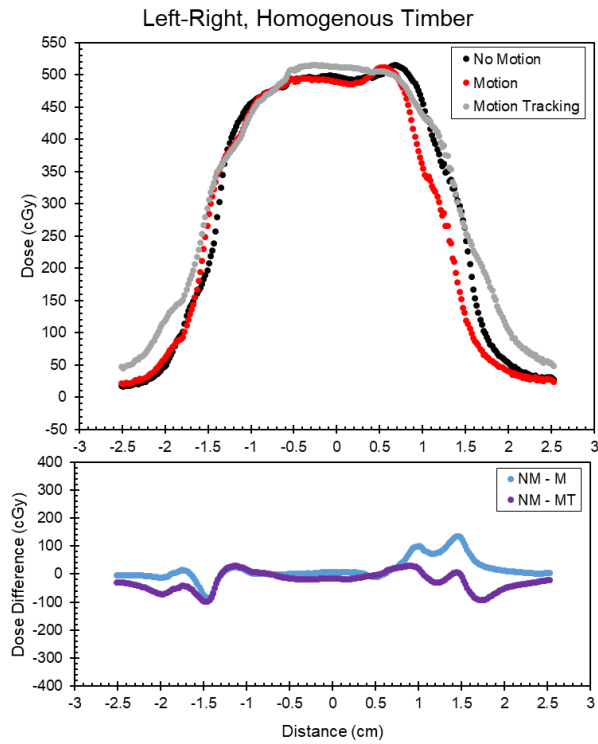
(a)



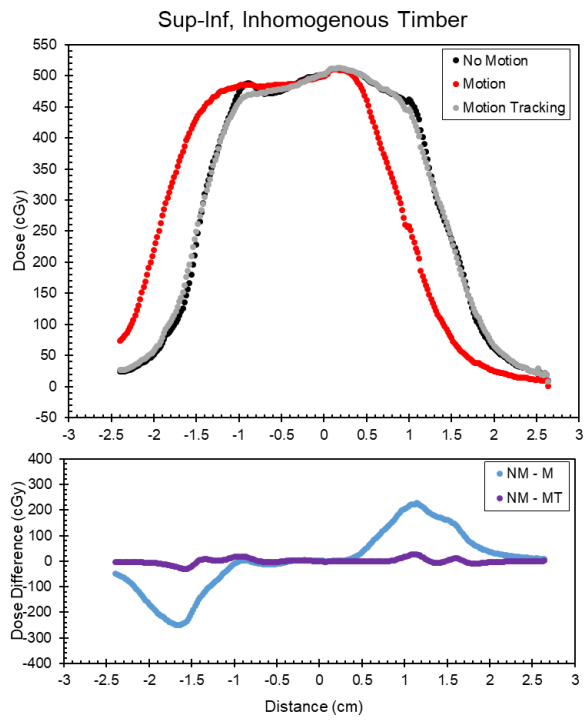
(b)



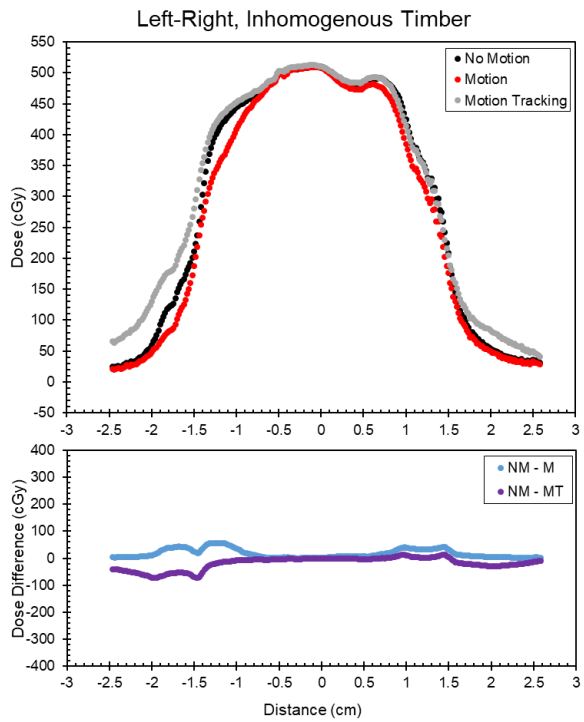
(c)



(d)



(e)



(f)

Figure 4.6 IMRT 6MV linac beam profiles for the three different scattering conditions and three different motion cases (No Motion, Motion and Motion+Tracking) using DUO and the corresponding point-to-point profile comparison. (a) Sup-Inf direction with homogenous Solid Water phantom. (b) Left-Right direction with homogenous Solid Water phantom. (c)

Sup-Inf direction with homogenous timber phantom. (d) Left-Right direction with homogenous timber phantom. (e) Sup-Inf direction with heterogeneous timber and Solid Water target phantom. (f) Left-Right direction with heterogeneous timber and Solid Water target phantom.

Table 4.6 and Table 4.7 present the mean dose results for the ROI analysis over the PTV for the IMRT delivery. The mean absorbed dose in the Solid Water scattering conditions without motion achieves the planned dose prescription to the PTV, 540 cGy. Introduction of the clinical patient motion significantly reduces the dose delivered to the PTV, the application of MLC tracking mitigates this influence and restores the dose to the PTV. As in the 3DCRT case, the motion is most influential in the superior-inferior direction. The reduced scattering conditions with the measurements in timber and inhomogeneous timber results in a reduction of the measured absorbed dose in the PTV and lessens the overall influential effect of the motion upon the delivered dose. The measured results, with sliding window IMRT delivery, agree with the 3DCRT results, demonstrating the efficacy of the MLC tracking system to mitigate the influences of the applied motion trace upon the delivered dose based upon a representative measurement in the PTV.

Table 4.6 Mean absorbed dose in PTV for Superior-Inferior axial profiles of IMRT delivery.

Motion Cases	Solid Water		Homogenous Timber		Inhomogeneous Timber	
	Mean Dose in PTV (cGy)	Standard Deviation	Mean Dose in PTV (cGy)	Standard Deviation	Mean Dose in PTV (cGy)	Standard Deviation
<i>NM</i>	539.9	2.3%	491.6	1.6%	487.2	3.0%
<i>M</i>	484.7	18.3%	445.7	17.7%	456.5	14.9%
<i>MT</i>	535.4	1.4%	497.3	3.3%	485.2	3.6%

Table 4.7 Mean absorbed dose in PTV for Left-Right axial profiles of IMRT delivery.

Motion Cases	Solid Water		Homogenous Timber		Inhomogeneous Timber	
	Mean Dose in PTV (cGy)	Standard Deviation	Mean Dose in PTV (cGy)	Standard Deviation	Mean Dose in PTV (cGy)	Standard Deviation

<i>NM</i>	533.1	3.1%	491.2	2.8%	485.2	4.1%
<i>M</i>	529.0	5.7%	479.7	6.4%	475.2	6.1%
<i>MT</i>	532.1	4.5%	494.2	4.5%	486.9	4.3%

4.4 Discussion

Adaptive radiotherapy (ART) aims to improve the outcome of radiation treatment through re-optimisation of patient treatments based on patient-specific changes in anatomy and biology during delivery. MLC tracking is one real-time motion adaptive strategy that applies real-time tumour localisation and tracking to modify and re-position the MLC shape during patient treatment. Patient specific quality assurance of MLC tracking treatments is complex due to the daily variations in a patients' tumour motion track, creating new adaptations each day. The use of the sDMG and DUO detectors for high spatial resolution beam profiling in motion adaptive radiotherapy lung treatments with MLC tracking has been investigated through the use of the detectors upon a HexaMotion motion platform to recreate patient-specific lung motion during irradiation.

Shown in Figure 4.3 are the axial profiles for the Superior-Inferior and Left-Right directions measured with DUO within the static homogenous timber phantom under exposure by a 6 MV linac compared with EBT3 film. The shape and features of the profiles are consistent between the detectors. From Table 4.1, DUO can reconstruct the FWHM of the delivered beam in a low-density medium with equivalent accuracy to EBT3 film, with at most an absolute difference of 0.015 mm between the two detectors. For the LHS PW the greatest difference between DUO and EBT3 film was 0.065 mm, demonstrating the agreement between the detectors.

In all scattering condition cases, and both 3DCRT and IMRT delivery techniques, the introduction of MLC tracking compensates for the effects of motion upon the dose distribution delivered, reducing the discrepancy for a motion scenario. MLC Tracking is shown to effectively mitigate the penumbral smearing and recover the characteristics of the beam profiles and doses delivered without motion.

4.5 Conclusion

Small MLC defined square fields were delivered to both the sDMG and EBT3 film for three motion cases to investigate the detectors dosimetric performance in adaptive deliveries. The cases investigated include: static platform (no motion), dynamic platform without motion tracking (motion) and dynamic platform with motion tracking (motion+tracking). The quantitative agreement between the sDMG and EBT3 film was established through measurement and comparison of the FWHM and penumbra widths for each beam profile. The agreement between the sDMG and EBT3 film for measurements of the FWHM of the static and dynamic radiation field deliveries was within 1.31%. The most significant disagreement between the detectors was observed in the measurements of the profiles penumbral width, with a maximum spatial difference of 0.58 mm between the individual detectors measurements for the 1 x 1 cm² dynamic radiation field with tracking.

It is observed that motion distorts the planned dose profile in the homogenous Solid Water, homogenous timber and heterogeneous timber phantoms. MLC tracking reduces the dose smearing significantly as demonstrated by the 'no-motion' and 'motion+tracking' results. The global gamma analysis of the axial beam profiles highlights the effectiveness of the MLC tracking system to compensate for the effects of motion upon delivered dose yielding excellent agreement between 'motion+tracking' beam profiles and 'no-motion' beam profiles in the 3DCRT delivery. The DUO and sDMG detectors have proven to be effective tools for pre-treatment verification of real-time adaptive stereotactic deliveries with high spatial resolution for dose profiling.

Chapter 5

Quality Assurance in Proton spot scanning radiation therapy

5.1 Introduction

This chapter aims to introduce the use of the sDMG and DUO detectors for lateral beam profile measurements in a clinical proton radiation beam, with energy 129.46 MeV, at the Francis H. Burr Proton Therapy Center (FHBPTC) at Massachusetts General Hospital (MGH). The measured results from sDMG and DUO for exposure to a proton pencil beam spot, used in proton pencil beam scanning, will be compared to measurements using a commercially available ion chamber array, MatriXX, used routinely in the clinic. The experimental results of an investigation will be presented into the efficacy and accuracy of the sDMG as a fast, independent proton energy verification system.

A published manuscript, of which I am the second author, uses the same experimental data presented here to compare with Monte Carlo simulations.

Merchant, A. H., **Newall, M.**, Guatelli, S., Petasecca, M., Lerch, M., Perevertaylo, V., Milluzzo, G., Petringa, G., Romano, F., Cirrone, G. A. P., Cuttone, G., Jackson, M. and Rosenfeld, A. B. (2017) 'Feasibility study of a novel multi-strip silicon detector for use in proton therapy range verification quality assurance', *Radiation Measurements*, 106, pp. 378–384. doi: 10.1016/j.radmeas.2017.03.017.

The first page of this manuscript is included in Appendix B.

5.2 Materials and Methods

The following experimental results were acquired at the Francis H. Burr Proton Therapy Center (FHBPTC) at Massachusetts General Hospital (MGH). The facility consists of a 235 MeV cyclotron (IBA dosimetry, Schwarzenbruck, Germany) providing a proton beam that is degraded and transported to one room with two fixed horizontal beams and two gantry equipped rooms (Tran, 2017), (DeLaney, 2007). The proton therapy system is capable of delivering a pencil beam spot with a range of 7 to 32 g/cm² and a full-width at half maximum (FWHM) of 20 to 35 mm. For a Gaussian distribution the FWHM is related to the standard deviation, σ , by:

$$FWHM = 2\sqrt{2 \cdot \ln 2} \sigma \quad (5.1)$$

The experimental measurements were acquired in a clinical therapy room with a rotating gantry for acquisition of data by the detector arrays with their measurement axes orientated either perpendicular for lateral profiles or parallel for edge-on acquisitions, to the proton pencil beam incidence. A pristine Bragg peak (PBP) proton pencil beam spot was used for irradiation of the detector systems with a spot size (σ) of 11 mm and energy 129.46 MeV at the treatment isocentre, which corresponds to a FWHM of 25.9 mm in air at isocentre and a range of 12.64 g/cm² to the distal 90% of the pristine Bragg peak in the PDD (R_{90}).

5.2.1 Equalisation of detector

The equalisation of the individual sensitivities and gain of each channel in the arrays of the sDMG and DUO detectors was carried out using a 6 MV linac, as described in 4.2.1. In summary, the detectors were exposed to the uniform intensity of a 20 x 20 cm² field size 6 MV photon beam at 10 cm depth in Solid Water with 10 cm of Solid Water backscattering material. The equalisation correction factor for each channel (CF_i) is calculated from the ratio of the individual response of each detector channel (R_i) to the average response of all channels in the array (\bar{R}).

$$CF_i = \frac{R_i}{\bar{R}} \quad (5.2)$$

The calculated correction factor per channel is uniquely applied to the measured response from each detector channel in the array.

$$R_{i,equalised} = \frac{R_i}{CF_i} \quad (5.3)$$

5.2.2 Lateral profiles

For the measurement and acquisition of lateral profiles of the PBP proton pencil beam spot, the detectors arrays; sDMG, DUO and the MatriXX ionization chamber array (IBA dosimetry, Schwarzenbruck, Germany) were placed upon the patient treatment couch and aligned at the treatment isocentre using the in-room lasers. The central axis of the detectors were aligned to the central axis of the proton pencil beam spot, such that the axis of measurement of the detector systems bisected the beam spot. Various depths of Solid Water were placed on top of the detectors for each measurement of the proton beam spot lateral profile, with 10 cm of polystyrene material beneath for backscattering. The following water equivalent depths were investigated; 13.8, 54.5, 105.1 and 125.9 mm with each depth repeated and measured using the sDMG, DUO and MatriXX. In this experiment the sDMG and DUO detectors are both enclosed within rigid PMMA holders which are recessed around the detectors at a water equivalent depth of 3.9 mm. The lateral profiles only of the proton pencil beam spot were analysed and quantitatively compared between the three detector systems by measuring the FWHM and penumbral widths (80%-20%) of the acquired measurements.

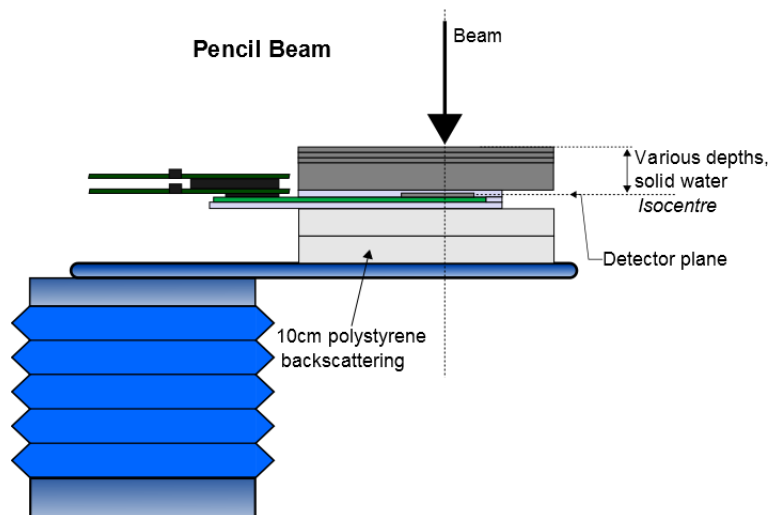
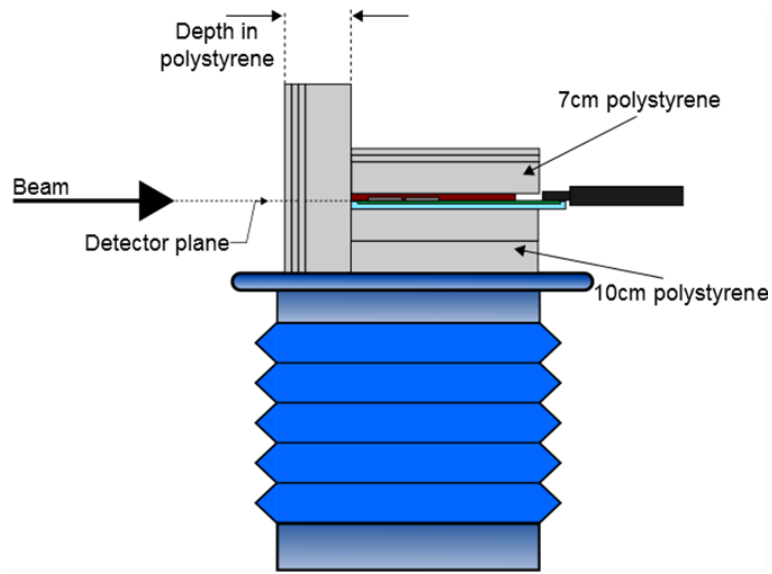


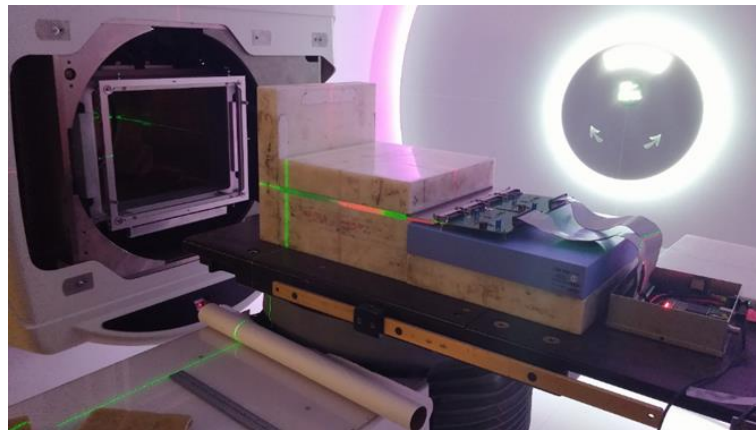
Figure 5.1 Schematic diagram (not to scale) of the experimental setup of DUO detector in proton pencil beam delivery for lateral profile measurements. Detector is positioned beneath increasing depths of Solid Water material and aligned with the central axis of the pencil beam and the treatment isocentre, setup is repeated for sDMG and MatriXX.

5.2.3 Edge-on acquisition

The edge-on acquisition of the proton pencil beam at MGH was conducted with the sDMG detector aligned using the in-room lasers to the treatment isocentre, with measurement axis of the detector parallel to the beam incidence. The gantry of the proton therapy delivery system was rotated to 270° to simplify setup of the system, Figure 5.2. Various depths of a polystyrene phantom material are placed in front of the linear array detector, manually degrading the energy of beam exiting the snout, until the pristine Bragg peak occurs within the sDMG and thus within the silicon sensitive volumes. Additional polystyrene phantom material is placed above and below the detector to improve scattering conditions. The depth of the sDMG detector in polystyrene is varied with depths investigated of 60, 70, 80 and 90 mm of polystyrene in front of the sDMG detector.



(a)



(b)

Figure 5.2 Schematic diagram (not to scale) of the experimental setup of edge-on acquisition of proton pencil beam spot delivery for pristine Bragg peak energy reconstruction with sDMG. (a) Schematic of experimental setup, various depths of polystyrene are placed in front of the detector. (b) Delivery of proton pencil beam spot to sDMG detector, the treatment isocentre is identified by the green lasers, aligned to the front of the sDMG.

5.2.4 Energy Reconstruction

Energy reconstruction of the incident proton pencil beam spot is achieved through accurate measurement of the location of the pristine Bragg peak in silicon within the sDMG linear detector array. The proton pencil beam to which the sDMG is exposed is mono-energetic, with energy of 129.46 MeV at the treatment isocentre, which corresponds to a range of 12.64 g/cm² to the distal 90% of the pristine Bragg peak in the PDD (R_{90}). Polystyrene phantom material of varying

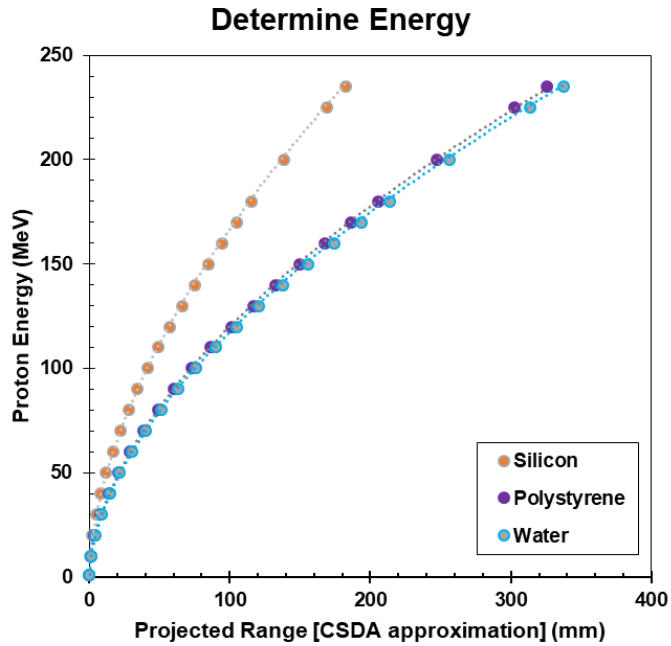
thicknesses are placed in front of the sDMG detector to degrade the energy of the beam and vary the position at which the pristine Bragg peak occurs within the silicon detector array. The physical measurement of the spatial coordinate of the initial Bragg peak, with depth in silicon, provides an effective means of determining the incident energy of the proton beam upon the detector based on the known geometry and materials of the phantom surrounding the detector.

The sDMG detector is encapsulated in a complex environment of varying materials which provide protection, provision of scattering material and a reduction of air surrounding the sensitive volumes of the detector array. The materials surrounding the silicon detector include; Solid Water and the printed circuit board (PCB) carrier. Due to the volume of Solid Water surrounding the detector, upon which the proton beam is incident, a broader scattered Bragg peak from the interaction of protons in the Solid Water material surrounding the detector is expected beyond the location of the initial Bragg peak in silicon. This is a result of the difference in the effective mass density of Solid Water $Z_{\text{eff}} = 1.032 \text{ g/cm}^3$ (*Solid Water® HE (Gammex™ Technology) - Sun Nuclear, 2020*) and the mass density of silicon, $Z_{\text{Si}} = 2.33 \text{ g/cm}^3$.

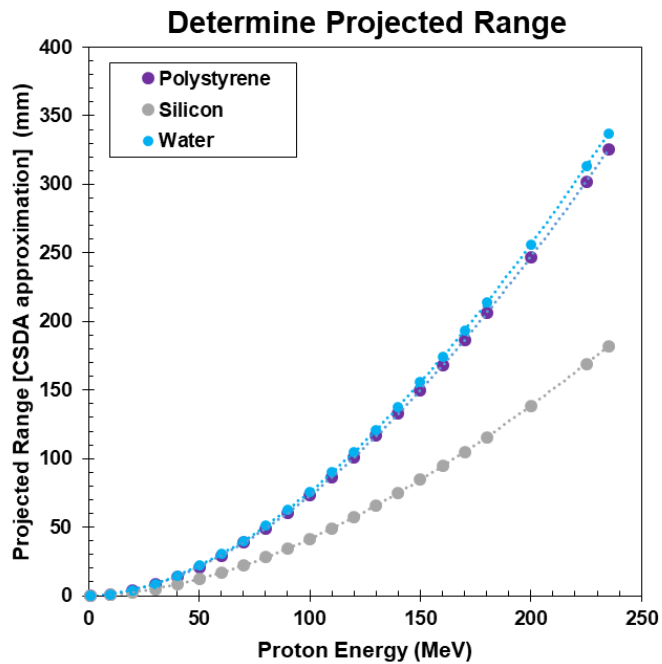
The energy of the incident proton beam is determined from the measurement of the Bragg peak in silicon utilising the assumptions and predictions of Continuous Slowing Down Approximation (CSDA). The CSDA range approximation assumes that the rate of energy loss of a charged particle along its track while traversing a medium is equal to the total stopping power within that medium, thus fluctuations in the rate of energy loss are neglected.

Determination of the initial energy of the proton beam upon the phantom surface from the measurement of the initial Bragg peak position in silicon requires determination of the predicted energy of the proton beam, which produces the peak in silicon, using the CSDA ranges of protons in silicon calculated by National Institute of Standards and Technology (NIST). The energy of the proton beam is thus determined, using the CSDA ranges of protons (Berger, 2017) in the preceding known thickness of phantom materials, for the various depths, the energy of the proton beam at the phantom surface can be reconstructed. The CSDA ranges for proton beams with energies from 1 to 235 MeV in silicon, polystyrene and water from NIST are shown in Figure 5.3. Fifth order polynomials are fitted to the data for each material across the proton energy range and using the

known geometry of the phantom the energy is reconstructed.



(a)



(b)

Figure 5.3 NIST calculated CSDA range for protons with energy from 1 to 235 MeV for silicon, polystyrene and water (Berger, 2017). (a) Visualised with Proton Energy as the ordinate and Projected Range the abscissa. (b) Visualised with Projected Range as the ordinate and Proton Energy the abscissa.

5.3 Results

5.3.1 Lateral Profiles

Figure 5.4 presents the results measured from the sDMG detector for 129.46 MeV proton pencil beam spot at various depths in Solid Water. The lateral profile of the beam spot measured by the sDMG is compared directly to the clinically measured profiles using the MatriXX ionisation chamber array under identical setup conditions. The response of the detectors are normalised to the maximum response at central axis, corresponding to the centre of the beam spot. The lateral profiles are aligned to the centre of the beam spot.

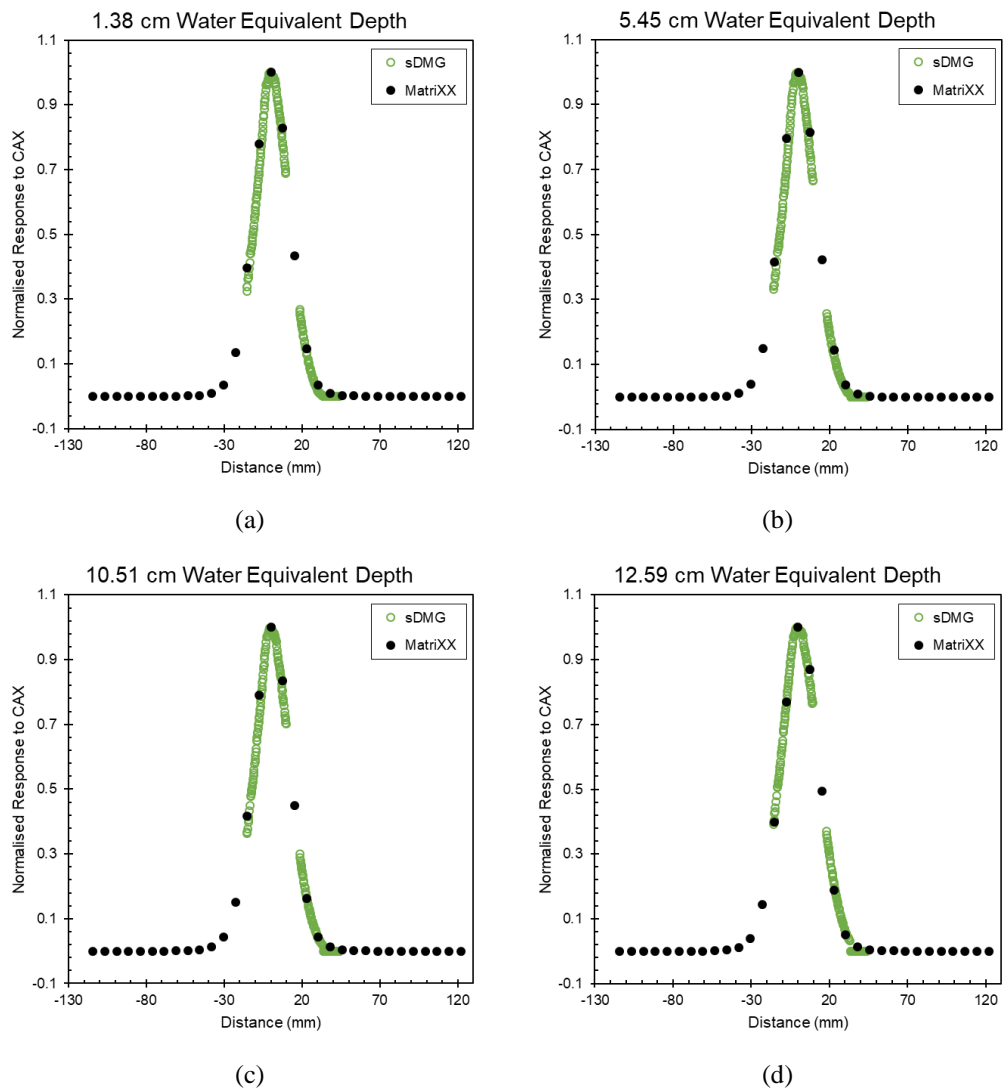


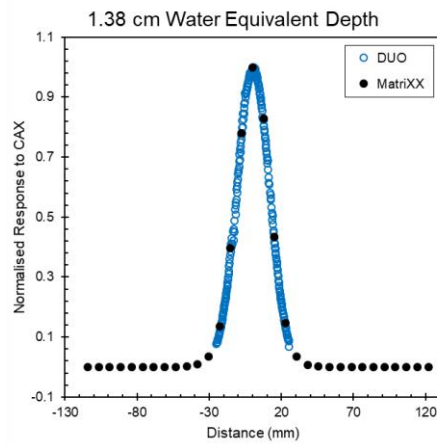
Figure 5.4 Lateral profiles of the proton pencil beam spot for varying depths in Solid Water compared between the sDMG and MatriXX. (a) 1.38 cm water equivalent depth. (b) 5.45 cm water equivalent depth. (c) 10.51 cm water equivalent depth. (d) 12.59 cm water equivalent depth.

Agreement between the quantitative measurements of the beam spots' FWHM and penumbral width for sDMG and MatriXX are presented in Table 5.1. These results were determined by fitting a sixth order polynomial to the response values on each side of CAX of the detectors in each array, to calculate the spatial coordinates of the 20%, 80% and 50% responses relative to the CAX, within each profile. For the sDMG detector the RHS penumbral width and FWHM are calculated and compared to the values determined by the MatriXX. The LHS penumbral width is not calculated due to the size of the pencil beam spot being greater than the length of the sDMG detector.

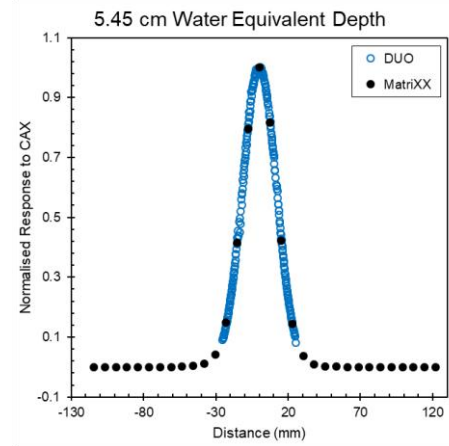
Table 5.1 sDMG and MatriXX measurements of FWHM and penumbral width for left hand side (LHS) only (20%-80%) for PBP pencil beam spot at different depths.

Water Equivalent Depth (mm)	sDMG		MatriXX		Difference (sDMG-MatriXX)	
	FWHM (mm)	Penumbra, RHS (mm)	FWHM (mm)	Penumbra, RHS (mm)	Δ FWHM (mm)	Δ RHS Penumbra (mm)
13.8	24.99	13.15	27.0	13.3	-2.01	-0.15
54.5	25.02	13.41	27.3	13.4	-2.28	0.01
105.1	26.34	14.06	27.8	13.6	-1.46	0.46
125.9	28.03	14.91	28.3	13.5	-0.27	1.41

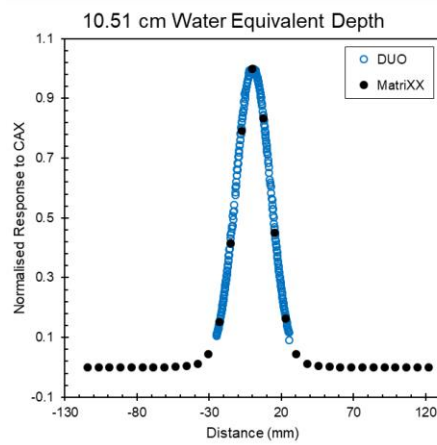
Figure 5.5 presents the results acquired from the DUO detector for the 129.46 MeV proton pencil beam spot, at the various depths in Solid Water investigated. The lateral profiles of the beam spot measured by DUO are compared directly to the clinically measured profiles using the MatriXX ionisation chamber array, which was exposed under identical experimental setup conditions. The response of the detectors are normalised to the maximum response at central axis, corresponding to the centre of the beam spot. The lateral profiles are aligned to the centre of the beam spot.



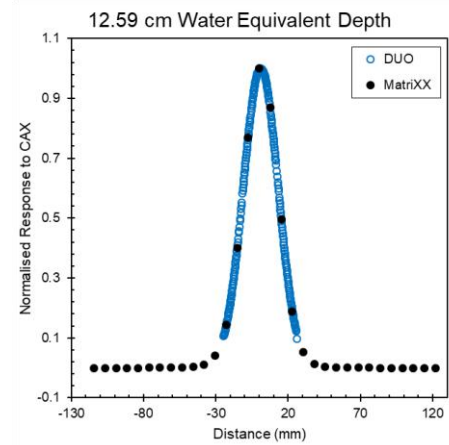
(a)



(b)



(c)



(d)

Figure 5.5 Lateral profiles of the proton pencil beam spot for varying depths in Solid Water compared between DUO and MatriXX. (a) 1.38 cm water equivalent depth. (b) 5.45 cm water equivalent depth. (c) 10.51 cm water equivalent depth. (d) 12.59 cm water equivalent depth.

Quantitative agreement between the measurements of the beam spot FWHM and penumbral width determined by DUO and MatriXX are presented in Table 5.2. These results were determined by fitting a sixth order polynomial to response values each side of CAX of the detectors, in each array, to calculate the spatial coordinates of the 20%, 80% and 50% responses relative to the CAX within each profile. The LHS and RHS penumbral widths and FWHM are calculated for DUO and compared to the values determined by the MatriXX.

Table 5.2 DUO and MatriXX measurement FWHM and penumbral width (20%-80%)

comparison for PBP pencil beam spot for different depths.

Water Equivalent Depth (cm)	DUO			MatriXX			Difference (DUO-MatriXX)		
	FWHM (mm)	Penumbra (mm)		FWHM (mm)	Penumbra (mm)		Δ FWHM (mm)	Δ Penumbra (mm)	
		LHS	RHS		LHS	RHS		LHS	RHS
13.8	26.24	12.34	12.55	27.0	13.7	13.3	-0.76	-1.36	-0.75
54.5	27.48	12.82	13.04	27.3	13.9	13.4	0.18	-1.08	-0.36
105.1	28.39	13.26	13.47	27.8	14.2	13.6	0.59	-0.94	-0.13
125.9	28.82	13.57	14.01	28.3	14.6	13.5	0.52	-1.03	0.51

The results summarised in Table 5.2 demonstrate agreement between DUO and MatriXX in measurement of the FWHM to within 1 mm over the range of water equivalent depths investigated.

5.3.2 Edge-on acquisition

The sDMG is exposed to a mono-energetic proton beam, with energy of 129.46 MeV at the treatment isocentre, which corresponds to a range of 12.64 g/cm² to the distal 90% of the pristine Bragg peak in the PDD (R₉₀). Polystyrene phantom material is placed in front of the detector in a series of thicknesses including; 60, 70, 80 and 90 mm. A coordinate system considering only depth in silicon is used for analysis of the measured results and determination of the spatial coordinate of the initial Bragg peak in silicon.

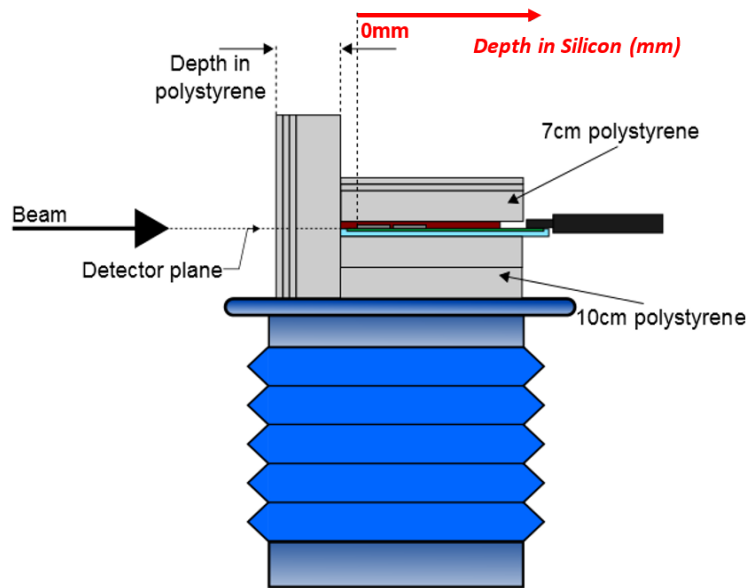
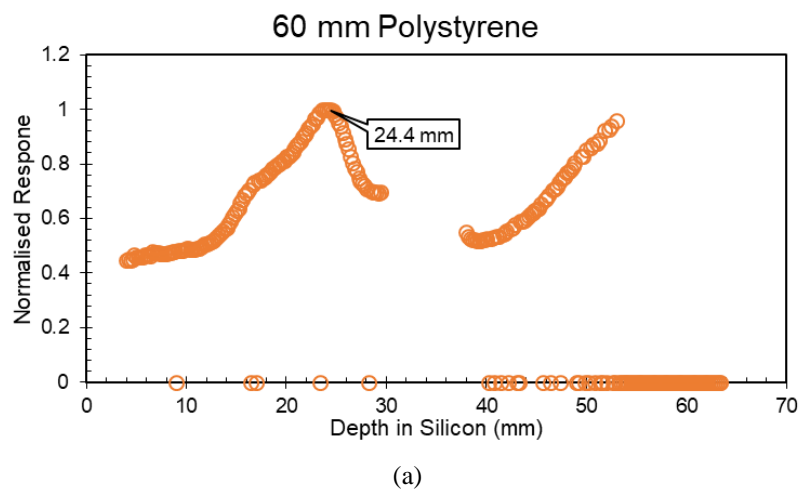
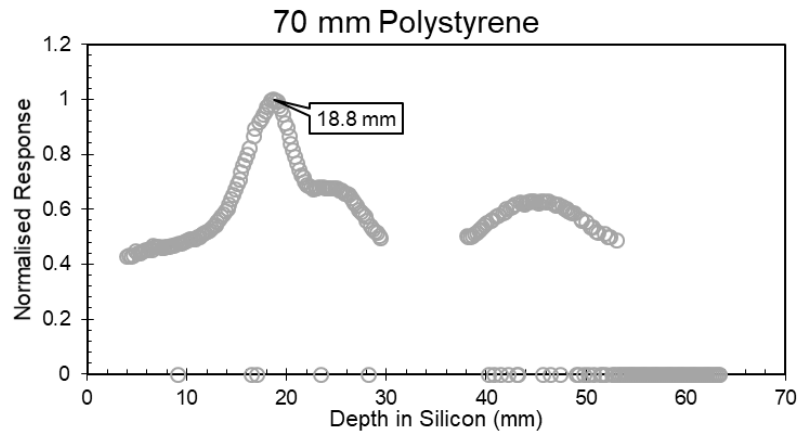


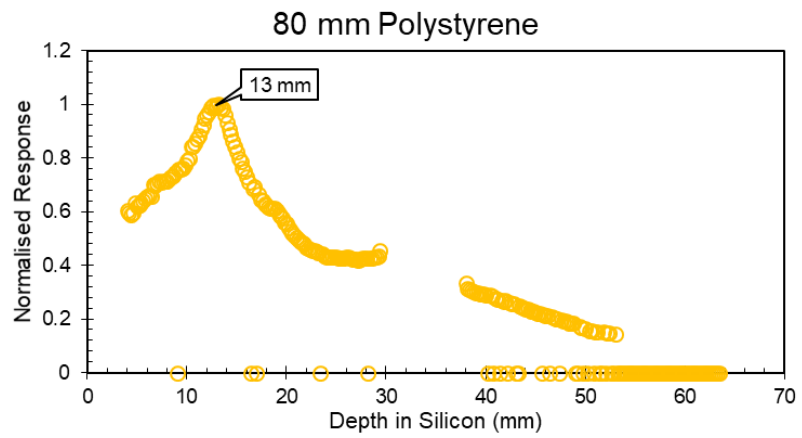
Figure 5.6 Schematic diagram (not to scale) of the experimental setup of the sDMG in edge-on acquisition with “Depth in Silicon” coordinate system described.

Figure 5.7 shows the measured results of the edge-on acquisition of the proton pencil beam spot for varying thickness of polystyrene phantom material in front of the detector. The response of the detector is normalised to the peak position of the Bragg peak for each individual depth investigated as accurate determination of the spatial coordinate in depth in silicon is the necessary measurement result.

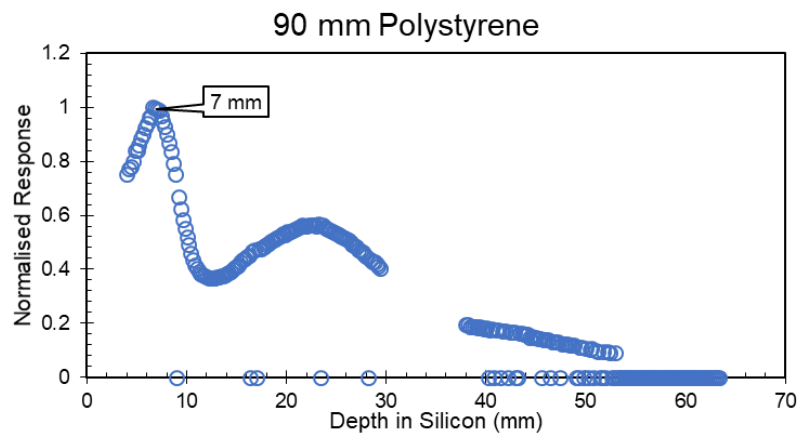




(b)



(c)



(d)

Figure 5.7 Results of the edge-on acquisition with sDMG in a proton pencil beam spot with varying thickness of polystyrene phantom material in front of the detector, with measured initial Bragg peak position highlighted in each callout box. (a) 60 mm polystyrene. (b) 70 mm polystyrene. (c) 80 mm polystyrene. (d) 90 mm polystyrene.

Table 5.3 summarises the results of the measured Bragg peak positions in silicon and the subsequently reconstructed proton beam energy at the phantom surface based on the CSDA range approximation for the varying thickness of polystyrene phantom material investigated. Based on the results of the experiment, the energy determined for the proton pencil beam incident upon the sDMG detector was calculated to be 129.2 ± 0.49 MeV (this uncertainty is quoted with a coverage factor of $k = 2$). The measurement agrees with the delivered energy of 129.46 MeV at isocentre, within the statistical uncertainty quoted of the measurement of the energy of the incident proton pencil beam using the sDMG.

Table 5.3 Results of the measured Bragg peak in silicon using the sDMG in edge on acquisition

Polystyrene phantom material preceding sDMG (mm) (± 0.5 mm)	Measured Bragg peak position in silicon (mm) (± 0.2 mm)	Predicted proton energy at phantom surface, E (MeV) (± 0.2 MeV)
60	24.4	129.5
70	18.8	129.4
80	13.0	129.1
90	7.0	128.9

5.4 Discussion

With the advent of proton pencil beam scanning systems, accurate beam data commissioning and beam modelling measurements are vital for the treatment delivery commissioning process. Establishing effective, independent and accurate means of conducting routine QA including identifying tools for routine quality assurance checks is necessary for efficient and safe delivery of advanced radiotherapy.

The sDMG and DUO detector systems were investigated for their capabilities to provide rapid, accurate and high spatial resolution measurements of a proton pencil beam spot and compared to the measured results of the MatriXX ionisation chamber array. The centre-to-centre distance between the ionization chambers of the MatriXX ionization chamber array is 7.62 mm (*MatriXX - Universal Detector Array / IBA Dosimetry, 2020*), compared to the silicon pixel spacing of 0.2 mm for both the sDMG and DUO detector arrays. In the results presented in Table 5.1 the significantly

higher spatial resolution of the sDMG detector compared to the MatriXX should result in a more accurate evaluation of FWHM, however the polynomial interpolation of the RHS spatial coordinate of the 50% response, in the space between the two silicon chips which compose the linear detector array of the sDMG, introduces uncertainty in the quantitative evaluation when compared to the MatriXX. This effect is also influential in the determination of the penumbral width using the sDMG. As such the agreement between the sDMG and the MatriXX for penumbral width measurements to within ± 0.5 mm is acceptable for the water equivalent depths 1.38, 5.45 and 10.51 cm. The measurement of the penumbral width at 12.59 cm water equivalent depth for the MatriXX of 13.5 mm should be greater in magnitude than the measurement at 10.51 cm water equivalent depth, this outlier generates an increased difference in measurement between the two systems. For FWHM, the results of Table 5.1 identify a systematic determination of the FWHM quantity to be less than measured by the MatriXX, this result is produced in part by the smaller volume of each pixel of the sDMG compared to the volume of the MatriXX ionisation chambers over which the signal is averaged.

It is evident that the physical dimensions and arrangement of DUO provides distinct advantages in enabling complete simultaneous two-dimensional acquisition of the proton pencil beam spot, such that the penumbral width of both LHS and RHS of the lateral profiles are measured simultaneously and quantified for comparison to the MatriXX, Figure 5.5. Table 5.2 demonstrates that the measured spot penumbrae are calculated to be sharper with the DUO evaluation than either the MatriXX or sDMG determinations. However, the sDMG evaluation may be influenced by the increased uncertainty due to the discontinuity in the profile measurement between the two linear arrays.

A Monte Carlo feasibility study was conducted for the sDMG detector and was related to its use in proton therapy range verification. The results of this study, which involved Monte Carlo simulation of the practical experimental measurements conducted in this chapter, demonstrated an excellent overall agreement between the experimental measurements and the simulation of the Bragg peak position in silicon, as measured in the sDMG detector (Merchant, 2017). The practical measured results for proton range verification using the sDMG, which are presented in Figure 5.7, demonstrate a series of detector pixels which return a measurement of zero. These pixels were found to be non-functional due to mechanical stresses.

5.5 Conclusion

Pencil beam spot profiles are an important characterization parameter of proton radiotherapy delivery in pencil beam scanning delivery systems. Quantitative measurement of spot profile characteristics with high spatial resolution detectors provides valuable information to the clinical department. Using the sDMG and DUO detectors the FWHM and penumbral width (80%-20%) were quantitatively measured for a proton pencil beam spot at water equivalent depths of 13.8, 54.5, 105.1 and 125.9 mm, with each depth repeated for measurement using the sDMG (Table 5.1), DUO (Table 5.2) and MatriXX detector systems for comparison. The sDMG and DUO calculated sharper FWHM and penumbral widths than the MatriXX ionization chamber array.

The sDMG detector was irradiated by the proton pencil beam spot in an edge-on acquisition mode to investigate a means of fast and independent method of proton beam energy verification. The reconstructed entrance energy at the phantom surface was calculated to be 129.5 ± 0.2 MeV, 129.4 ± 0.2 MeV, 129.1 ± 0.2 MeV and 128.9 ± 0.2 MeV for the thickness of 60, 70, 80 and 90 mm of polystyrene phantom material respectively, Table 5.3. This results in a mean energy determination of 129.2 ± 0.49 MeV, which compares accurately with the delivered proton beam energy of 129.46 MeV at the treatment isocentre.

The feasibility of using the high spatial resolution pixelated silicon detector arrays, sDMG and DUO, for quantitative measurements in proton pencil beam spot scanning systems has been demonstrated. DUO provides significant advantages in terms of simultaneous and spatially continuous acquisitions of high resolution dose profiles for accurate penumbral and FWHM measurements. Both sDMG and DUO demonstrate limitations in terms of capability to measure proton pencil beam spots beyond 40 mm in size.

Chapter 6

Energy Verification in heavy-ion radiation therapy

6.1 Introduction

The previous chapter described the results of independent energy verification measurements using the sDMG linear detector array in a proton pencil beam with energy 129.46 MeV. This chapter aims to introduce the use of the sDMG and TERA data acquisition system as a fast, independent energy verification system for use in charged particle therapy with a heavy ion carbon beam.

A published manuscript, of which I am the second author, uses the same experimental data to compare with Monte Carlo simulations.

Debrot, E., **Newall, M.**, Guatelli, S., Petasecca, M., Matsufuji, N. and Rosenfeld, A. B. (2018) ‘A silicon strip detector array for energy verification and quality assurance in heavy ion therapy’, *Medical Physics*, 45(2), pp. 953–962. doi: 10.1002/mp.12736.

The first page of this manuscript is included in Appendix B.

6.2 Materials and Methods

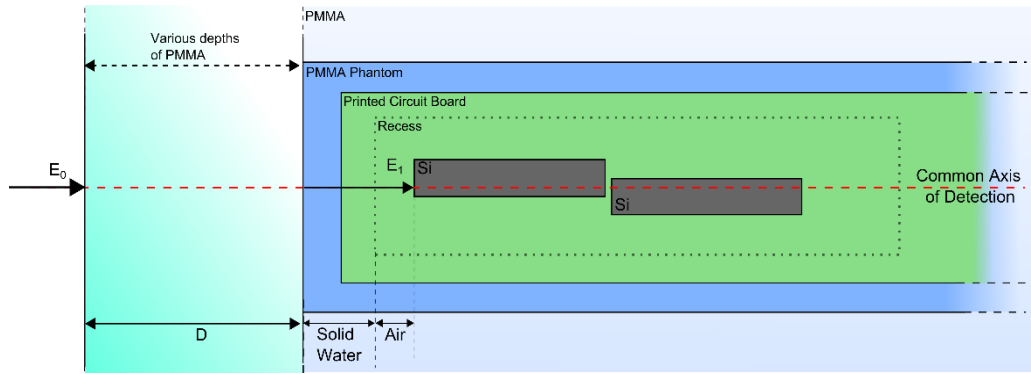
The experimental results presented here were conducted at the Heavy Ion Medical Accelerator in Chiba (HIMAC) with the National Institute of Radiological Sciences (NIRS), Japan.

The sDMG detector was irradiated in a research bunker with a fixed horizontal beamline using a mono-energetic ^{12}C ion beam with energy 290 MeV/U. The ^{12}C ion beam exits the vacuum beam port, within the bunker, and traverses an aluminium scattering filter and approximately 10 m of air before it is defined by a brass collimator with 10 x 10 cm² square field opening.

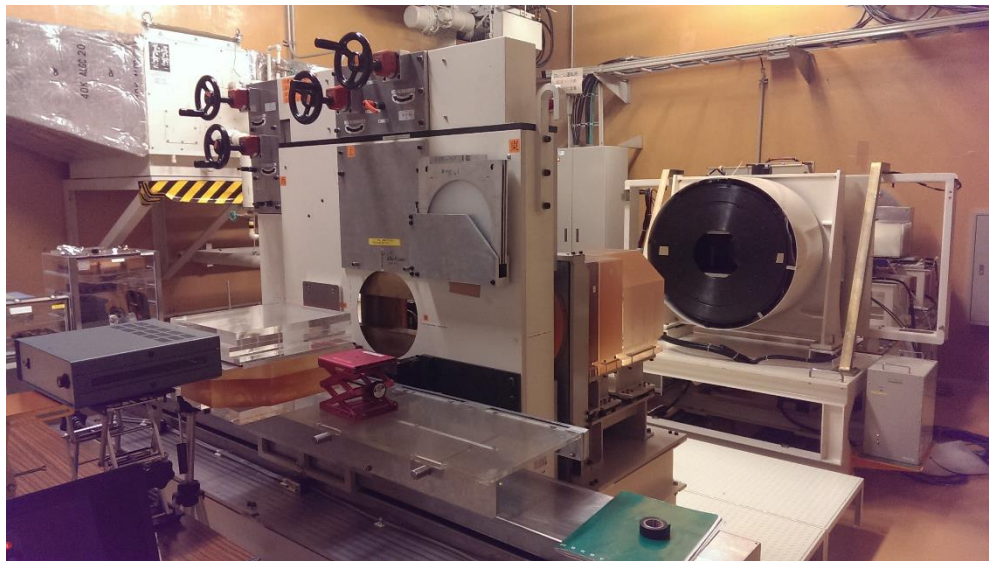
The measurement axis of the sDMG was orientated parallel to the direction of the ^{12}C ion beam for edge-on acquisitions of the pristine Bragg peak (PBP). The sDMG was carefully aligned to the central axis of the defined field by measurement and an independent external laser assembly. Known thicknesses of PMMA phantom material were placed directly in front of the sDMG detector to degrade the energy of the incident ^{12}C ion beam.

Various thicknesses were investigated to examine the deposition of the pristine Bragg peak within the sDMG detector. Figure 6.1(a) is a schematic representation (not to scale) of the exposure of the sDMG in the PMMA phantom to the incident mono-energetic ^{12}C ion beam orientated for edge-on acquisition. Figure 6.1(b) depicts the real experimental setup of the sDMG detector in edge-on acquisition mode to the ^{12}C ion beam at HIMAC.

The response of the sDMG detector was equalised for the individual sensitivities and gain of each channel in the array using a 6 MV linac. This exposure consisted of irradiation of the detector the uniform intensity of a 20 x 20 cm² field size 6 MV photon beam at 10 cm depth in Solid Water with 10 cm of Solid Water backscattering material. The equalisation correction factors were calculated following the procedure described in 5.2.1.



(a)



(b)

Figure 6.1 Setup of edge-on acquisition of sDMG detector in ^{12}C ion beam. (a) Schematic representation (not to scale) of the exposure of the linear detector array to the mono-energetic carbon ion beam for varying depths in PMMA phantom material. (b) Setup of experimental measurements at the carbon ion beam facility.

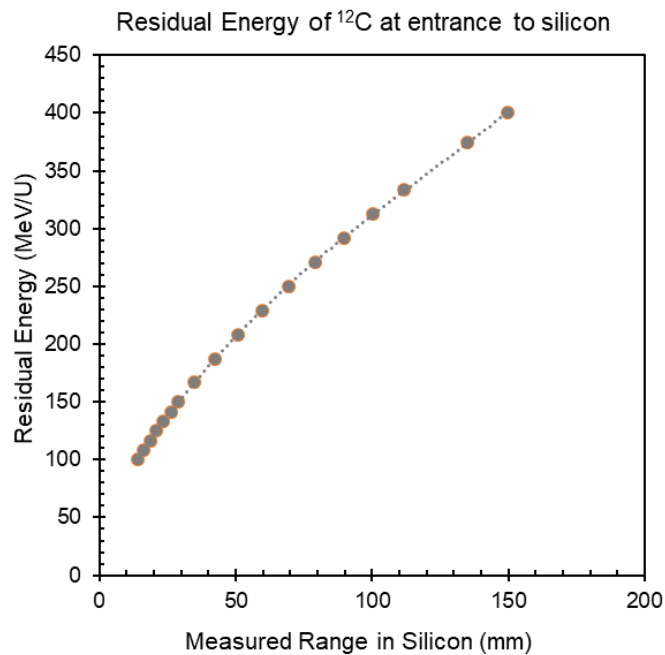
6.2.1 Energy Reconstruction

Energy reconstruction of the incident ^{12}C ion beam is achieved through accurate measurement of the location of the pristine Bragg peak in silicon within the sDMG linear detector array.

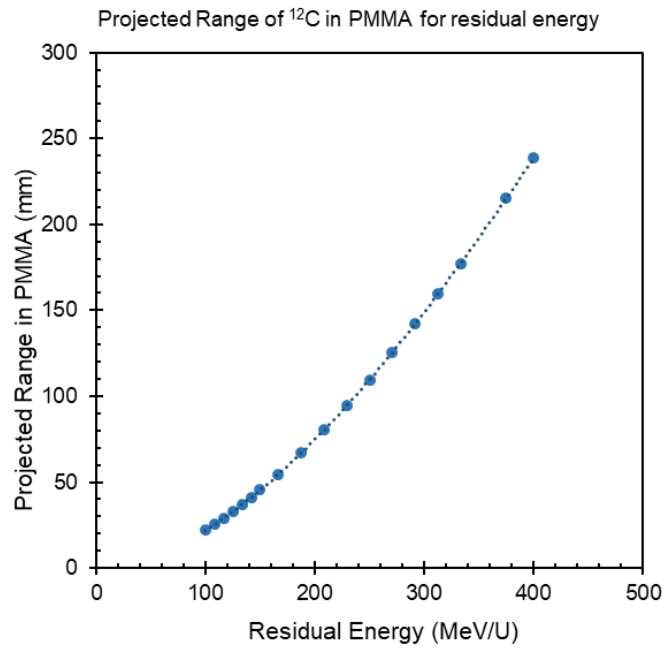
The ^{12}C ion beam is incident upon the surface of the PMMA phantom with energy 290 MeV/U (E_0 in Figure 6.1(a)). The energy of the mono-energetic ^{12}C ion beam degrades as it traverses the PMMA phantom, with the ^{12}C ion's reaching maximum range in the sDMG detector, producing a pristine Bragg peak in the detector. The depth of the pristine Bragg peak in silicon, measured within the

sDMG detector, is used to reconstruct the residual energy of the ^{12}C ion beam upon incidence on the silicon of the sDMG detector (E_1 in Figure 6.1(a)).

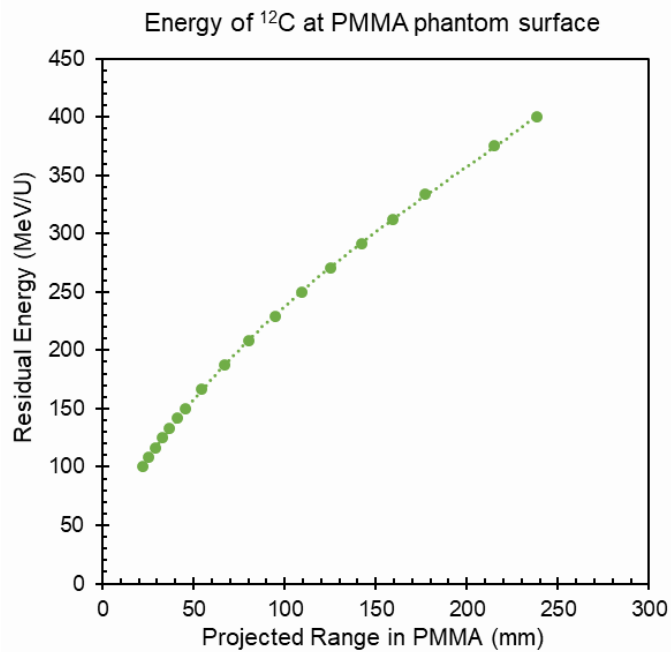
The energy of the incident ^{12}C ion beam is determined from the measurement of the Bragg peak in silicon utilising the calculations of the projected range in matter of ^{12}C ions of the SRIM-2013 software package (Ziegler, 2013), (Ziegler, 2010). SRIM (The Stopping and Range of Ions in Matter) is Monte Carlo simulation software package which calculates the range and stopping power of ions traversing different materials using a quantum mechanical treatment of ion-atom collisions. The software requires input of the type of ion, energy and target material and is able to calculate (but not limited to) the ion-penetration depth and energy deposition in target material. Using SRIM-2013 the projected range of ^{12}C ions was calculated between 100 MeV/U and 400 MeV/U for PMMA and silicon. The results were then plotted and fit with third order polynomials for the calculation and interpolation of; the residual energy (E_1) of ^{12}C ions at the entrance to silicon from Bragg peak measurement in silicon (Figure 6.2(a)), the projected range of ^{12}C ions in PMMA without silicon present (Figure 6.2(b)), and the energy of ^{12}C ions (E_0) at the PMMA phantom surface from measurement of Bragg peak in PMMA without silicon present (Figure 6.2(c)).



(a)



(b)



(c)

Figure 6.2 The calculated projected ranges from SRIM-2013 (Ziegler, 2013). (a) Determination of residual energy of ^{12}C ions at the entrance to silicon from Bragg peak measurement in depth of silicon. (b) Determination of the projected range of ^{12}C ions in PMMA without silicon present. (c) Determination of the energy of ^{12}C ions at the PMMA phantom surface from measurement of Bragg peak in PMMA without silicon present.

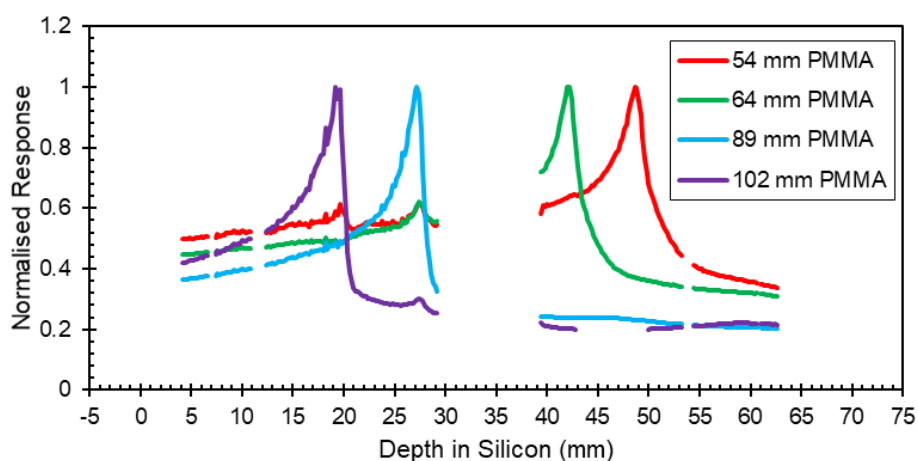
The energy of the ^{12}C ion beam is reconstructed from the measurement of the pristine Bragg peak location in the silicon sDMG detector array using the calculation method described above for various depth of PMMA phantom material.

The sDMG detector is encapsulated in a complex environment of varying materials which provides protection, provision of scattering material and a reduction of air surrounding the sensitive volumes of the detector array. The materials surrounding the silicon detector include; Solid Water and the printed circuit board (PCB) carrier. Due to the energy and nature of the ^{12}C ions in the beam incident upon the PMMA phantom, unlike in the proton beam irradiation, a secondary phantom scatter peak is not expected.

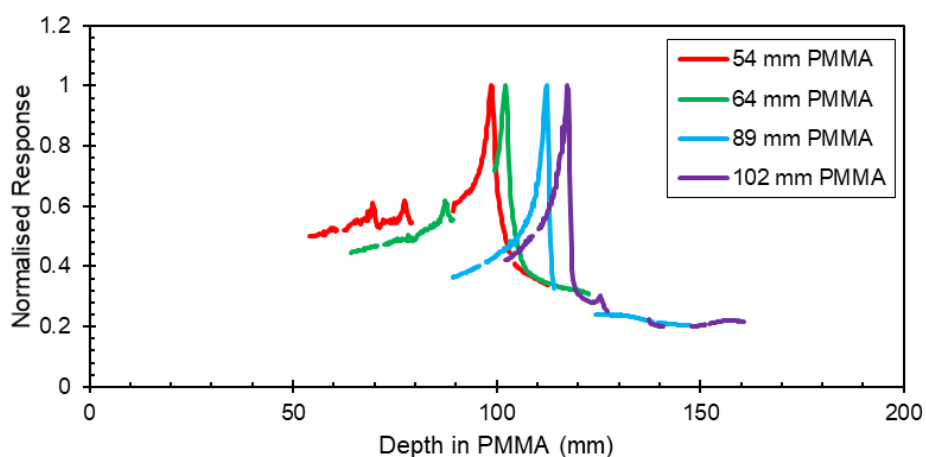
6.3 Results

The sDMG is exposed to a mono-energetic ^{12}C ion beam, with energy of 290 MeV/U exiting the vacuum port. PMMA phantom material is placed in front of the detector in a series of thicknesses including; 54, 64, 89 and 102 mm. A coordinate system considering only depth in silicon is used for first visualisation of the measured results with equalisation factor applied, Figure 6.3(a).

The overall shape of the pristine Bragg peak measured by the sDMG detector clearly demonstrates the peak of maximum dose deposition, which is defined and can be accurately localised in the linear array. Figure 6.3(b) illustrates the measured results aligned in depth in PMMA, which is used for localisation of the pristine Bragg peak. The pristine Bragg peak measured by the sDMG detector in silicon in the ^{12}C ion beam is more defined than compared to the measurements in the proton pencil beam due to reduced Coulomb scattering in the ^{12}C ion beam.



(a)

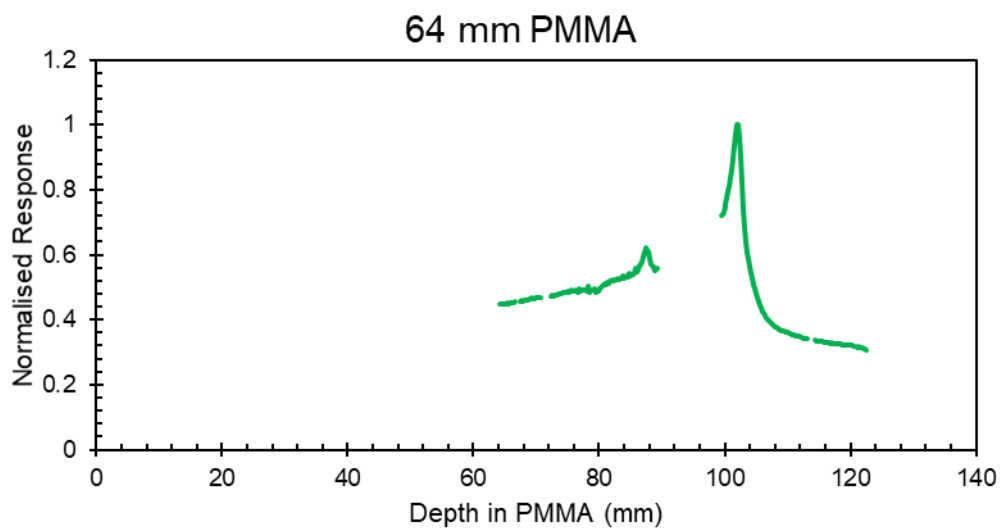
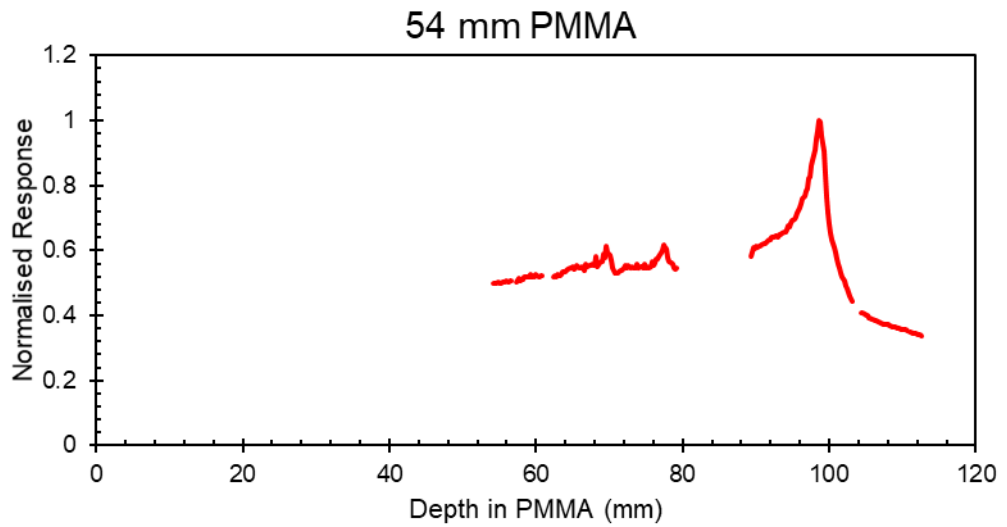


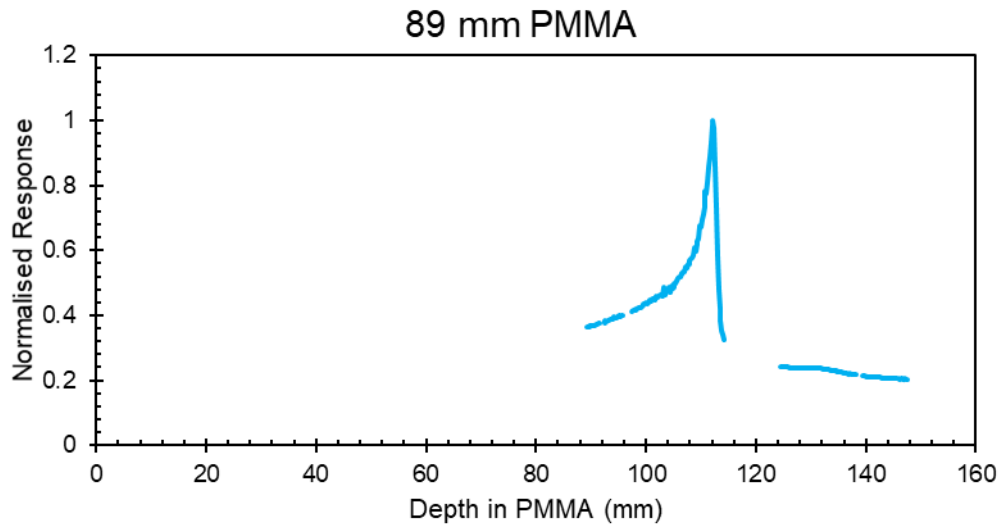
(b)

Figure 6.3 Combined measurements results of sDMG detector exposed to ^{12}C ion beam in edge-on acquisition mode with varying depths of PMMA phantom material preceding detector. (a) Results presented with abscissa describing the depth of the pristine Bragg peak delivered in depth in Silicon of linear sDMG array. (b) Results presented with abscissa describing the depth of PBP delivered in depth in PMMA phantom.

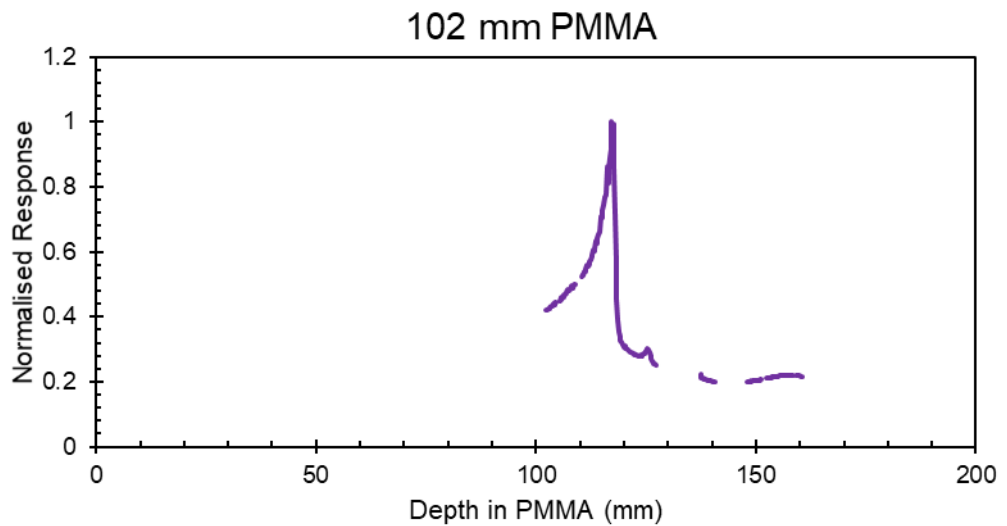
The measurement of the location of the pristine Bragg peak within the silicon detector (at a known depth in the PMMA phantom) is completed after each acquisition. The energy of the beam (E_1) at entrance to the silicon detector is calculated from the experimental measurement of the location of the pristine Bragg peak within the detector. The measured location of the pristine Bragg peak in PMMA (projected range without silicon + build-up PMMA) is determined from this calculated energy (E_1). The energy (E_0) at the entrance to the PMMA phantom is calculated from the measured

location of the pristine Bragg peak in PMMA (without silicon) following the energy reconstruction method described, 6.2.1.





(c)



(d)

Figure 6.4 Individual measurements results of sDMG detector exposed to ^{12}C ion beam in edge-on acquisition mode with varying depths of PMMA phantom material preceding detector. (a) 54 mm PMMA. (b) 64 mm PMMA. (c) 89 mm PMMA. (d) 102 mm PMMA.

The results of the measurement of the pristine Bragg peak position for a ^{12}C ion beam incident upon a PMMA phantom of various thicknesses and the subsequent calculation of the energy of the ^{12}C ion beam at the PMMA phantom surface is presented in Table 6.1.

Table 6.1 Results of the measurement of the pristine Bragg peak location in the sDMG detector for various depths of PMMA phantom material and the calculation of the incident ^{12}C ion beam energy at the PMMA phantom surface (E_0).

PMMA Build-up Material (mm) (± 0.5 mm)	Measured peak location in silicon (mm) (± 0.2 mm)	Calculated residual energy, E_1 (MeV/U) (± 0.7 MeV/U)	Projected range in PMMA without silicon from phantom surface (mm) (± 0.7 mm)	Calculated Energy, E_0 (MeV/U) (± 0.5 MeV/U)
54	48.8	119.5	132.4	278.8
64	42.2	143.7	131.2	277.8
89	27.2	186.3	130.3	278.8
102	19.5	203.4	131.1	280.4

Based on the results of the experiment, the energy determined for the ^{12}C ion beam incident upon the sDMG detector was calculated to be 278.9 ± 2.1 MeV (this uncertainty is quoted with a coverage factor of $k = 2$).

6.4 Discussion

A Monte Carlo simulation of the experimental setup was conducted by Debrot et al. (Debrot, 2018) with the simulated average energy of the ^{12}C ion beam at the surface of the PMMA phantom determined to be 280 ± 0.2 MeV/U. The measurement of 278.9 ± 2.1 MeV using the sDMG over various thickness of PMMA agrees with the simulated energy of 280 ± 0.2 MeV/U at the PMMA phantom surface, within the statistical uncertainty quoted for the measurement of the energy of the incident ^{12}C ion beam using the sDMG. Disagreement between the measured and expected values for the ^{12}C ion beam incident at the surface of the PMMA phantom is attributed to potential uncertainties present in the thicknesses of absorber materials placed in front of the sDMG detector as well as uncertainties related to the degradation of the energy of the beam prior to incidence upon the phantom.

The sDMG detector was irradiated in a research bunker with a fixed horizontal beamline using a mono-energetic ^{12}C ion beam with energy 290 MeV/U. The deposition of the pristine Bragg peak is

evident in the sDMG detector for each depth of PMMA investigated, shown in Figure 6.4. Visualised in depth in silicon, Figure 6.3(a), it is also evident that individual smaller peaks occur in regions of the detector previously irradiated by the ^{12}C pristine Bragg peak. These smaller peaks, occurring at depths of 21 and 27 mm, are attributed to radiation damage defects generated by the previous measurement at depth in PMMA, measured with the same sDMG detector.

Additionally, the smaller peaks are evident because the equalisation correction factors applied to the results acquired by the sDMG detector are generated by uniform MV photon irradiation, thus are not accounting for the non-linear localised variations in individual sensitivity of the detectors channels caused by the defects generated by the high LET ^{12}C radiation at the distal end of the pristine Bragg peak.

Prolonged exposure of the silicon detector sDMG to the ^{12}C ion beam in edge-on acquisition mode was found to yield visible radiation damage defects in the form of non-linear localised variations in individual sensitivity of the detectors channels. The presence of these effects does not influence the accuracy of the energy reconstruction method described as the defects are highly localised within the detector.

Deposition of energy beyond the distal edge of the pristine Bragg peak, measured by the sDMG, is attributed to the lateral scattering of ^{12}C ions into the detector which have a comparatively extended range in the surrounding scattering materials of the PCB relative to the silicon detector.

6.5 Conclusion

A method of calculating the energy of the incident ^{12}C ion beam from the measurement of the Bragg peak in silicon was developed utilising the calculated projected range in matter of ^{12}C ions from the SRIM-2013 software package. The residual energy (E_1) of ^{12}C ions at the entrance to silicon is determined from the measurement of the pristine Bragg peak location in silicon, the projected range of ^{12}C ions in PMMA without silicon present is then calculated and the energy of ^{12}C ions (E_0) at the PMMA phantom surface is determined based on the known thicknesses of PMMA from calculation of the pristine Bragg peak location in PMMA without silicon present. Based on the results of the experiment, the energy determined for the ^{12}C ion beam incident upon the sDMG

detector was calculated to be 278.9 ± 2.1 MeV (this uncertainty is quoted with a coverage factor of $k = 2$). The results of this experimental work demonstrate the feasibility of the sDMG detector for use in energy verification of a mono-energetic ^{12}C ion beam.

Chapter 7

Conclusions

7.1 Summary

The Serial Dose Magnifying Glass (sDMG), is a multi-strip silicon detector comprised of two linear arrays of 128 diodes with pitch 0.2 mm. The radiation damage study illustrates the sDMG detectors' increase in response and stabilisation of the charge collection efficiency across all pixels within the array to within +/-5% after 40 kGy of accumulated uniform dose. The linearity of the detector's accumulated charge response to delivered dose from a 6 MV linac photon beam was examined within the range 50 cGy to 500 cGy. The R^2 of the linear fitting function was determined to be 0.99999 and the conversion factor found to be 105 pC/cGy/pixel. The sDMG exhibits a maximum dose per pulse dependence of approximately 40% across the range of 2.1×10^{-5} Gy pulse⁻¹ to 2.78×10^{-4} Gy pulse⁻¹ investigated. The response of the sDMG detector was normalised to the response of the CC13 ionisation chamber irradiated under identical conditions. These results were used to generate a series of correction factors to account for the dose per pulse dependence within the sDMG detector. PDD measurements for the sDMG were compared to a Markus ionisation chamber over the range 0.5 cm to 25 cm depth in Solid Water. Initially the exhibited agreement between the Markus IC and sDMG is within +/-8% for depths less than 5 cm in Solid Water, at greater depths the percentage difference between the sDMG and Markus chamber increases to a maximum of 20%. The discrepancy between the response of sDMG and the Markus IC is attributed to the intrinsic dose per pulse dependence of the sDMG. Utilising the calculated correction factors the observed

maximum difference is reduced from $\pm 20\%$ to $\pm 4\%$ with the sDMG response maintaining agreement within $\pm 1.27\%$ for depths greater than 1.5cm in Solid Water. A series of output factors for the sDMG were measured and compared to EBT3 film for field sizes ranging from $0.5 \times 0.5 \text{ cm}^2$ up to $10 \times 10 \text{ cm}^2$. For field sizes less than $1.5 \times 1.5 \text{ cm}^2$ the sDMG is observed to under-respond up to a maximum of 3.3%, for the field size of $0.5 \times 0.5 \text{ cm}^2$, relative to EBT3 film. For field sizes greater than $1.5 \times 1.5 \text{ cm}^2$ the sDMG detector is observed to over-respond relative to EBT3 film with the agreement remaining within $\pm 2\%$. The disagreement between the EBT3 film and sDMG without dose rate dependence correction is within 8%, with dose rate dependence correction agreement is within 3.1%. Normalised beam profile measurements were conducted for field sizes between $0.5 \times 0.5 \text{ cm}^2$ and $4 \times 4 \text{ cm}^2$ and compared between the sDMG and EBT3 film. The sDMG detector exhibited agreement to within 0.90 % for the determination of the FWHM of the radiation field sizes when compared with EBT3 film measurements. The disagreement in penumbral width measurements between sDMG and EBT3 film was found to be at most 60 μm difference for static 6 MV photon beam delivery. This disagreement between the detectors is restricted to the submillimeter scale and is at most 0.45 mm in the case of FWHM comparison.

From these measurements of dose linearity, dose per pulse dependence, PDD, beam profiling and output factor the sDMG was demonstrated to perform accurately and effectively as a QA tool for small radiation beam deliveries.

The use of the sDMG and DUO detectors for high spatial resolution beam profiling in motion adaptive radiotherapy lung treatments with MLC tracking has been investigated. The quantitative agreement between the sDMG and EBT3 film was established through measurement and comparison of the FWHM and penumbra widths for each beam profile. The agreement between the sDMG and EBT3 film for measurements of the FWHM of the static and dynamic radiation field deliveries was within 1.31%. DUO is shown to reconstruct the FWHM of the delivered beam in a low-density medium with equivalent accuracy to EBT3 film, with at most an absolute difference of 0.015 mm between the two detectors. For the LHS PW the greatest difference between DUO and EBT3 film was 0.065 mm, demonstrating the agreement between the detectors. In all scattering condition cases, and both 3DCRT and IMRT delivery techniques, the introduction of MLC tracking compensates for the effects of motion upon the dose distribution delivered, reducing the discrepancy

for a motion scenario. MLC Tracking is shown to effectively mitigate the penumbral smearing and recover the characteristics of the beam profiles and doses delivered without motion.

The DUO and sDMG detectors have proven to be effective tools for pre-treatment verification of real-time adaptive stereotactic deliveries with high spatial resolution for dose profiling.

With the advent of proton pencil beam scanning systems, accurate beam data commissioning and beam modelling measurements are vital for the treatment delivery commissioning process. The sDMG and DUO detector systems were investigated for capabilities to provide rapid, accurate and high spatial resolution measurements of a proton pencil beam spot and their results are compared to the measured results of the MatriXX ionisation chamber array. Using the sDMG and DUO detectors the FWHM and penumbral width (80%-20%) were quantitatively measured for a proton pencil beam spot at water equivalent depths of 13.8, 54.5, 105.1 and 125.9 mm, with each depth repeated for measurement using the sDMG, DUO and MatriXX detector systems for comparison. The sDMG and DUO calculated sharper FWHM and penumbral widths, respectively than the MatriXX ionization chamber array.

The sDMG detector was irradiated by the proton pencil beam spot in an edge-on acquisition mode to investigate a means of fast and independent proton beam energy verification. The reconstructed entrance energy at the phantom surface was calculated to be 129.5 ± 0.2 MeV, 129.4 ± 0.2 MeV, 129.1 ± 0.2 MeV and 128.9 ± 0.2 MeV for the thickness of 60, 70, 80 and 90 mm of polystyrene phantom material respectively. This results in a mean energy determination of 129.2 ± 0.49 MeV, which compares accurately with the delivered proton beam energy of 129.46 MeV at the treatment isocentre. The sDMG detector was also irradiated using a mono-energetic ^{12}C ion beam with energy 290 MeV/U in edge-on acquisition mode. Based on the results of this experiment, the energy determined for the ^{12}C ion beam incident upon the sDMG detector was calculated to be 278.9 ± 2.1 MeV (this uncertainty is quoted with a coverage factor of $k = 2$). The measurement of 278.9 ± 2.1 MeV using the sDMG over various thickness of PMMA agrees with the expected energy of 280 ± 0.2 MeV/U at the PMMA phantom surface, within the statistical uncertainty quoted for the measurement of the energy of the incident ^{12}C ion beam using the sDMG.

The sDMG detector is shown to provide a fast, accurate and independent means of range and energy verification in both proton pencil beams and carbon-ion beams.

Despite the limitations relating to dose per pulse dependence and physical size for both DUO and sDMG, the detectors have demonstrated uniquely valuable performance in providing high spatial resolution measurements of small radiation fields in homogenous and heterogeneous scattering conditions for accurate validation of static and dynamic delivery techniques. Furthermore, an efficient and practical methodology is presented utilising the sDMG for independent energy verification in proton and carbon-ion radiation beams.

7.2 Impact & Future Directions

The detailed investigation conducted in this work into the first version of the high spatial resolution silicon detectors sDMG and DUO, developed at CMRP, and fabricated on bulk silicon substrates, allowed for a clear demonstration of their advantages and initial shortcomings. These initial shortcomings and limitations included; discontinuities in measurement axis (sDMG), limiting overall physical dimensions and dose per pulse dependence. However these limitations were determined in combination with highly valuable accuracy and performance characteristics with high spatial resolution. These detectors merit further investigation in both small field photon dosimetry as well as independent energy verification for proton and heavy-ion therapies.

The importance of this work is that it pioneered firstly the use of the high spatial resolution pixelated Si dosimeters for QA in EBRT MART and has directly led to the production of the second (low resistivity bulk) and third generation (epitaxial) silicon 1D and 2D family of CMRP dosimeters (DMG 256 , DUO, Octa and M512).

Biasi et al. (Biasi, 2018) investigated a 2D monolithic silicon array, fabricated on a high resistivity p-type epitaxial layer, with 512 detectors across four linear arrays arranged with a shared central detector and the linear arrays at 45° relative to each other. Output factors, dose profiles, dose per pulse dependence and PDDs were investigated across flattening filter free and flattened photon beams of energy 6MV and 10MV.

Stansook et al. (Stansook, 2019) described and investigated the changes in performance characteristics of the family of 2D monolithic silicon detector arrays, consisting of M512, DUO and Octa, which were initially fabricated on bulk p-type substrates and are now subsequently fabricated on epitaxial p-type substrates. The output factors, off-axis ratios and PDDs in square 6MV and 10MV flattened photon radiation fields were presented.

Causer et al. (Causer, 2019) conducted a preliminary investigation into a monolithic silicon strip detector (sDMG-256) which consists of 256 detectors in a single continuous linear array, with 0.2 mm pitch on a bulk p-type silicon substrate, for use in a static magnetic field of 1.2 T under exposure to small photon beams with energy 6MV and 10MV.

Causer et al. (Causer, 2020) reported on an investigation using DUO for Bragg peak detection in a therapeutic quality proton beam with a 0.95 T transverse magnetic field.

Alnaghy et al. (Alnaghy, 2020) utilised a 512 channel monolithic silicon detector array (M512) arranged in a 22 x 22 grid, fabricated on an epitaxial p-type silicon substrate, to investigate the feasibility of dose measurement in a 1.0 T inline MRI-linac during MR imaging.

The initial findings and characterisations conducted in this work, for these detectors in MART and charged particle radiation therapy, has resulted in advanced performance of CMRP detectors which is outlined in the many peer review papers of my colleagues at CMRP at the University of Wollongong.

List of References

- Aldosari, A. H., Espinoza, A., Robinson, D., Fuduli, I., Porumb, C., Alshaikh, S., Carolan, M., Lerch, M. L. F., Perevertaylo, V., Rosenfeld, A. B. and Petasecca, M. (2013) 'Characterization of an innovative p-type epitaxial diode for dosimetry in modern external beam radiotherapy', *IEEE Transactions on Nuclear Science*, 60(6), pp. 4705–4712. doi: 10.1109/TNS.2013.2289909.
- Aldosari, A. H., Petasecca, M., Espinoza, A., Newall, M., Fuduli, I., Porumb, C., Alshaikh, S., Alrowaili, Z. A., Weaver, M., Metcalfe, P., Carolan, M., Lerch, M. L. F., Perevertaylo, V. and Rosenfeld, A. B. (2014) 'A two dimensional silicon detectors array for quality assurance in stereotactic radiotherapy: MagicPlate-512', *Medical Physics*, 41(9), p. 091707. doi: 10.1118/1.4892384.
- Alnaghy, S. J., Causer, T., Roberts, N., Oborn, B., Jelen, U., Dong, B., Gargett, M., Begg, J., Liney, G., Petasecca, M., Rosenfeld, A. B., Holloway, L. and Metcalfe, P. (2020) 'High resolution silicon array detector implementation in an inline MRI-linac', *Medical Physics*, 47(4), pp. 1920–1929. doi: 10.1002/mp.14016.
- American Association of Physicists in Medicine Radiation Therapy Task Group 62 (2005) 'Diode in vivo dosimetry for patients receiving external beam radiation therapy', *Medical Physics Publishing*, pp. 1–84.
- Andreo, P., Burns, D. T., Hohlfield, K., Huq, M. S., Kanai, T., Laitano, F., Smyth, V. and Vynckier, S. (2006) 'Absorbed Dose Determination in External Beam Radiotherapy: An International Code of Practice for Dosimetry based on Standards of Absorbed Dose to Water', *IAEA Technical Reports Series no. 398*. Vienna: International Atomic Energy Agency.
- ArcCHECK® - Sun Nuclear* (2020). Available at: <https://www.sunnuclear.com/products/arccheck> (Accessed: 24 August 2020).
- Arjomandy, B., Taylor, P., Ainsley, C., Safai, S., Sahoo, N., Pankuch, M., Farr, J. B., Yong Park, S., Klein, E., Flanz, J., Yorke, E. D., Followill, D. and Kase, Y. (2019) 'AAPM task group 224: Comprehensive proton therapy machine quality assurance', *Medical Physics*, 46(8), pp. e678–e705. doi: 10.1002/mp.13622.
- Aspradakis, M. M., Byrne, J. P., Palmans, H., Duane, S., Conway, J., Warrington, A. P. and Rosser, K. (2010) 'IPEM Report 103: Small Field MV Photon Dosimetry', *International Atomic Energy Agency (IAEA)*.
- Ataei, G., Rezaei, M., Gorji, K., Banaei, A., Goushbolagh, N., Farhood, B., Bagheri, M. and Firouzjah, R. (2019) 'Evaluation of dose rate and photon energy dependence of gafchromic EBT3 film irradiating with 6 MV and Co-60 photon beams', *Journal of Medical Signals & Sensors*, 9(3), p. 204. doi: 10.4103/jmss.JMSS_45_18.
- Avevor, J., Tagoe, S. N. A., Amuasi, J. H., Fletcher, J. J. and Shirazu, I. (2017) 'Dose Assessment of the Rectum during Brachytherapy of the Cervix Using Gafchromic Films', *International Journal of Scientific Research in Science, Engineering and Technology*, 3(5), pp. 651–659.
- Berger, M. J., Coursey, J. S., Zucker, M. A. and Chang, J. (2017) 'Stopping-Power & Range Tables for Electrons, Protons, and Helium Ions', *Nistir*, 4999, pp. 1–17. doi: 10.18434/T4NC7P.
- Bertholet, J., Knopf, A., Eiben, B., McClelland, J., Grimwood, A., Harris, E., Menten, M., Poulsen, P., Nguyen, D. T., Keall, P. and Oelfke, U. (2019) 'Real-time intrafraction motion monitoring in external beam radiotherapy', *Physics in Medicine and Biology*, 64(15). doi: 10.1088/1361-6560/ab2ba8.
- Biasi, G., Petasecca, M., Guatelli, S., Hardcastle, N., Carolan, M., Perevertaylo, V., Kron, T. and Rosenfeld, A. B. (2018) 'A novel high-resolution 2D silicon array detector for small field dosimetry with FFF photon beams', *Physica Medica*. Elsevier, 45(October 2017), pp. 117–126. doi: 10.1016/j.ejmp.2017.12.010.

Booth, J. T., Caillet, V., Hardcastle, N., O'Brien, R., Szymura, K., Crasta, C., Harris, B., Haddad, C., Eade, T. and Keall, P. J. (2016) 'The first patient treatment of electromagnetic-guided real time adaptive radiotherapy using MLC tracking for lung SABR', *Radiotherapy and Oncology*, 121(1), pp. 19–25. doi: 10.1016/j.radonc.2016.08.025.

Borca, V. C., Pasquino, M., Russo, G., Grosso, P., Cante, D., Sciacero, P., Girelli, G., La Porta, M. R. and Tofani, S. (2013) 'Dosimetric characterization and use of GAFCHROMIC EBT3 film for IMRT dose verification', *Journal of Applied Clinical Medical Physics*, 14(2), pp. 158–171. doi: 10.1120/jacmp.v14i2.4111.

Bouchard, H., Seuntjens, J., Duane, S., Kamio, Y. and Palmans, H. (2015) 'Detector dose response in megavoltage small photon beams. I. Theoretical concepts', *Medical Physics*, 42(10), pp. 6033–6047. doi: 10.1118/1.4930053.

Bouchard, H., Kamio, Y., Palmans, H., Seuntjens, J. and Duane, S. (2015) 'Detector dose response in megavoltage small photon beams. II. Pencil beam perturbation effects', *Medical Physics*, 42(10), pp. 6048–6061. doi: 10.1118/1.4930798.

Brown, J. M., Carlson, D. J. and Brenner, D. J. (2014) 'The tumor radiobiology of SRS and SBRT: Are more than the 5 Rs involved?', *International Journal of Radiation Oncology Biology Physics*, 88(2), pp. 254–262. doi: 10.1016/j.ijrobp.2013.07.022.

Butson, M. J., Yu, P. K. N., Cheung, T. and Metcalfe, P. (2003) 'Radiochromic film for medical radiation dosimetry', *Materials Science and Engineering: R: Reports*, 41(3–5), pp. 61–120. doi: 10.1016/S0927-796X(03)00034-2.

Butson, M. J., Cheung, T. and Yu, P. K. N. (2006) 'Scanning orientation effects on Gafchromic EBT film dosimetry.', *Australasian Physical & Engineering Sciences in Medicine*, 29(3), pp. 281–284. doi: 10.1007/BF03178579.

Calypso | Varian (2020). Available at: <https://www.varian.com/en-au/products/radiotherapy/real-time-tracking-motion-management/calypso> (Accessed: 25 August 2020).

Cancer (2018). Available at: <https://www.who.int/en/news-room/fact-sheets/detail/cancer> (Accessed: 24 August 2020).

Cantone, M. C., Ciocca, M., Dionisi, F., Fossati, P., Lorentini, S., Krengli, M., Molinelli, S., Orecchia, R., Schwarz, M., Veronese, I. and Vitolo, V. (2013) 'Application of failure mode and effects analysis to treatment planning in scanned proton beam radiotherapy', *Radiation Oncology*, 8(1), pp. 1–9. doi: 10.1186/1748-717X-8-127.

Castriconi, R., Ciocca, M., Mirandola, A., Sini, C., Broggi, S., Schwarz, M., Fracchiolla, F., Martišíková, M., Aricò, G., Mettievier, G. and Russo, P. (2017) 'Dose-response of EBT3 radiochromic films to proton and carbon ion clinical beams', *Physics in Medicine and Biology*, 62(2), pp. 377–393. doi: 10.1088/1361-6560/aa5078.

Causser, T. J., Chapman, T., Oborn, B. M., Davis, J. A., Petasecca, M., Rosenfeld, A. B. and Metcalfe, P. (2019) 'Characterization of a high spatiotemporal resolution monolithic silicon strip detector for MRI-linac dosimetry', *Journal of Physics: Conference Series*, 1154(1). doi: 10.1088/1742-6596/1154/1/012006.

Causser, T. J., Schellhammer, S. M., Gantz, S., Lühr, A., Hoffmann, A. L., Metcalfe, P. E., Rosenfeld, A. B., Guatelli, S., Petasecca, M. and Oborn, B. M. (2020) 'First application of a high-resolution silicon detector for proton beam Bragg peak detection in a 0.95 T magnetic field', *Medical Physics*, 47(1), pp. 181–189. doi: 10.1002/mp.13871.

Charlie Ma, C.-M. (2019) 'Physics and Dosimetric Principles of SRS and SBRT', *Mathews Journal of Cancer Science*, 4(2), pp. 1–16. doi: 10.30654/mjcs.10022.

Chen, S. N., Gauthier, M., Bazalova-Carter, M., Bolanos, S., Glenzer, S., Riquier, R., Revet, G., Antici, P., Morabito, A., Propp, A., Starodubtsev, M. and Fuchs, J. (2016) 'Absolute dosimetric characterization of

Gafchromic EBT3 and HDv2 films using commercial flat-bed scanners and evaluation of the scanner response function variability', *Review of Scientific Instruments*, 87(7). doi: 10.1063/1.4954921.

Ciancaglioni, I., Marinelli, M., Milani, E., Prestopino, G., Verona, C., Verona-Rinati, G., Consorti, R., Petrucci, A. and De Notaristefani, F. (2012) 'Dosimetric characterization of a synthetic single crystal diamond detector in clinical radiation therapy small photon beams', *Medical Physics*, 39(7), pp. 4493–4501. doi: 10.1118/1.4729739.

Das, I. J., Ding, G. X. and Ahnesjö, A. (2008) 'Small fields: Nonequilibrium radiation dosimetry', *Medical Physics*, pp. 206–215. doi: 10.1118/1.2815356.

Debrot, E., Newall, M., Guatelli, S., Petasecca, M., Matsufuji, N. and Rosenfeld, A. B. (2018) 'A silicon strip detector array for energy verification and quality assurance in heavy ion therapy', *Medical Physics*, 45(2), pp. 953–962. doi: 10.1002/mp.12736.

DeLaney, T. F. (2007) 'Clinical proton radiation therapy research at the Francis H. Burr Proton Therapy Center', *Technology in Cancer Research and Treatment*, 6(4 Suppl), pp. 61–66. doi: 10.1177/15330346070060s410.

Depuydt, T., Verellen, D., Haas, O., Gevaert, T., Linthout, N., Duchateau, M., Tournel, K., Reynders, T., Leysen, K., Hoogeman, M., Storme, G. and Ridder, M. De (2011) 'Geometric accuracy of a novel gimbals based radiation therapy tumor tracking system', *Radiotherapy and Oncology*, 98(3), pp. 365–372. doi: 10.1016/j.radonc.2011.01.015.

Devic, S., Tomic, N. and Lewis, D. (2016) 'Reference radiochromic film dosimetry: Review of technical aspects', *Physica Medica*, 32(4), pp. 541–556. doi: 10.1016/j.ejmp.2016.02.008.

Dhanesar, S., Sahoo, N., Kerr, M., Taylor, M. B., Summers, P., Zhu, X. R., Poenisch, F. and Gillin, M. (2013) 'Quality assurance of proton beams using a multilayer ionization chamber system', *Medical Physics*, 40(9). doi: 10.1118/1.4817481.

Elith, C., Dempsey, S. E., Findlay, N. and Warren-Forward, H. M. (2011) 'An introduction to the intensity-modulated radiation therapy (IMRT) techniques, tomotherapy, and VMAT', *Journal of Medical Imaging and Radiation Sciences*, 42(1), pp. 37–43. doi: 10.1016/j.jmir.2010.11.005.

Fuduli, I., Porumb, C., Espinoza, A. A., Aldosari, A. H., Carolan, M., Lerch, M. L. F., Metcalfe, P., Rosenfeld, A. B. and Petasecca, M. (2014) 'A comparative analysis of multichannel Data Acquisition Systems for quality assurance in external beam radiation therapy', *Journal of Instrumentation*, 9(6). doi: 10.1088/1748-0221/9/06/T06003.

Fuduli, I., Newall, M. K., Espinoza, A. A., Porumb, C. S., Carolan, M., Lerch, M. L. F., Metcalfe, P., Rosenfeld, A. B. and Petasecca, M. (2014) 'Multichannel Data Acquisition System comparison for Quality Assurance in external beam radiation therapy', in *Radiation Measurements*, pp. 338–341. doi: 10.1016/j.radmeas.2014.05.016.

Galvin, J. M. and De Neve, W. (2007) 'Intensity modulating and other radiation therapy devices for dose painting', *Journal of Clinical Oncology*, 25(8), pp. 924–930. doi: 10.1200/JCO.2007.10.6716.

Green, O. L., Rankine, L. J., Cai, B., Curcuru, A., Kashani, R., Rodriguez, V., Li, H. H., Parikh, P. J., Robinson, C. G., Olsen, J. R., Mutic, S., Goddu, S. M. and Santanam, L. (2018) 'First clinical implementation of real-time, real anatomy tracking and radiation beam control', *Medical Physics*, 45(8), pp. 3728–3740. doi: 10.1002/mp.13002.

Hall, E. J. and Wu, C. S. (2003) 'Radiation-induced second cancers: The impact of 3D-CRT and IMRT', *International Journal of Radiation Oncology Biology Physics*, 56(1), pp. 83–88. doi: 10.1016/S0360-3016(03)00073-7.

Hanna, G. G. and Landau, D. (2015) 'Stereotactic body radiotherapy for oligometastatic disease', *Clinical Oncology*, 27(5), pp. 290–297. doi: 10.1016/j.clon.2015.02.003.

- Heinzerling, J. H., Hampton, C. J., Robinson, M., Bright, M., Moeller, B. J., Ruiz, J., Prabhu, R., Burri, S. H. and Foster, R. D. (2020) ‘Use of surface-guided radiation therapy in combination with IGRT for setup and intrafraction motion monitoring during stereotactic body radiation therapy treatments of the lung and abdomen’, *Journal of Applied Clinical Medical Physics*, 21(5), pp. 48–55. doi: 10.1002/acm2.12852.
- Henke, L., Kashani, R., Robinson, C., Curcuru, A., DeWees, T., Bradley, J., Green, O., Michalski, J., Mutic, S., Parikh, P. and Olsen, J. (2018) ‘Phase I trial of stereotactic MR-guided online adaptive radiation therapy (SMART) for the treatment of oligometastatic or unresectable primary malignancies of the abdomen’, *Radiotherapy and Oncology*, 126(3), pp. 519–526. doi: 10.1016/j.radonc.2017.11.032.
- Heydariyan, M., Hoban, P. W. and Beddoe, A. H. (1996) ‘A comparison of dosimetry techniques in stereotactic radiosurgery’, *Physics in Medicine and Biology*, 41(1), pp. 93–110. doi: 10.1088/0031-9155/41/1/008.
- Hoban, P. W., Heydariyan, M., Beckham, W. A. and Beddoe, A. H. (1994) ‘Dose rate dependence of a PTW diamond detector in the dosimetry of a 6 MV photon beam’, *Physics in Medicine and Biology*, 39(8), pp. 1219–1229. doi: 10.1088/0031-9155/39/8/003.
- Huet, C., Moignier, C., Fontaine, J. and Clairand, I. (2014) ‘Characterization of the gafchromic EBT3 films for dose distribution measurements in stereotactic radiotherapy’, *Radiation Measurements*, 71, pp. 364–368. doi: 10.1016/j.radmeas.2014.05.020.
- Ishikawa, H., Tsuji, H., Murayama, S., Sugimoto, M., Shinohara, N., Maruyama, S., Murakami, M., Shirato, H. and Sakurai, H. (2019) ‘Particle therapy for prostate cancer: The past, present and future’, *International Journal of Urology*, 26(10), pp. 971–979. doi: 10.1111/iju.14041.
- Jursinic, P. A. (2009) ‘Angular dependence of dose sensitivity of surface diodes’, *Medical Physics*, 36(6), pp. 2165–2171. doi: 10.1118/1.3125644.
- Kavanagh, B. D., McGarry, R. C. and Timmerman, R. D. (2006) ‘Extracranial radiosurgery (stereotactic body radiation therapy) for oligometastases.’, *Seminars in radiation oncology*, 16(2), pp. 77–84. doi: 10.1016/j.semradonc.2005.12.003.
- Keall, P., Nguyen, D. T., O’Brien, R., Hewson, E., Ball, H., Poulsen, P., Booth, J., Greer, P., Hunter, P., Wilton, L., Bromley, R., Kipritidis, J., Eade, T., Kneebone, A., Hruby, G., Moodie, T., Hayden, A., Turner, S., Arumugam, S., *et al.* (2020) ‘Real-Time Image Guided Ablative Prostate Cancer Radiation Therapy: Results From the TROG 15.01 SPARK Trial’, *International Journal of Radiation Oncology Biology Physics*, 107(3), pp. 530–538. doi: 10.1016/j.ijrobp.2020.03.014.
- Keall, P. J., Colvill, E., O’Brien, R., Ng, J. A., Poulsen, P. R., Eade, T., Kneebone, A. and Booth, J. T. (2014) ‘The first clinical implementation of electromagnetic transponder-guided MLC tracking’, *Medical Physics*, 41(2), p. 020702. doi: 10.1118/1.4862509.
- Knopf, A. C. and Lomax, A. (2013) ‘In vivo proton range verification: A review’, *Physics in Medicine and Biology*, 58(15), pp. 131–160. doi: 10.1088/0031-9155/58/15/R131.
- Kron, T. (1994) ‘Thermoluminescence dosimetry and its applications in medicine--Part 1: Physics, materials and equipment.’, *Australasian physical & engineering sciences in medicine*, 17(4), pp. 175–199.
- Kron, T. (1995) ‘Thermoluminescence dosimetry and its applications in medicine--Part 2: History and applications.’, *Australasian physical & engineering sciences in medicine*, 18(1), pp. 1–25. doi: 10.1007/13246.1879-5447.
- Kry, S. F., Alvarez, P., Cygler, J. E., DeWerd, L. A., Howell, R. M., Meeks, S., O’Daniel, J., Reft, C., Sawakuchi, G., Yukihiro, E. G. and Mihailidis, D. (2020) ‘AAPM TG 191: Clinical use of luminescent dosimeters: TLDs and OSLDs’, *Medical Physics*, 47(2), pp. e19–e51. doi: 10.1002/mp.13839.
- Kubo, H. D. and Hill, B. C. (1996) ‘Respiration gated radiotherapy treatment: A technical study’, *Physics in Medicine and Biology*, 41(1), pp. 83–91. doi: 10.1088/0031-9155/41/1/007.

- Lang, S., Zeimet, J., Ochsner, G., Schmid Daners, M., Riesterer, O. and Klöck, S. (2014) ‘Development and evaluation of a prototype tracking system using the treatment couch’, *Medical Physics*, 41(2), p. 021720. doi: 10.1118/1.4862077.
- Laub, W. U. and Crilly, R. (2014) ‘Clinical radiation therapy measurements with a new commercial synthetic single crystal diamond detector’, *Journal of Applied Clinical Medical Physics*, 15(6), pp. 92–102. doi: 10.1120/jacmp.v15i6.4890.
- Lee, N. Y. and Terezakis, S. A. (2008) ‘Intensity-modulated radiation therapy’, *Journal of Surgical Oncology*, 97(8), pp. 691–696. doi: 10.1002/jso.21014.
- León-Marroquín, E. Y., Camacho-López, M. A., García-Garduño, O. A., Herrera-González, J. A., Villarreal-Barajas, J. E., Gutiérrez-Fuentes, R. and Contreras-Bulnes, R. (2016) ‘Spectral analysis of the EBT3 radiochromic film irradiated with 6 MV X-ray radiation’, *Radiation Measurements*, 89, pp. 82–88. doi: 10.1016/j.radmeas.2016.03.007.
- Lewis, D. F. and Chan, M. F. (2016) ‘Technical Note: On GAFChromic EBT-XD film and the lateral response artifact’, *Medical Physics*, 43(2), pp. 643–649. doi: 10.1118/1.4939226.
- Low, D. A., Harms, W. B., Mutic, S. and Purdy, J. A. (1998) ‘A technique for the quantitative evaluation of dose distributions’, *Medical Physics*, 25(5), pp. 656–661. doi: 10.1118/1.598248.
- Low, D. A., Moran, J. M., Dempsey, J. F., Dong, L. and Oldham, M. (2011) ‘Dosimetry tools and techniques for IMRT’, *Medical Physics*, 38(3), pp. 1313–1338. doi: 10.1118/1.3514120.
- Low, D. A. and Dempsey, J. F. (2003) ‘Evaluation of the gamma dose distribution comparison method’, *Medical Physics*, 30(9), pp. 2455–2464. doi: 10.1118/1.1598711.
- Lühr, A., von Neubeck, C., Krause, M. and Troost, E. G. C. (2018) ‘Relative biological effectiveness in proton beam therapy – Current knowledge and future challenges’, *Clinical and Translational Radiation Oncology*, 9, pp. 35–41. doi: 10.1016/j.ctro.2018.01.006.
- MapCHECK® 3 - Sun Nuclear* (2020). Available at: <https://www.sunnuclear.com/products/mapcheck-3> (Accessed: 24 August 2020).
- Marroquin, E. Y. L., Herrera González, J. A., Camacho López, M. A., Barajas, J. E. V. and García-Garduño, O. A. (2016) ‘Evaluation of the uncertainty in an EBT3 film dosimetry system utilizing net optical density’, *Journal of Applied Clinical Medical Physics*, 17(5), pp. 466–481. doi: 10.1120/jacmp.v17i5.6262.
- MatriXX - Universal Detector Array | IBA Dosimetry* (2020). Available at: <https://www.ibadosimetry.com/product/matrixx-universal-detector-array/> (Accessed: 24 August 2020).
- Mayles, P., Nahum, A. and Rosenwald, J. C. (2007) *Handbook of radiotherapy physics: Theory and practice, Handbook of Radiotherapy Physics: Theory and Practice*. CRC Press. doi: 10.1118/1.2969650.
- Merchant, A. H., Newall, M., Guatelli, S., Petasecca, M., Lerch, M., Perevertaylo, V., Milluzzo, G., Petringa, G., Romano, F., Cirrone, G. A. P., Cuttone, G., Jackson, M. and Rosenfeld, A. B. (2017) ‘Feasibility study of a novel multi-strip silicon detector for use in proton therapy range verification quality assurance’, *Radiation Measurements*, 106, pp. 378–384. doi: 10.1016/j.radmeas.2017.03.017.
- Miften, M., Olch, A., Mihailidis, D., Moran, J., Pawlicki, T., Molineu, A., Li, H., Wijesooriya, K., Shi, J., Xia, P., Papanikolaou, N. and Low, D. A. (2018) ‘Tolerance limits and methodologies for IMRT measurement-based verification QA: Recommendations of AAPM Task Group No. 218’, *Medical Physics*, 45(4), pp. e53–e83. doi: 10.1002/mp.12810.
- Min, C. H., Kim, C. H., Youn, M. Y. and Kim, J. W. (2006) ‘Prompt gamma measurements for locating the dose falloff region in the proton therapy’, *Applied Physics Letters*, 89(18), pp. 9–12. doi: 10.1063/1.2378561.
- Mirandola, A., Magro, G., Lavagno, M., Mairani, A., Molinelli, S., Russo, S., Mastella, E., Vai, A., Maestri,

D., La Rosa, V. and Ciocca, M. (2018) 'Characterization of a multilayer ionization chamber prototype for fast verification of relative depth ionization curves and spread-out-Bragg-peaks in light ion beam therapy', *Medical Physics*, 45(5), pp. 2266–2277. doi: 10.1002/mp.12866.

Morimoto, K., Demizu, Y., Hashimoto, N., Mima, M., Terashima, K., Fujii, O., Otsuki, N., Murakami, M., Fuwa, N. and Nibu, K. I. (2014) 'Particle radiotherapy using protons or carbon ions for unresectable locally advanced head and neck cancers with skull base invasion', *Japanese Journal of Clinical Oncology*, 44(5), pp. 428–434. doi: 10.1093/jjco/hyu010.

Ng, J. A., Booth, J. T., Poulsen, P. R., Fledelius, W., Worm, E. S., Eade, T., Hegi, F., Kneebone, A., Kuncic, Z. and Keall, P. J. (2012) 'Kilovoltage Intrafraction Monitoring for Prostate Intensity Modulated Arc Therapy: First Clinical Results', *International Journal of Radiation Oncology*Biophysics*Physics*, 84(5), pp. e655–e661. doi: 10.1016/j.ijrobp.2012.07.2367.

Niroomand-Rad, A., Blackwell, C. R., Coursey, B. M., Gall, K. P., Galvin, J. M., McLaughlin, W. L., Meigooni, A. S., Nath, R., Rodgers, J. E. and Soares, C. G. (1998) 'Radiochromic film dosimetry: Recommendations of AAPM Radiation Therapy Committee Task Group 55', *Medical Physics*, 25(11), pp. 2093–2115. doi: 10.1118/1.598407.

OCTAVIUS 4D - PTW Freiburg GmbH (2020). Available at: <https://www.ptwdosimetry.com/en/products/octavius-4d/> (Accessed: 24 August 2020).

OCTAVIUS Detector 1600 SRS - PTW Freiburg GmbH (2020). Available at: <https://www.ptwdosimetry.com/en/products/octavius-detector-1600-srs/> (Accessed: 24 August 2020).

Oppenheim, A. V., Schaffer, R. W. and Buck, J. R. (1999) 'Discrete-Time Signal Processing', *Book*. 2nd edn. Upper Saddle River, New Jersey: Prentice-Hall, Inc, p. 870.

Paganetti, H. (2012) 'Range uncertainties in proton therapy and the role of Monte Carlo simulations', *Physics in Medicine and Biology*, 57(11). doi: 10.1088/0031-9155/57/11/R99.

Palmans, H., Andreo, P., Huq, M., Seuntjens, J. and Christaki, K. (2017) 'Dosimetry of Small Static Fields used in External Beam Radiotherapy: An IAEA–AAPM International Code of Practice for Reference and Relative Dose Determination', *Technical Report Series No. 483*. Vienna: International Atomic Energy Agency.

Palmans, H., Andreo, P., Huq, M. S., Seuntjens, J., Christaki, K. E. and Meghzifene, A. (2018) 'Dosimetry of small static fields used in external photon beam radiotherapy: Summary of TRS-483, the IAEA–AAPM international Code of Practice for reference and relative dose determination', *Medical Physics*, 45(11), pp. 1138–1138. doi: 10.1002/mp.13208.

Papaconstadopoulos, P., Hegyi, G., Seuntjens, J. and Devic, S. (2014) 'A protocol for EBT3 radiochromic film dosimetry using reflection scanning', *Medical Physics*, 41(12). doi: 10.1118/1.4901308.

Pappas, E., Maris, T. G., Zacharopoulou, F., Papadakis, A., Manolopoulos, S., Green, S. and Wojnecki, C. (2008) 'Small SRS photon field profile dosimetry performed using a PinPoint air ion chamber, a diamond detector, a novel silicon-diode array (DOSI), and polymer gel dosimetry. Analysis and intercomparison', *Medical Physics*, 35(10), pp. 4640–4648. doi: 10.1118/1.2977829.

Parodi, K., Paganetti, H., Shih, H. A., Michaud, S., Loeffler, J. S., DeLaney, T. F., Liebsch, N. J., Munzenrider, J. E., Fischman, A. J., Knopf, A. and Bortfeld, T. (2007) 'Patient Study of In Vivo Verification of Beam Delivery and Range, Using Positron Emission Tomography and Computed Tomography Imaging After Proton Therapy', *International Journal of Radiation Oncology Biology Physics*, 68(3), pp. 920–934. doi: 10.1016/j.ijrobp.2007.01.063.

Petasecca, M., Alhujaili, S., Aldosari, a. H., Fuduli, I., Newall, M., Porumb, C. S., Carolan, M., Nitschke, K., Lerch, M. L. F., Kalliopuska, J., Perevertaylo, V. and Rosenfeld, A. B. (2015) 'Angular independent silicon detector for dosimetry in external beam radiotherapy', *Medical Physics*, 42(8), pp. 4708–4718. doi: 10.1118/1.4926778.

Planskoy, B. (1980) 'Evaluation of diamond radiation dosimeters', *Physics in Medicine and Biology*, 25(3), pp. 519–532. doi: 10.1088/0031-9155/25/3/011.

Products (2020). Available at: <https://delta4family.com/products#phantom> (Accessed: 24 August 2020).

Purdy, J. A. (2008) 'Dose to normal tissues outside the radiation therapy patient's treated volume: A review of different radiation therapy techniques', *Health Physics*, 95(5), pp. 666–676. doi: 10.1097/01.HP.0000326342.47348.06.

Radiotherapy Films - GAFchromic™ (2020). Available at: <http://www.gafchromic.com/gafchromic-film/radiotherapy-films/index.asp> (Accessed: 25 August 2020).

Rosenfeld, A. B., Biasi, G., Petasecca, M., Lerch, M. L. F., Villani, G. and Feygelman, V. (2020) 'Semiconductor dosimetry in modern external-beam radiation therapy', *Physics in Medicine & Biology*, 65(16), p. 16TR01. doi: 10.1088/1361-6560/aba163.

Ruan, D. and Keall, P. (2010) 'Online prediction of respiratory motion: multidimensional processing with low-dimensional feature learning', *Physics in Medicine and Biology*, 55(11), pp. 3011–3025. doi: 10.1088/0031-9155/55/11/002.

Rubio, C., Morera, R., Hernando, O., Leroy, T. and Lartigau, S. E. (2013) 'Extracranial stereotactic body radiotherapy. Review of main SBRT features and indications in primary tumors', *Reports of Practical Oncology and Radiotherapy*. Wielkopolskie Centrum Onkologii, pp. 387–396. doi: 10.1016/j.rpor.2013.09.009.

Rutherford, H., Chacon, A., Mohammadi, A., Takyu, S., Tashima, H., Yoshida, E., Nishikido, F., Hofmann, T., Pinto, M., Franklin, D. R., Yamaya, T., Parodi, K., Rosenfeld, A. B., Guatelli, S. and Safavi-Naeini, M. (2020) 'Dose quantification in carbon ion therapy using in-beam positron emission tomography', *Physics in Medicine & Biology*, (July). doi: 10.1088/1361-6560/abaa23.

Sadeghi, M., Sina, S. and Faghihi, R. (2015) 'Investigation of LiF, Mg and Ti (TLD-100) reproducibility', *Journal of Biomedical Physics and Engineering*, 5(4), pp. 217–222. doi: 10.22086/jbpe.v5i4.

Saini, J., Cao, N., Bowen, S. R., Herrera, M., Nicewonger, D., Wong, T. and Bloch, C. D. (2016) 'Clinical Commissioning of a Pencil Beam Scanning Treatment Planning System for Proton Therapy', *International Journal of Particle Therapy*, 3(1), pp. 51–60. doi: 10.14338/ijpt-16-0000.1.

Schulz-Ertner, D. and Tsujii, H. (2007) 'Particle radiation therapy using proton and heavier ion beams', *Journal of Clinical Oncology*, 25(8), pp. 953–964. doi: 10.1200/JCO.2006.09.7816.

Shah, A. P., Kupelian, P. a, Willoughby, T. R. and Meeks, S. L. (2011) 'Expanding the use of real-time electromagnetic tracking in radiation oncology', *Journal of Applied Clinical Medical Physics*, 12(4), pp. 34–49. doi: 10.1120/jacmp.v12i4.3590.

Sheehan, J. P., Yen, C. P., Lee, C. C. and Loeffler, J. S. (2014) 'Cranial stereotactic radiosurgery: Current status of the initial paradigm shifter', *Journal of Clinical Oncology*, 32(26), pp. 2836–2846. doi: 10.1200/JCO.2013.53.7365.

Shi, J., Simon, W. E. and Zhu, T. C. (2003) 'Modeling the instantaneous dose rate dependence of radiation diode detectors', *Medical Physics*, 30(9), pp. 2509–2519. doi: 10.1118/1.1602171.

Shioyama, Y., Tsuji, H., Suefuji, H., Sinoto, M., Matsunobu, A., Toyama, S., Nakamura, K. and Kudo, S. (2015) 'Particle radiotherapy for prostate cancer', *International Journal of Urology*, 22(1), pp. 33–39. doi: 10.1111/iju.12640.

Shirato, H., Seppenwoolde, Y., Kitamura, K., Onimura, R. and Shimizu, S. (2004) 'Intrafractional Tumor Motion: Lung and Liver', *Seminars in Radiation Oncology*, 14(1), pp. 10–18. doi: 10.1053/j.semradonc.2003.10.008.

Al Shukaili, K., Petasecca, M., Newall, M., Espinoza, A., Perevertaylo, V. L., Corde, S., Lerch, M. L. F.

and Rosenfeld, A. B. (2017) 'A 2D silicon detector array for quality assurance in small field dosimetry: DUO', *Medical Physics*, 44(2), pp. 628–636. doi: 10.1002/mp.12060.

Solid Water® HE (Gammex™ Technology) - Sun Nuclear (2020). Available at: <https://www.sunnuclear.com/products/solid-water-he> (Accessed: 24 August 2020).

Sorriaux, J., Kacperek, A., Rossomme, S., Lee, J. A., Bertrand, D., Vynckier, S. and Sterpin, E. (2013) 'Evaluation of Gafchromic® EBT3 films characteristics in therapy photon, electron and proton beams', *Physica Medica*, 29(6), pp. 599–606. doi: 10.1016/j.ejmp.2012.10.001.

SRS MapCHECK® - Sun Nuclear (2020). Available at: <https://www.sunnuclear.com/products/srs-mapcheck> (Accessed: 24 August 2020).

Stansook, N., Biasi, G., Utitsarn, K., Petasecca, M., Metcalfe, P., Carolan, M., Lerch, M. L. F., Perevertaylo, V. L., Kron, T. and Rosenfeld, A. B. (2019) '2D monolithic silicon-diode array detectors in megavoltage photon beams: does the fabrication technology matter? A medical physicist's perspective', *Australasian Physical and Engineering Sciences in Medicine*. Springer International Publishing, 42(2), pp. 443–451. doi: 10.1007/s13246-019-00736-7.

Tran, L. T., Chartier, L., Bolst, D., Pogosso, A., Guatelli, S., Petasecca, M., Lerch, M. L. F., Prokopovich, D. A., Reinhard, M. I., Clasio, B., Depauw, N., Kooy, H., Flanz, J. B., McNamara, A., Paganetti, H., Beltran, C., Furutani, K., Perevertaylo, V. L., Jackson, M., *et al.* (2017) 'Characterization of proton pencil beam scanning and passive beam using a high spatial resolution solid-state microdosimeter', *Medical Physics*, 44(11), pp. 6085–6095. doi: 10.1002/mp.12563.

Trikalinos, T. A., Terasawa, T., Ip, S., Raman, G. and Lau, J. (2009) 'Particle Beam Radiation Therapies for Cancer. Technical Brief No. 1.', *Prepared by Tufts Medical Center Evidence-based Practice Center under Contract No. HHS-290-07-10055*. Rockville, MD: Agency for Healthcare Research and Quality.

Tsujii, H. and Kamada, T. (2012) 'A review of update clinical results of carbon ion radiotherapy', *Japanese Journal of Clinical Oncology*, 42(8), pp. 670–685. doi: 10.1093/jjco/hys104.

Tyler, M., Liu, P. Z. Y., Chan, K. W., Ralston, A., McKenzie, D. R., Downes, S. and Suchowerska, N. (2013) 'Characterization of small-field stereotactic radiosurgery beams with modern detectors', *Physics in Medicine and Biology*, 58(21), pp. 7595–7608. doi: 10.1088/0031-9155/58/21/7595.

Types of Cancer Treatment - National Cancer Institute (2020). Available at: <https://www.cancer.gov/about-cancer/treatment/types> (Accessed: 24 August 2020).

Vatnitsky, S. and Jarvinen, H. (1993) 'Application of a natural diamond detector for the measurement of relative dose distributions in radiotherapy', *Physics in Medicine and Biology*, 38(1), pp. 173–184. doi: 10.1088/0031-9155/38/1/013.

Veselsky, T., Novotny, J. and Pastykova, V. (2018) 'Assessment of basic physical and dosimetric parameters of synthetic single-crystal diamond detector and its use in Leksell Gamma Knife and CyberKnife small radiosurgical fields', *International Journal of Radiation Research*, 16(1), pp. 7–16. doi: 10.18869/acadpub.ijrr.16.1.7.

Webb, S. (2003) 'The physical basis of IMRT and inverse planning', *British Journal of Radiology*, 76(910), pp. 678–689. doi: 10.1259/bjr/65676879.

Welsh, K. T. and Reinstein, L. E. (2001) 'The thermal characteristics of different diodes on in vivo patient dosimetry', *Medical Physics*, 28(5), pp. 844–849. doi: 10.1118/1.1367862.

What is cancer? | Cancer Australia (2020). Available at: <https://www.canceraustralia.gov.au/affected-cancer/what-cancer> (Accessed: 24 August 2020).

What is Radiation Therapy? - Targeting Cancer (2020). Available at: <https://www.targetingcancer.com.au/what-is-radiation-therapy/> (Accessed: 24 August 2020).

What Is Radiotherapy? Benefits & Side Effects - TROG Cancer Research (2020). Available at: <https://www.trog.com.au/What-is-radiotherapy> (Accessed: 24 August 2020).

Wong, J. H. D., Carolan, M., Lerch, M. L. F., Petasecca, M., Khanna, S., Perevertaylo, V. L., Metcalfe, P. and Rosenfeld, A. B. (2010) 'A silicon strip detector dose magnifying glass for IMRT dosimetry', *Medical Physics*, 37(2), pp. 427–439. doi: 10.1118/1.3264176.

Wong, J. H. D., Hardcastle, N., Tom, W. A., Bayliss, A., Tolakanahalli, R., Lerch, M. L. F., Petasecca, M., Carolan, M., Metcalfe, P. and Rosenfeld, A. B. (2011) 'Independent quality assurance of a helical tomotherapy machine using the dose magnifying glass', *Medical Physics*, 38(4), pp. 2256–2264. doi: 10.1118/1.3566067.

Wong, J. H. D., Knittel, T., Downes, S., Carolan, M., Lerch, M. L. F., Petasecca, M., Perevertaylo, V. L., Metcalfe, P., Jackson, M. and Rosenfeld, A. B. (2011) 'The use of a silicon strip detector dose magnifying glass in stereotactic radiotherapy QA and dosimetry', *Medical Physics*, 38(3), pp. 1226–1238. doi: 10.1118/1.3549759.

Wuerfel, J. U. (2013) 'Dose measurements in small fields', *Medical Physics*, 1(1), pp. 81–90.

X-Ray Mass Attenuation Coefficients / NIST (2020). Available at: <https://www.nist.gov/pml/x-ray-mass-attenuation-coefficients> (Accessed: 24 August 2020).

Yajima, K., Kanai, T., Kusano, Y. and Shimojyu, T. (2009) 'Development of a multi-layer ionization chamber for heavy-ion radiotherapy', *Physics in Medicine and Biology*, 54(7). doi: 10.1088/0031-9155/54/7/N04.

Zarifi, M., Guatelli, S., Bolst, D., Hutton, B., Rosenfeld, A. and Qi, Y. (2017) 'Characterization of prompt gamma-ray emission with respect to the Bragg peak for proton beam range verification: A Monte Carlo study', *Physica Medica*, 33, pp. 197–206. doi: 10.1016/j.ejmp.2016.12.011.

Zebra - Scan monolayer & SOBP measurements / IBA Dosimetry (2020). Available at: <https://www.iba-dosimetry.com/product/zebra/> (Accessed: 25 August 2020).

Zenklusen, S. M., Pedroni, E. and Meer, D. (2010) 'A study on repainting strategies for treating moderately moving targets with proton pencil beam scanning at the new gantry 2 at PSI', *Physics in Medicine and Biology*, 55(17), pp. 5103–5121. doi: 10.1088/0031-9155/55/17/014.

Ziegler, J. F., Biersack, J. P. and Ziegler, M. D. (2013) *The Stopping and Range of Ions in Matter*. United Kingdom: Elsevier Science.

Ziegler, J. F., Ziegler, M. D. and Biersack, J. P. (2010) 'SRIM - The stopping and range of ions in matter (2010)', *Nuclear Instruments and Methods in Physics Research, Section B: Beam Interactions with Materials and Atoms*, 268(11–12), pp. 1818–1823. doi: 10.1016/j.nimb.2010.02.091.

Zou, W., Betancourt, R., Yin, L., Metz, J., Avery, S. and Kassaei, A. (2013) 'Effects on the photon beam from an electromagnetic array used for patient localization and tumor tracking', *Journal of Applied Clinical Medical Physics*, 14(3), pp. 72–80. doi: 10.1120/jacmp.v14i3.4138.

Appendices

Appendix A

A. MATLAB scripts

The following scripts were generated in MATLAB for data analysis of decoded detector acquisition files.

A.1. FindGamma.m

```
function [ Gamma ] = FindGamma( Measurement, Comparison )
% 20/05/2016

%Find Gamma value between two matrices

% Measurement - LOW Resolution Detector i.e. MagicPlate
% Comparison - HIGH Resolution Film

% The GAMMA answer will possess same dimensions as the measurement
matrix.

%This function/methodology does not work in the other direction, in
terms
%of matrix dimensions...

% Author: Matthew Newall
% Date: 6/10/12

%%
pitchMeasurement = 2.54/75; %define in cm.
pitchComparison = 0.1; %define in cm.

displacement = 0;

DistanceToAgreement = 0.2; %Distance to Agreement criterion (cm)
DoseDifference = 0.02; %Percentage dose difference criterion %
(decimal)

maxMeasurement = max(max(Measurement));
```

```

sizeMeasurement = size(Measurement);
sizeComparison = size(Comparison);

TempGamma = zeros(sizeComparison(1),sizeComparison(2));
Gamma = zeros(sizeMeasurement(1),sizeMeasurement(2));

%%
%if sizeMeasurement == sizeComparison
    for My = 1:sizeMeasurement(1)
        for Mx = 1:sizeMeasurement(2)
            for Cy = 1:sizeComparison(1)
                for Cx = 1:sizeComparison(2)
                    dr = (((Mx*pitchMeasurement)-
(Cx*pitchComparison))^2)+(((My*pitchMeasurement)-
(Cy*pitchComparison))^2)/(DistanceToAgreement^2);
                    dD = ((Measurement(My,Mx) -
Comparison(Cy,Cx))^2)/((DoseDifference.*maxMeasurement)^2);
                    TempGamma(Cy,Cx) = dr + dD;
                end
            end
            Gamma(My,Mx) = min(min(TempGamma));
        end
    end
    Gamma = sqrt(Gamma);
%else
%   fprintf('Matrix sizes do not agree.\n') ;
%end

%%

T = size(Gamma,1)*size(Gamma,2);
u = reshape(Gamma, T, 1);
a=0;
for i=1:T
    if u(i,*)>1
        a = a+1;
    end
end

A = (1-(a/T))*100;

fprintf('\n\tThe number of channels failing is %d out of %d', a, T);
fprintf('\n\tThe agreement across the array is %0.2f\n', A);

end

```

A.2. FindX.m

```

function [X] = findX(InputArray, Yvalue, isSDMG, showPlots)
% findX - this function determines the x-axis location of a single y-
axis
% normalised value along a gaussian distribution (i.e. beam profile)
via
% interpolation; using the 'piecewise cubic hermite interpolation
% polynomial ('pchipinterp').
%
%   A is a two column array; the first column consists of the x-axis
%   coordinates (in cm), the second column contains the y-axis
coordinates.
%

```

```

% Yvalue is the y-axis value (whose location is of interest) as a
% percentage of the maximum value in the profile, expressed as a
decimal
% e.g. 0.5 to find the "exact" location of the Half Maximums.
%
% Returns an array, X, containing the x-axis locations of the y-axis
% values for the Left Hand Side (LHS) and Right Hand Side (RHS) of
the
% distribution (about the central maximum).
%
% Nb: The columns MUST be of equal lengths and contain ONLY real
numbers.
%% DETERMINE ACTIONS BASED UPON NUMBER OF INPUTS.

if nargin == 2
    isSDMG = 0;
    showPlots = false;
elseif nargin == 3
    showPlots = false;
end

%% HIDDEN PARAMETERS.

% InputArray(:,1) = XinputVector;
% InputArray(:,2) = YinputVector;

useMaximumOfProfile = 0; % 0 -> No, 1-> Yes.

%% sDMG ONLY - Interpolate across gap between DMG's to find 'true'
maximum.
if isSDMG == 1
    %% COMPLETE THE ARRAY.
    ArrayToFit = InputArray;

    % Identify outliers (dead channels) to remove based upon 'n' and
'sigma' values.
    n = 8;
    sigma = 1.5;
    [~,I] = hampel(ArrayToFit(:,2),n,sigma);
    ArrayToFit(I,:) = [];

    % Plot outlier identification.
    if showPlots == true
        figure;
        subplot(1,2,1);
        title('Determine Outliers in Data');
        scatter(InputArray(:,1),...
            InputArray(:,2),...
            40,...
            'MarkerFaceColor',[0 0 .8]);
        box on
        xlabel('Distance (cm)');
        ylabel('Response (counts)');
        hold on
        plot(InputArray(I,1),InputArray(I,2),'sk','MarkerSize',10);
        hold off
        legend('Input Data','Identified Outliers');
        axis([0 InputArray(end,1) 0 max(ArrayToFit(:,2))*1.2]);
    end
end

```



```

    % Cut away known dead channels (unnecessary if filtering with
    hampel).
    % ArrayToFit(130:134,:) = []; % Cut dead channels for better
    fitting.

    % Spline or Pchip fitting: pchip fitting provides 'flatter'/lower
    maximum -> broader FWHM.
    %     FitOfProfile =
    fit(ArrayToFit(:,1),ArrayToFit(:,2),'smoothingspline','SmoothingParam'
    , 0.999);
    FitOfProfile = fit(ArrayToFit(:,1),ArrayToFit(:,2),'pchip');

    % Determine resolution of provided profile.
    SamplingResolution = InputArray(2,1) - InputArray(1,1);

    % Find spatial coordinates across missing interval with identical
    % sampling resolution and coordinates of removed dead channels.
    IntervalX = [transpose(InputArray(128,1)+SamplingResolution :
    SamplingResolution : InputArray(129,1)-SamplingResolution) ;
    InputArray(I,1)];

    % Determine magnitude of profile from fit at the 'X' spatial
    coordinates.
    IntervalY = feval(FitOfProfile,IntervalX);

    % Concatenate vectors together.
    CatArray = [ArrayToFit ; [IntervalX IntervalY]];

    % Sort spatial vector into descending order,and then sort the
    response vector based
    % upon the corresponding swaps.
    [CompleteArray,I] = sort(CatArray(:,1),1);
    CompleteArray(:,2) = CatArray(I,2);

    CentreArray = CompleteArray;

    %% PLOT THE FIT, INPUT SDMG DATA AND INTERPOLATED DATA.
    if showPlots == true
        subplot(1,2,2);
        scatter(InputArray(:,1),...
            InputArray(:,2),...
            40,...
            'MarkerFaceColor',[0 0 .8]);
        hold on
        plot(FitOfProfile);
        scatter(IntervalX(:,1),...
            IntervalY(:,1),...
            40,...
            'MarkerFaceColor',[1 0 0]);
        hold off
        box on
        xlabel('Distance (cm)');
        ylabel('Response (counts)');
        legend('Original Data','Fit','Interpolated Data');
        axis([0 InputArray(end,1) 0 max(ArrayToFit(:,2))*1.2]);
    end

    elseif isSDMG == 2
        %% FILTER ANY INPUT ARRAY FOR OUTLIERS ('DEAD' CHANNELS).
        ArrayToFit = InputArray;
        n = 9;

```

```

sigma = 0.7;
[~,I] = hampel(ArrayToFit(:,2),n,sigma);
ArrayToFit(I,:) = [];

if showPlots == true
    figure;
    title('Determine Outliers in Data');
    scatter(InputArray(:,1),...
            InputArray(:,2),...
            40,...
            'MarkerFaceColor',[0 0 .8]);
    box on
    xlabel('Distance (cm)');
    ylabel('Response (counts)');
    hold on
    plot(InputArray(I,1),InputArray(I,2),'sk','MarkerSize',10);
    hold off
    legend('Input Data','Identified Outliers');
    axis([0 InputArray(end,1) 0 max(ArrayToFit(:,2))*1.2]);
end

%FitOfProfile =
fit(ArrayToFit(:,1),ArrayToFit(:,2),'smoothingspline','SmoothingParam'
, 0.999);
FitOfProfile = fit(ArrayToFit(:,1),ArrayToFit(:,2),'pchip');

IntervalX = InputArray(I,1);
IntervalY = feval(FitOfProfile,IntervalX);
CatArray = [ArrayToFit ; [IntervalX IntervalY]];
[CompleteArray,I] = sort(CatArray(:,1),1);
CompleteArray(:,2) = CatArray(I,2);
CentreArray = CompleteArray;
else
CentreArray = InputArray;
end

if useMaximumOfProfile == 0;
%% FINDING CENTRE OF ARRAY.
% Downsample data.
DownSampledInputArray = downsample(CentreArray,3);
% Filter out noise in downsampled data.
FilteredDSIA = medfilt1(DownSampledInputArray(:,2),5);
% Calculate the discrete forward derivative of the filtered data.
ForwardDerivative =
diff(FilteredDSIA)./diff(DownSampledInputArray(:,1));

% Determine the spatial coordinates of the max and min peaks.
LHS = DownSampledInputArray(ForwardDerivative ==
max(ForwardDerivative),1);
RHS = DownSampledInputArray(ForwardDerivative ==
min(ForwardDerivative),1);

% Calculate FWHM and estimate centre of profile.
FWHM = (RHS - LHS);
CentreEstimate = LHS + (FWHM/2);
% Find true centre of complete data from downsampled centre.
FindingCentre = (CentreArray(:,1) - CentreEstimate).^2;

% Determine Index of centre value and true centre value.
CentreIndex = find(FindingCentre == min(FindingCentre));
CentreValue = CentreArray(CentreIndex(1),1);

```

```

%% DETERMINE MAXIMUM.
% Empirically determined formula to determine size of ROI to
average over
% for normalisation of profile and accurate percentage
calculation.
AreaOfProfile = (-0.0037602032*(FWHM^3)) + (0.0768540576*(FWHM^2))
+ (0.1020720234*(FWHM)) + (0.0532649909);

% Determine resolution of profile.
SamplingResolution = InputArray(2,1) - InputArray(1,1);

% Calculate number of elements to determine the 'average of',
about the centre.
NumberOfElements = AreaOfProfile/SamplingResolution;

% Round to nearest even integer.
NumberOfElements = 2*round(NumberOfElements/2);

Maximum = mean(CentreArray((CentreIndex(1) - NumberOfElements/2) :
(CentreIndex(1) + NumberOfElements/2) , 2));

%% FIT AND INTERPOLATE LOCATIONS.
FitModelOfInput = fit(CentreArray(:,1),CentreArray(:,2),'pchip');

if showPlots == true
    figure;
    scatter(InputArray(:,1),...
            InputArray(:,2),...
            40,...
            'MarkerFaceColor',[0 0 .8]);
    box on
    axis tight;
    hold on
    plot(FitModelOfInput);
    hold off
    legend('Input Data','Fit');
    xlabel('Distance (cm)');
    ylabel('Response (counts)');
    axis([0 InputArray(end,1) 0 max(CentreArray(:,2))*1.2]);
end

objective = @(i) FitModelOfInput(i) - (Yvalue*Maximum);
X(1,1) = fzero(objective,[CentreArray(1,1) CentreValue]);
%LHS
X(1,2) = fzero(objective,[CentreValue CentreArray(end,1)]);
%RHS

clearvars pitch y profile_temporary distance_temporary profile_max
profile_fit

%% PLOTTING.
if showPlots == true
    figure;
    subplot(1,2,1);
    scatter(DownSampledInputArray(1:end-1,1),...
            ForwardDerivative(:,1),...
            40,...
            'MarkerFaceColor',[0 0 .8]);
    box on
    xlabel('Distance (cm)');

```

```

        ylabel('First Derivative');
        hold on
        plot(DownSampledInputArray(ForwardDerivative ==
max(ForwardDerivative),1),ForwardDerivative(ForwardDerivative ==
max(ForwardDerivative),1),'sk','MarkerSize',10);
        plot(DownSampledInputArray(ForwardDerivative ==
min(ForwardDerivative),1),ForwardDerivative(ForwardDerivative ==
min(ForwardDerivative),1),'sk','MarkerSize',10);
        hold off
        legend('Forward Derivative','Identified Max/Min');

        subplot(1,2,2);
        scatter(InputArray(:,1),...
            InputArray(:,2),...
            40,...
            'MarkerFaceColor',[0 0 .8]);
        box on
        axis tight;
        hold on
        plot(FitModelOfInput);

        line([InputArray(1,1),InputArray(end,1)], [Maximum,Maximum], 'Color','g'
, 'LineWidth',1, 'LineStyle','--'); % Maximum
        line([CentreArray((CentreIndex(1)-
NumberOfElements/2),1),CentreArray((CentreIndex(1)-
NumberOfElements/2),1)], [0,max(InputArray(:,2))*1.2], 'Color','m', 'Line
Width',1, 'LineStyle','--'); %LHS line of maximum area.

        line([CentreArray((CentreIndex(1)+NumberOfElements/2),1),CentreArray((
CentreIndex(1)+NumberOfElements/2),1)], [0,max(InputArray(:,2))*1.2], 'C
olor','m', 'LineWidth',1, 'LineStyle','--'); %RHS line of maximum area.

        line([X(1,1),X(1,1)], [0,max(InputArray(:,2))*1.2], 'Color','k', 'LineWid
th',1, 'LineStyle','--'); %LHS occurence of POI.

        line([X(1,2),X(1,2)], [0,max(InputArray(:,2))*1.2], 'Color','k', 'LineWid
th',1, 'LineStyle','--'); %RHS occurence of POI.
        hold off
        legend('Input Data','Fit');
        xlabel('Distance (cm)');
        ylabel('Response (counts)');
        axis([0 InputArray(end,1) 0 max(CentreArray(:,2))*1.2]);
    end
else
    %% USE THE MAXIMUM IN PROFILE.
    FitModelOfInput = fit(InputArray(:,1),InputArray(:,2),'pchip');

    MaximumOfInput = max(InputArray(:,2));
    CentreOfProfile = InputArray(InputArray(:,2) == MaximumOfInput,1);

    objective = @(i) FitModelOfInput(i) - (Yvalue*MaximumOfInput);
    X(1,1) = fzero(objective,[InputArray(1,1) CentreOfProfile]);
    %LHS
    X(1,2) = fzero(objective,[CentreOfProfile InputArray(end,1)]);
    %RHS

    clearvars MaximumOfInput CentreOfProfile FitModelOfInput objective
end
end
end

```

A.3.calculateEqualisation.m

```
function [ EqualisationFactors , EqualisationVector ] =  
calculateEqualisation( Path , ...  
    Map )  
%calculateEqualisation:  
%  
  
%% Select File:  
  
fprintf('DETECTOR RESPONSE - EQUALISATION:\n');  
fprintf('\tSelect the file/s to produce equalisation factors.\n');  
[FileNames, FilePath] = uigetfile('*.*', 'Select Decoded Files to  
produce Equalisation Array:', Path);  
  
if ischar(FilePath) == 0 && ischar(FileNames) == 0  
    % If cancel is pressed in pop-up window, function exits returning  
    0.  
    fprintf('\tCancel.\n');  
    EqualisationFactors = 0;  
    EqualisationVector = 0;  
    return  
else  
    File = fullfile(FilePath, FileNames);  
    fprintf('\t\tFile selected: %s.\n',FileNames);  
end  
  
%% 0. HIDDEN PARAMETERS.  
fprintf('\t2. Generating the equalisation factors...\n');  
  
plotProfile = true;  
  
plotTimeResponse = true;  
ChannelNumber = 200;  
  
baselineSubtractionOption = 0; % 0 = Manual, 1 = Automatic, 2 = off.  
useForLoop = false;  
  
LowerThreshold = 0.01;  
UpperThreshold = 3;  
  
LogicalStr = {'False', 'True'};  
fprintf('\t\tPlot Time Response of channel %d: %s\n',ChannelNumber,  
LogicalStr{plotTimeResponse + 1});  
  
if baselineSubtractionOption == 0  
    fprintf('\t\tBaseline Subtraction: Manual\n');  
elseif baselineSubtractionOption == 1  
    fprintf('\t\tBaseline Subtraction: Automatic\n');  
elseif baselineSubtractionOption == 2  
    fprintf('\t\tBaseline Subtraction: Off\n');  
end  
  
fprintf('\t\tPlot the result: %s\n', LogicalStr{plotProfile + 1});  
  
fprintf('\t\tRestrict Equalisation Factors below: %0.2f\n',  
LowerThreshold);  
fprintf('\t\tRestrict Equalisation Factors above: %0.2f\n',  
UpperThreshold);
```

```

%% 1. IMPORT DATA.

Data = importdata(File, '\t');

%% 2. SETUP TIME PARAMETERS.

samplingFrequency = 360; % Sampling
frequency % Sampling period
period = 1/samplingFrequency; % Length of signal
numberOfSamples = size(Data,1); % Time vector
time = (0:numberOfSamples-1)*period; % Swap to column
time = time';
vector

%% 3. PLOT DETECTOR RESPONSE AS FUNCTION OF TIME.

if plotTimeResponse == true
    figure;
    plot(time, (Data(:,ChannelNumber))./65535*100, 'LineWidth', 1);
    axis tight;
    box on;
    title('Channel Response');
    ylabel('Response (%)');
    xlabel('Time (s)');
end

%% 4. BASELINE SUBTRACTION OPTIONS.

baselineSubtractionTime = 1; % Time (in seconds) from end of file
to consider noise over i.e. determines noise ROI.

if baselineSubtractionOption == 0
    defaultAns = {num2str(period*(size(Data,1))-
baselineSubtractionTime), num2str(period*(size(Data,1)))};
    answer = inputdlg({'Enter time 1 (s):', 'Enter time 2
(s):'}, 'Input', 1, defaultAns);
    RegionOfInterestLeft =
floor((str2double(answer{1}))*samplingFrequency);
    RegionOfInterestRight =
floor((str2double(answer{2}))*samplingFrequency);
else
    RegionOfInterestLeft = floor((period*(size(Data,1))-
baselineSubtractionTime)*samplingFrequency);
    RegionOfInterestRight =
floor(period*(size(Data,1))*samplingFrequency);
end

% Calculate Noise.
MeanNoise = (mean(Data( RegionOfInterestLeft : RegionOfInterestRight ,
:))).*size(Data,1);

if baselineSubtractionOption == 2 % 2 - off.
    IntegralData = sum(Data);
else
    IntegralData = (sum(Data)) - MeanNoise;
end

%% 6. ZERO-OUT NEGATIVE VALUES.

if useForLoop == true
    for i = 1 : size(IntegralData,2)

```

```

        if(IntegralData(1,i)<0)
            IntegralData(1,i) = 0;
        end
    end
else
    [~, col] = find( IntegralData < 0);
    IntegralData(col) = 0;
    clearvars row col
end

%% 7.

IntegralMean = mean(IntegralData);

EqualisationVector = IntegralData./IntegralMean;

%% 8. THRESHOLD EQUALISATION FACTORS TO ELIMINATE HIGHS/LOWS.

if useForLoop == true
    for i = 1 : size(EqualisationVector,2)
        if(EqualisationVector(1,i)<LowerThreshold)
            EqualisationVector(1,i) = 1;
        end
        if(EqualisationVector(1,i)>UpperThreshold)
            EqualisationVector(1,i) = 1;
        end
    end
else
    [~, col] = find( EqualisationVector < LowerThreshold);
    EqualisationVector(col) = 1;
    clearvars row col

    [~, col] = find( EqualisationVector > UpperThreshold);
    EqualisationVector(col) = 1;
end

%% 9.

EqualisationFactors = rearrange(EqualisationVector,Map);

[row, col] = find(isnan(EqualisationFactors));
for i=1:size(row,1)
    EqualisationFactors(row(i),col(i)) = 0;
end

clearvars i
%% 10.

if plotProfile == true
    plotProfileFromDetector( EqualisationFactors );
end
fprintf('\t3. Complete!\n\n');
end

```

A.4. integrateFile.m

```

function [ Output ] = integrateFile( Path , ...
    Map , ...
    EqualisationFactors, ...
    Mask)

```

```

%FileIntegrate:
%

% Check if equalisation factors are supplied or not, if not supplied
% calculate un-equalised profile.
if nargin == 2
    EqualisationFactors = false;
    Mask = false;
elseif nargin == 3
    Mask = false;
end

%% Select File:

fprintf('\nDETECTOR RESPONSE - INTEGRATION:\n');
fprintf('\t1. Select the file/s to integrate.\n');
[FileNames, FilePath] = uigetfile('*.txt', 'Select Decoded Files for
Analysis:', Path);

if ischar(FilePath) == 0 && ischar(FileNames) == 0
    % If cancel is pressed in pop-up window, function exits returning
    0.
    fprintf('\tCancel.\n');
    Output = false;
    return
else
    File = fullfile(FilePath, FileNames);
    fprintf('\t\tFile selected: %s.\n',FileNames);
end

if EqualisationFactors == false
    fprintf('\t2. Generating the unequalised integral...\n');
else
    fprintf('\t2. Generating the equalised integral...\n');
end

%% 0. HIDDEN PARAMETERS.
plotProfile = true;
plotTimeResponse = true;
ChannelNumber = 200;
baselineSubtractionOption = 2; % 0 = Manual, 1 = Automatic, 2 = off.
useForLoop = false;

filterData = true;
k = 50; % Number of adjacent samples on either side samples in data
over which to compute Hampel Identifier.
nsigma = 0.5; % Number of estimated standard deviations above which
will be filtered.
plotFilteredComparison = false;

plotType = 'charge';
chargeQuanta = 4.8; % (pC) - range 5

if strcmp(plotType,'raw') == true
    modifier = 1;
    labelY = 'Raw Response (counts)';
elseif strcmp(plotType,'response') == true
    modifier = 65535/100;
    labelY = 'Normalised Response (%)';
elseif strcmp(plotType,'charge') == true
    modifier = 65535/chargeQuanta;

```



```

        labelY = 'Charge (pC)';
elseif strcmp(plotType,'dose') == true
    %     modifier = 65535/(chargeQuanta*doseConversion);
    %     labelY = 'Dose (cGy)';
end

%% DISPLAY OUTPUTS:
LogicalStr = {'False', 'True'};
fprintf('\t\tFilter data: %s\n', LogicalStr{filterData + 1});
if filterData == true
    fprintf('\t\tHampel Filter, k: %d\n', k);
    fprintf('\t\tHampel Filter, nsigma: %0.2f\n', nsigma);
end

fprintf('\t\tPlot Time Response of channel %d: %s\n',ChannelNumber,
LogicalStr{plotTimeResponse + 1});

if baselineSubtractionOption == 0
    fprintf('\t\tBaseline Subtraction: Manual\n');
elseif baselineSubtractionOption == 1
    fprintf('\t\tBaseline Subtraction: Automatic\n');
elseif baselineSubtractionOption == 2
    fprintf('\t\tBaseline Subtraction: Off\n');
end

fprintf('\t\tPlot the result: %s\n', LogicalStr{plotProfile + 1});

clearvars LogicalStr
%% NESTED FUNCTIONS.

function [CorrectedIntegral , Integral] = baselineSubtract(file,
data, option, frequency, period, isUnFilteredData)
    subtractionTime = 1;    % Time (in seconds) from end of file
to estimate average noise over.
    if option == 0
        defaultAns = {num2str(period*(size(data,1))-
subtractionTime),num2str(period*(size(data,1)))};
        answer = inputdlg({'Enter time 1 (s):','Enter time 2
(s):'},'Input',1,defaultAns);
        RegionOfInterestLeft =
floor((str2double(answer{1}))*frequency);
        RegionOfInterestRight =
floor((str2double(answer{2}))*frequency);
    else
        RegionOfInterestLeft = floor((period*(size(data,1))-
subtractionTime)*frequency);
        RegionOfInterestRight =
floor(period*(size(data,1))*frequency);
    end

    MeanNoise = (mean(data(RegionOfInterestLeft :
RegionOfInterestRight , :))).*size(data,1);

    if option == 2    % If baseline subtraction is selected off.
        [CorrectedIntegral , Integral] = sumData(file, data,
frequency, isUnFilteredData);
    else
        [CorrectedIntegral , Integral] = sumData(file, data,
frequency, isUnFilteredData);
        if islogical(CorrectedIntegral) == false
            CorrectedIntegral = CorrectedIntegral - MeanNoise;

```

```

        end
        Integral = Integral - MeanNoise;
    end
end

function [ CorrectedIntegral , Integral ] = sumData(file, data,
frequency, isUnFilteredData)
    AngleFile = strcat(file(1:end-11),'angles.aux');
    if exist(AngleFile,'file') == 2
        AngleImport = importdata(AngleFile, '\t');

        load('C:\Users\Matt\Google
Drive\MATLAB\Detector\DUO_angularCorrection');
        pp =
pchip(DUO_angularCorrection(:,1),DUO_angularCorrection(:,2));
        cf = zeros(size(AngleImport,1),1);
        for j = 1:size(AngleImport,1)
            cf(j,1) = ppval(pp,AngleImport(j,1));
        end

        correctedData = zeros(size(data,1),size(data,2));
        for row = 1:size(data,1)
            for col = 1:size(data,2)
                correctedData(row,col) = data(row,col)/cf(row,1);
            end
        end

        if isUnFilteredData == false
            fprintf('\t\tAngular Correction Applied.\n');
            figure;
            subplot(1,2,1);
            t =
linspace(1,size(AngleImport,1),size(AngleImport,1));
            t = t*1/frequency;
            scatter(t,AngleImport);
            axis square; box on;
            xlabel('Time (s)');ylabel('Angle (degrees)');
            axis([0 t(end,end) -270 270]);
            subplot(1,2,2);
            scatter(t,cf);
            axis square; box on;
            xlabel('Time (s)');ylabel('Correction Factor');
            axis([0 t(end,end) 0 2]);
        end

        CorrectedIntegral = (sum(correctedData));
        Integral = (sum(data));
    else
        if isUnFilteredData == false
            fprintf('\t\tNo Angular Correction.\n');
        end

        CorrectedIntegral = false;
        Integral = (sum(data));
    end
end

function [ I ] = zeroOut(inputIntegral, useLoop)
    if useLoop == true
        for j = 1 : size(inputIntegral,2)
            if(inputIntegral(1,j)<0)

```

```

        inputIntegral(1,j) = 0;
    end
end
else
    [~, c] = find( inputIntegral < 0);
    inputIntegral(c) = 0;
end
I = inputIntegral;
end

function [UnequalisedIntegral, EqualisedIntegral] =
adjustIntegral(inputVector, inputMap, inputEQFactors)
    Array = rearrange(inputVector, inputMap);
    if inputEQFactors == false
        UnequalisedIntegral = Array;
        EqualisedIntegral = false;
    else
        UnequalisedIntegral = Array;
        EqualisedIntegral = Array ./ inputEQFactors;
    end
    [r, c] = find(isnan(UnequalisedIntegral));
    UnequalisedIntegral(r,c) = 0;
    clearvars r c
    [r, c] = find(isnan(EqualisedIntegral));
    EqualisedIntegral(r,c) = 0;
end

%% 1. IMPORT DATA.

DataImport = importdata(File, '\t');

%% 2. SETUP TIME PARAMETERS.

samplingFrequency = 360; % Sampling
frequency % Sampling period
period = 1/samplingFrequency; % Length of signal
numberOfSamples = size(DataImport,1); % Time vector
time = (0:numberOfSamples-1)*period; % Swap to column
time = time';
vector

%% 2.b) Filter Data

if filterData == true
    Data = hampel(DataImport,k,nsigma);
else
    Data = DataImport;
end

%% 3. PLOT DETECTOR RESPONSE AS FUNCTION OF TIME.

function resize1(source,event)
    fig1Pos = fig1.Position;
    ax1.Position = [0.1*fig1Pos(3) 0.15*fig1Pos(4) 0.8*fig1Pos(3)
0.75*fig1Pos(4)];
end

if plotTimeResponse == true
    fig1 = figure;
    fig1.SizeChangedFcn = @resize1;

```

```

    ax1 = axes(fig1);
    ax1.Units = 'pixels';
    ax1.Position = [0.1*fig1.Position(3) 0.15*fig1.Position(4)
0.8*fig1.Position(3) 0.8*fig1.Position(4)];
    ax1.Box = 'on';
    if filterData == true

plot(ax1,time,(DataImport(:,ChannelNumber))./modifier,'LineWidth',1);
    hold(ax1,'on');

plot(ax1,time,(Data(:,ChannelNumber))./modifier,'LineWidth',1);
    legend('Unfiltered Data','Hampel Filtered Data');
    hold(ax1,'off');
    else

plot(ax1,time,(Data(:,ChannelNumber))./modifier,'LineWidth',1);
    end
    ax1.Title.String = 'Channel Response';
    ax1.XLabel.String = 'Distance (cm)';
    ax1.YLabel.String = labelY;
end

clearvars numberOfSamples
%% 4. BASELINE SUBTRACTION OPTIONS.

[AngCorIntegral, Integral] = baselineSubtract(File, Data,
baselineSubtractionOption, samplingFrequency, period, false);

if filterData == true
    [UnfiltAngCorIntegral, UnfiltIntegral] = baselineSubtract(File,
DataImport, baselineSubtractionOption, samplingFrequency, period,
true);
else
    UnfiltAngCorIntegral = false;
    UnfiltIntegral = false;
end
%% 5. ZERO-OUT NEGATIVE INTEGRAL VALUES.

Integral = zeroOut(Integral, useForLoop);

if islogical(AngCorIntegral) == false
    AngCorIntegral = zeroOut(AngCorIntegral, useForLoop);
end

if filterData == true
    UnfiltIntegral = zeroOut(UnfiltIntegral, useForLoop);
    if islogical(UnfiltAngCorIntegral) == false
        UnfiltAngCorIntegral = zeroOut(UnfiltAngCorIntegral,
useForLoop);
    end
end
%% 6. MAP THE VECTOR INTO THE OUTPUT ARRAY.

[UnEqIntegral, EqIntegral] = adjustIntegral(Integral, Map,
EqualisationFactors);

if islogical(AngCorIntegral) == false
    [UnEqAngCorIntegral, EqAngCorIntegral] =
adjustIntegral(AngCorIntegral, Map, EqualisationFactors);
else
    UnEqAngCorIntegral = false;

```

```

    EqAngCorIntegral = false;
end

if filterData == true
    [UnEqUnfiltIntegral, EqUnfiltIntegral] =
adjustIntegral(UnfiltIntegral, Map, EqualisationFactors);
    if islogical(UnfiltAngCorIntegral) == false
        [UnEqUnfiltAngCorIntegral, EqUnfiltAngCorIntegral] =
adjustIntegral(UnfiltAngCorIntegral, Map, EqualisationFactors);
    else
        UnEqUnfiltAngCorIntegral = false;
        EqUnfiltAngCorIntegral = false;
    end
end

%% 7. SELECT CORRECT INTEGRAL.

if islogical(EqualisationFactors) == false
    if islogical(EqAngCorIntegral) == false
        integral = EqAngCorIntegral;
    else
        integral = EqIntegral;
    end
else
    if islogical(UnEqAngCorIntegral) == false
        integral = UnEqAngCorIntegral;
    else
        integral = UnEqIntegral;
    end
end

if plotFilteredComparison == true
    if islogical(EqualisationFactors) == false
        if islogical(EqUnfiltAngCorIntegral) == false
            unfiltintegral = EqUnfiltAngCorIntegral;
        else
            unfiltintegral = EqUnfiltIntegral;
        end
    else
        if islogical(UnEqUnfiltAngCorIntegral) == false
            unfiltintegral = UnEqUnfiltAngCorIntegral;
        else
            unfiltintegral = UnEqUnfiltIntegral;
        end
    end
end

%%
if size(Mask) > 1
    channels = transpose(1:(size(integral,1)-1));

    Horiz(:,1) = channels;
    Vert(:,1) = channels;
    Horiz(:,2) = integral(1:end-1,1);
    Vert(:,2) = integral(1:end-1,2);

    MaskH = Mask(:,1);
    MaskV = Mask(:,2);
    Horiz(MaskH,:) = [];
    Vert(MaskV,:) = [];

    FinalIntegral(:,1) =
interpl(Horiz(:,1),Horiz(:,2),channels,'pchip');

```

```

    FinalIntegral(:,2) =
interp1 (Vert(:,1),Vert(:,2),channels,'pchip');
    FinalIntegral(end+1,:) = 0;

    integral = FinalIntegral;
    EqIntegral = FinalIntegral;
end
%% 8. PLOT.
pitch = 0.02;

function resize2(source,event)
    ax2.Position = [0.1*fig2.Position(3) 0.15*fig2.Position(4)
0.8*fig2.Position(3)/2 0.8*fig2.Position(4)];
    ax3.Position = [0.55*fig2.Position(3) 0.15*fig2.Position(4)
0.8*fig2.Position(3)/2 0.8*fig2.Position(4)];
end

fig2 = figure;
orig2Position = fig2.Position;
fig2.Position = [orig2Position(1) orig2Position(2) 2*orig2Position(3)
orig2Position(4)];
fig2.SizeChangedFcn = @resize2;

ax2 = axes(fig2);
ax2.Units = 'pixels';
ax2.Position = [0.1*fig2.Position(3) 0.15*fig2.Position(4)
0.75*fig2.Position(3)/2 0.8*fig2.Position(4)];

ax3 = axes(fig2);
ax3.Units = 'pixels';
ax3.Position = [0.55*fig2.Position(3) 0.15*fig2.Position(4)
0.75*fig2.Position(3)/2 0.8*fig2.Position(4)];

% distance = transpose(((0:(size(Map,1)-1))*pitch));
distance = transpose(1:(size(Map,1)));

if plotProfile == true
    if plotFilteredComparison == true
        scatter(ax2,distance,integral(:,1),'filled');
        hold(ax2,'on');
        scatter(ax2,distance,unfiltintegral(:,1),'filled');
        hold(ax2,'off');

        scatter(ax3,distance,integral(:,2),'filled');
        hold(ax3,'on');
        scatter(ax3,distance,unfiltintegral(:,2),'filled');
        hold(ax3,'off');
    else
        scatter(ax2,distance,integral(:,1),'filled');
        scatter(ax3,distance,integral(:,2),'filled');
    end
end

ax2.Box = 'on';
ax2.Title.String = 'Horizontal';
ax2.XLabel.String = 'Distance (cm)';
ax2.YLabel.String = labelY;
ax2.XLim = [0 max(distance)];

ax3.Box = 'on';
ax3.Title.String = 'Vertical';

```

```

ax3.XLabel.String = 'Distance (cm)';
ax3.YLabel.String = labelY;
ax3.XLim = [0 max(distance)];

%% 9. ASSEMBLE OUTPUT.

Output.Equalised.Integral = EqIntegral;
Output.Equalised.AngularCorrectedIntegral = EqAngCorIntegral;
Output.Equalised.UnfilteredIntegral = EqUnfiltIntegral;
Output.Equalised.UnfilteredAngularCorrectedIntegral =
EqUnfiltAngCorIntegral;

Output.Unequalised.Integral = UnEqIntegral;
Output.Unequalised.AngularCorrectedIntegral = UnEqAngCorIntegral;
Output.Unequalised.UnfilteredIntegral = UnEqUnfiltIntegral;
Output.Unequalised.UnfilteredAngularCorrectedIntegral =
UnEqUnfiltAngCorIntegral;

Output.EqualisationFactors = EqualisationFactors;
Output.Map = Map;

Output.File = File;
%% Find Channels responsible for penumbra: 20, 50 & 80%

HorizontalOrVertical = 2; % 1 - Horizontal or 2 - Vertical.

function [out] = findChannels(inputdata, R, inputIntegral,
inputMap, HorV)
    % Y
    in(:,2) = inputIntegral(:,HorV);
    % X
    pitch = 0.02;
    profileSize = size(in,1)-1;
    distance = transpose((0:profileSize)*pitch);
    in(:,1) = distance;

    channel = findX(in,R,2,false);
    channel = round(channel./pitch);

    if size(Mask) > 1
        while Mask(channel(1),HorV) == 1
            channel(1) = channel(1)+1;
        end
        while Mask(channel(2),HorV) == 1
            channel(2) = channel(2)+1;
        end
    end

    channel = inputMap(channel,HorV);

    out(:,1) = inputdata(:,channel(1));
    out(:,2) = inputdata(:,channel(2));
end

Output.TimeResponse = findChannels(Data, 0.5, integral, Map,
HorizontalOrVertical);

figure;
subplot(1,2,1);
plot(time, (Output.TimeResponse(:,1))./modifier, 'LineWidth', 1);
axis tight;

```

```
box on;
title('LHS Penumbra Channel');
ylabel(labelY);
xlabel('Time (s)');
subplot(1,2,2);
plot(time,(Output.TimeResponse(:,2))./modifier,'LineWidth',1);
axis tight;
box on;
title('RHS Penumbra Channel');
ylabel(labelY);
xlabel('Time (s)');

%%

fprintf('\t3. Complete!\n\n');
end
```


Appendix B

B. Co-author works

The following pages detail the first page of manuscripts where I am co-author with a significant contribution to the study, the experimental data of which relates directly to:

- Chapter 6 – “Feasibility study of a novel multi-strip silicon detector for use in proton therapy range verification quality assurance”, published in *Radiation Measurements*
- Chapter 7 – “A silicon strip detector array for energy verification and quality assurance in heavy ion therapy” (Debrot, 2018), published in *Medical Physics*



Contents list available at ScienceDirect

Radiation Measurements

journal homepage: www.elsevier.com/locate/radmeas

Feasibility study of a novel multi-strip silicon detector for use in proton therapy range verification quality assurance

A.H. Merchant^a, M. Newall^b, S. Guatelli^{a,b}, M. Petasecca^{a,b}, M. Lerch^{a,b}, V. Perevertaylo^c, G. Milluzzo^d, G. Petringa^d, F. Romano^d, G.A.P. Cirrone^d, G. Cuttone^d, M. Jackson^{a,c} and A. B. Rosenfeld^{a,b,*}

^aCenter for Medical Radiation Physics, University of Wollongong, Wollongong, 2522, Australia

^bIllawarra Health Medical Research Institute, University of Wollongong, Wollongong, 2522, Australia

^cSPA BIT, Kiev, Ukraine

^dINFN, Catania, Italy

^eDepartment of Radiation Oncology, Prince of Wales Hospital, Sydney, 2031, Australia

HIGHLIGHTS

- ▶ A multi-strip silicon detector has been designed for proton range verification.
- ▶ Detector response has been experimentally characterised at the INFN CATANA facility.
- ▶ Geant4 studies have been performed to theoretically characterise the detector response.

ARTICLE INFO

Article history:

Received Click here to enter the received date

Received in revised form Revised date

Accepted Accepted date

Available on line On-line date

Keywords:

Particle therapy
Proton range verification
Multi-strip silicon detector
Geant4 Monte Carlo

ABSTRACT

The characterisation of a novel multi-strip silicon detector, the serial Dose Magnifying Glass, to incident 60MeV mono-energetic proton beams, typical for ocular melanoma treatment, was performed by means of Geant4 simulations and experimental methods. Geant4 simulations were performed to determine the applicability and potential of the detector for proton beam range verification with high spatial resolution. Experimental characterisation was performed using the CATANA beam line to confirm the Monte Carlo feasibility study and determine the detector response to incident proton beams of 5 mm, 13 mm, 25 mm and 36 mm diameter, in addition to the detector response when PMMA slabs are positioned between the detector and the beam nozzle. Results indicate the suitability of the detector for proton beam range verification in proton therapy Quality Assurance.

© 2016 Elsevier Ltd. All rights reserved

1. Introduction

* Corresponding author.

E-mail address: anatomy@uow.edu.au.

Since the publication of R. Wilson's seminal paper (Wilson, 1946) discussing the potential use of protons as a therapeutic alternative to conventional X-ray radiotherapy to today, research into the benefits of this treatment has progressed at a significant rate. Reflecting this, the number of facilities providing proton therapy, and the number of patients treated, has grown at an increasing rate (Jermann, 2015). The benefit of using protons for cancer treatment is the reduction of the total integral dose delivered to normal tissue while achieving a very conformal dose in the tumor target. This is due to the finite range of

A silicon strip detector array for energy verification and quality assurance in heavy ion therapy

Emily Debrot, Matthew Newall, Susanna Guatelli, and Marco Petasecca
Centre for Medical Radiation Physics, University of Wollongong, Wollongong, NSW 2500, Australia

Naruhiko Matsufuji
Research Centre for Charge Particle Therapy National Institute of Radiological Science, Chiba, Japan

Anatoly B. Rosenfeld^{a)}
Centre for Medical Radiation Physics, University of Wollongong, Wollongong, NSW 2500, Australia

Purpose: The measurement of depth dose profiles for range and energy verification of heavy ion beams is an important aspect of quality assurance procedures for heavy ion therapy facilities. The steep dose gradients in the Bragg peak region of these profiles require the use of detectors with high spatial resolution. The aim of this work is to characterize a one dimensional monolithic silicon detector array called the “serial Dose Magnifying Glass” (sDMG) as an independent ion beam energy and range verification system used for quality assurance conducted for ion beams used in heavy ion therapy.

Methods: The sDMG detector consists of two linear arrays of 128 silicon sensitive volumes each with an effective size of $2\text{ mm} \times 50\text{ }\mu\text{m} \times 100\text{ }\mu\text{m}$ fabricated on a p-type substrate at a pitch of 200 μm along a single axis of detection. The detector was characterized for beam energy and range verification by measuring the response of the detector when irradiated with a 290 MeV/u ^{12}C ion broad beam incident along the single axis of the detector embedded in a PMMA phantom. The energy of the ^{12}C ion beam incident on the detector and the residual energy of an ion beam incident on the phantom was determined from the measured Bragg peak position in the sDMG. Ad hoc Monte Carlo simulations of the experimental setup were also performed to give further insight into the detector response.

Results: The relative response profiles along the single axis measured with the sDMG detector were found to have good agreement between experiment and simulation with the position of the Bragg peak determined to fall within 0.2 mm or 1.1% of the range in the detector for the two cases. The energy of the beam incident on the detector was found to vary less than 1% between experiment and simulation. The beam energy incident on the phantom was determined to be (280.9 ± 0.8) MeV/u from the experimental and (280.9 ± 0.2) MeV/u from the simulated profiles. These values coincide with the expected energy of 281 MeV/u.

Conclusions: The sDMG detector response was studied experimentally and characterized using a Monte Carlo simulation. The sDMG detector was found to accurately determine the ^{12}C beam energy and is suited for fast energy and range verification quality assurance. It is proposed that the sDMG is also applicable for verification of treatment planning systems that rely on particle range.

Key words: energy verification, heavy ion therapy, Monte Carlo, QA, silicon strip detector